Agent-Based Modelling of Radiation-Induced Lung Injuries

Agentenbasierte Modellierung strahleninduzierter Lungenverletzungen
Zur Erlangung des Grades eines Doktors der Naturwissenschaften (Dr. rer. nat.)
Genehmigte Dissertation von Nicolò Cogno aus Savigliano
Tag der Einreichung: 17. Oktober 2023, Tag der Prüfung: 15. November 2023

1. Gutachten: Prof. Dr. Marco Durante
2. Gutachten: Prof. Dr. Kay Hamacher
Darmstadt, Technische Universität Darmstadt

TECHNISCHE
UNIVERSITÄT
DARMSTADT

Physics Department
IPKM
Strahlenbiophysik

Agent-Based Modelling of Radiation-Induced Lung Injuries
Agentenbasierte Modellierung strahleninduzierter Lungenverletzungen

Accepted doctoral thesis by Nicolò Cogno

Date of submission: 17th October 2023
Date of thesis defense: 15th November 2023

Darmstadt, Technische Universität Darmstadt

Bitte zitieren Sie dieses Dokument als:
URN: urn:nbn:de:tuda-tuprints-263354
URL: http://tuprints.ulb.tu-darmstadt.de/26335
Jahr der Veröffentlichung auf TUprints: 2023

Dieses Dokument wird bereitgestellt von tuprints,
E-Publishing-Service der TU Darmstadt
http://tuprints.ulb.tu-darmstadt.de
tuprints@ulb.tu-darmstadt.de

To those who have never ceased to support me.

Abstract

Radiotherapy (RT), which nowadays is integrated in more than 50% of the therapies of new cancer patients, involves the use of ionizing radiation (such as photon beams and ions) as a tool to sterilize cancers. However, the lethal doses to be delivered to the tumours are limited by normal tissue complications. Consequently, constraints must be set on the radiation dose and irradiated volume in order to maintain acceptable toxicity levels.

An important role in this context is played by computational models that ultimately provide valuable insights useful for tuning the RT parameters. Their use in the biomedical framework has a well-defined pattern: a theoretical model is initially built on the basis of the available *in-vitro* and/or *in-vivo* data and implemented *in-silico*; the model is then altered until a good match between its output and laboratory data is observed and finally used for predictions in the clinical setting. As yet, however, the tolerance doses for the organs at risk are derived from clinical experience and used as inputs for phenomenological Normal-Tissue Complication Probability (NTCP) models that lack a mechanistic description of the underlying phenomena.

This thesis describes the implementation of an Agent-Based Model (ABM) that simulates the onset of Radiation-Induced Lung Injuries (RILI) (namely pneumonitis and fibrosis), complications that can occur in the lungs of patients irradiated in the thoracic region. Although relatively common, the risk factors and progression of the RILI, which eventually lead to respiratory failure and death, haven't been fully elucidated. Here, the capability of the innovative AB modelling approach to improve patient-specific NTCP estimates while attempting to provide insights on the development of RILI is investigated. With respect to the existing dose-volume histogram-based and tissue-architecture approaches, ABMs can take into account not only the patient-specific geometry and tissue-level parameters, but also spatial information on the dose distribution.

As a first step, a 3D model of idiopathic pulmonary fibrosis, which resembles the Radiation-Induced Lung Fibrosis (RILF), was implemented using BioDynaMo, an AB simulation framework. The model, whose agents simulate a partial pulmonary acinus, can replicate previous experimental results and assess the appropriateness of the approach for the purpose. The model was subsequently rescaled to represent an alveolar segment at the cell scale that can be damaged locally by external sources. As a surrogate measure of the RILF severity, the RILF Severity Index (RSI) was introduced, derived by combining the loss in the alveolar volume with the increase in the average concentration of the ExtraCellular Matrix (ECM). The RSI showed qualitative agreement with a similar index obtained using data from computational tomographies and the ECM patterns matched clinical findings. Finally, a pipeline was established that links TOPAS-nBio, a particle transport simulator for biological applications, with BioDynaMo. The alveolar segment structure was rebuilt using TOPAS-nBio and the delivery of realistic dose distributions at the cell scale was simulated. The output was then used as an input for the AB model and the effect of different fractionation schemes and radiation qualities on the outcome explored. In accordance with previous studies, a 5-fractions treatment resulted in a lower RSI with respect to the delivery of the same dose in a single fraction and an increased sensitivity to peaked protons dose distributions with respect to flatter ones from photons irradiation was observed.

Overall, the results presented in this thesis prove the capability of the AB models to recapitulate some main radiobiological processes and advise for their potential complementary role in NTCP estimates.

Zusammenfassung

Strahlentherapie (RT), die heutzutage in mehr als 50% der Therapien für neue Krebspatienten integriert ist, umfasst die Verwendung von ionisierender Strahlung (wie Photonstrahlen und Ionen) als Werkzeug zur Abtötung von Krebszellen. Die letalen Dosen, die den Tumoren verabreicht werden müssen, sind jedoch durch Komplikationen im normalen Gewebe begrenzt. Folglich müssen Einschränkungen für die Strahlendosis und das bestrahlte Volumen festgelegt werden, um akzeptable Toxizitätsniveaus aufrechtzuerhalten.

In diesem Zusammenhang spielen computerbasierte Modelle eine wichtige Rolle, da sie letztendlich wertvolle Einblicke liefern, die zur Feinabstimmung der RT-Parameter nützlich sind. Ihre Verwendung im biomedizinischen Rahmen folgt einem gut definierten Muster: Ein theoretisches Modell wird zunächst auf der Grundlage der verfügbaren In-vitro- und/oder In-vivo-Daten entwickelt und in-silico umgesetzt; das Modell wird dann angepasst, bis eine gute Übereinstimmung zwischen den Ausgaben und Laborergebnissen festgestellt wird, und schließlich für Vorhersagen im klinischen Umfeld verwendet. Bisher stammen die Toleranzdosen für die Risikoorgane jedoch aus klinischer Erfahrung und werden als Eingabe für phänomenologische Modelle zur Normalgewebekomplikationswahrscheinlichkeit (NTCP) verwendet, die keine mechanistische Beschreibung der zugrunde liegenden Phänomene aufweisen.

Diese Dissertation beschreibt die Implementierung eines agentenbasierten Modells (ABM), das den Beginn von strahleninduzierten Lungenschäden (RILI) (insbesondere Pneumonitis und Fibrose) simuliert, Komplikationen, die in den Lungen von Patienten auftreten können, die im Brustbereich bestrahlt werden. Obwohl relativ häufig, sind die Risikofaktoren und der Verlauf von RILI, die letztendlich zu Atemversagen und Tod führen können, noch nicht vollständig aufgeklärt. Hier wird die Fähigkeit des innovativen AB-Modellierungsansatzes untersucht, patientenspezifische NTCP-Schätzungen zu verbessern und gleichzeitig Einblicke in die Entwicklung von RILI zu geben. Im Vergleich zu den bestehenden Dosis-Volumen-Histogramm-basierten und Gewebsarchitektur-Ansätzen können ABMs nicht nur die patientenspezifische Geometrie und gewebespezifische Parameter berücksichtigen, sondern auch räumliche Informationen zur Dosisverteilung.

Als ersten Schritt wurde ein 3D-Modell der idiopathischen Lungenfibrose implementiert, das der strahleninduzierten Lungenfibrose (RILF) ähnelt, und zwar unter Verwendung von BioDynaMo, einem AB-Simulationsframework. Das Modell, dessen Agenten einen Teil des Lungenazinus simulieren, kann frühere experimentelle Ergebnisse replizieren und die Angemessenheit des Ansatzes für den Zweck bewerten. Das Modell wurde anschließend in einen alveolären Segmentmaßstab umgesetzt, der auf Zellebene lokal durch externe Quellen geschädigt werden kann. Als Ersatzmaß für die Schwere der RILF wurde der RILF-Schweregrad-Index (RSI) eingeführt, abgeleitet aus der Kombination des Verlusts im alveolären Volumen mit der Zunahme der durchschnittlichen Konzentration der extrazellulären Matrix (ECM). Der RSI zeigte qualitative Übereinstimmung mit einem ähnlichen Index, der aus Daten von Computertomographien gewonnen wurde, und die ECM-Muster stimmten mit klinischen Befunden überein. Schließlich wurde eine Pipeline erstellt, die TOPAS-nBio, einen Teilchentransport-Simulator für biologische Anwendungen, mit BioDynaMo verknüpft. Die alveoläre Segmentstruktur wurde unter Verwendung von TOPAS-nBio neu erstellt, und die Lieferung realistischer Dosisverteilungen auf Zellebene wurde simuliert. Die Ausgabe wurde dann als Eingabe für das AB-Modell verwendet, und der Effekt unterschiedlicher Fraktionierungsschemata und Strahlenqualitäten auf das Ergebnis wurde erforscht. In Übereinstimmung mit früheren Studien führte

eine 5-Fraktionen-Behandlung zu einem geringeren RSI im Vergleich zur Verabreichung derselben Dosis in einer einzigen Fraktion, und eine erhöhte Empfindlichkeit gegenüber Spitzenprotonendosisverteilungen im Vergleich zu flacheren von Photonenstrahlung wurde beobachtet.

Insgesamt belegen die in dieser Dissertation präsentierten Ergebnisse die Fähigkeit der AB-Modelle, einige der wichtigsten radiobiologischen Prozesse zu rekapitulieren, und raten zu ihrer potenziellen ergänzenden Rolle bei NTCP-Schätzungen.

Contents

Acronyms

3DCRT 3D Conformal Radiation Therapy. 9, 10

AB Agent-Based. v, 1, 21, 25, 38, 47, 72, 75–77, 79, 81, 85, 86, 91–95

ABM Agent-Based Model. v, 1, 21–23, 26, 39, 41, 44, 53–55, 58, 65, 66, 72, 75–82, 84–87, 89, 91–94, 111, 112

AEC1 Alveolar Epithelial Cells of type 1. 11, 13, 34, 35, 37, 38, 44, 46, 50, 57–59, 61, 65–67, 69–71, 87, 88

AEC2 Alveolar Epithelial Cells of type 2. 11, 13, 34, 35, 37, 38, 44–49, 51, 52, 54, 57–61, 63–73, 79, 80, 82, 86–89, 91, 93, 94, 111

BC Boundary Condition. 29–31, 67, 88, 93, 111

BDM BioDynaMo. 1, 21, 25, 26, 28, 29, 32–34, 39, 40, 42, 44, 47, 48, 66–68, 70, 87, 91, 92

CFL Courant-Friedrichs-Lewy. 28, 32, 42, 43, 67, 89

CT Computed Tomography. 9, 14, 15, 52, 58, 67, 94

DNA DeoxyriboNucleic Acid. 2–8, 12, 18, 21, 22, 82, 86, 87, 95, 111

DSB Double Strand Break. 5, 6, 8, 86

DVH Dose-Volume Histogram. 9, 10, 12, 18, 21, 75, 84, 94

EBM Equation-Based Model. 38, 39, 54, 55, 58

ECM ExtraCellular Matrix. v, 11–13, 28, 36–38, 42, 45, 49, 51–54, 57–60, 62, 63, 65–73, 75, 77–81, 83–89, 93–95, 111

EMT Epithelial to Mesenchymal Transition. 12, 13, 37

EndMT Endothelial to Mesenchymal Transition. 12, 13

EUD Equivalent Uniform Dose. 18

FD Finite Difference. 29, 30

FGF2 Fibroblasts Growth Factor 2. 37, 38, 45, 46, 48, 54, 60, 69, 71

FI Fibrosis Index. 15, 62, 63, 66, 79, 85, 87, 94

FSU Functional Subunit. 19–21, 57–59, 61, 63, 65, 66, 73, 75, 77–81, 83–89, 94, 95

FTCS Forward Euler in Time and Central in Space method. 28, 29, 67, 88, 93

HPC High-Performance Computer. 25, 33, 92, 93, 111

HU Hounsfield Units. 15, 59, 94

IL13 Interleukin 13. 12, 37, 38, 45, 46, 57, 68, 71

IMRT Intensity Modulated Radiation Therapy. 9, 10, 12, 15

IPF Idiopathic Pulmonary Fibrosis. 1, 12, 36, 37, 44, 48, 57, 63, 65, 66, 69, 71, 93

LET Linear Energy Transfer. 4–6, 8, 9, 82, 86, 95

LQ Linear Quadratic. 6, 7, 20, 59, 61, 62, 65, 66, 72, 79, 82, 83, 85, 86, 88, 91, 94, 95

M0 Monocyte-derived Macrophages. 12, 37, 38, 44, 46, 57, 93

M1 Alveolar Macrophages of type 1. 12, 34, 35, 37, 38, 44–46, 54, 57–59, 61, 67–71, 79, 87, 88, 93

M2 Alveolar Macrophages of type 2. 12, 34, 35, 37, 38, 44–46, 54, 57–59, 61, 67–71, 79, 87–89

MC Monte Carlo. 1, 21, 23, 75–81, 84–86, 89, 91, 92, 94, 95, 112

MCP1 Monocyte chemoattractant protein 1. 12, 37, 38, 45, 46, 54, 57, 60, 68, 69, 79

MLD Mean Lung Dose. 12

MMP Matrix MetalloProteinases. 28, 37, 38, 42, 43, 45, 67, 68, 88, 93, 111

NSCLC Non-Small Cell Lung Cancer. 10

NTCP Normal-Tissue Complication Probability. v, 15–21, 23, 55, 57–59, 61, 65, 66, 75, 84–88, 93–95

OAR Organ At Risk. 9, 10

PDE Partial Differential Equation. 28, 29, 38, 42, 43, 47, 66, 88, 93

PDGF Platelet-Derived Growth Factor. 12, 37, 38, 45, 57, 68, 71

RBE Relative Biological Effectiveness. 8, 9, 83, 84, 86

RILF Radiation-Induced Lung Fibrosis. v, 1, 10, 12–16, 19, 21, 36, 37, 57–60, 62–66, 72, 73, 75, 76, 79, 85–87, 89, 93, 94

RILI Radiation-Induced Lung Injuries. v, 1, 8, 10, 12–15, 22, 23, 26, 28, 34, 36, 57, 59, 64, 66, 69, 75, 93, 94, 111

RIP Radiation-Induced Pneumonitis. 10, 12–14, 16, 21

ROS Reactive Oxygen Species. 12, 22

RSI RILF Severity Index. v, 20, 62, 63, 66, 75, 77–81, 83–88, 94, 95

RT Radiotherapy. v, 1, 2, 5, 6, 8–10, 13, 15, 52, 55, 57, 58, 64, 66, 73, 75, 84, 87, 93

SASP Senescence-Associated Secretory Phenotype. 37, 69

SBPT Stereotactic Body Proton Therapy. 10, 15

SBRT Stereotactic Body Radiation Therapy. 10, 12, 15

SEM Standard Error of the Mean. 78, 80, 81, 84

SSB Single Strand Break. 5, 6

TCP Tumour Control Probability. 15, 18, 20, 21

TGFβ Transforming Growth Factor Beta. 12, 37, 45–47, 57, 60

TIMP Tissue Inhibitors of MetalloProteinases. 37, 38, 42, 43, 45, 67, 68, 88, 111

TNFα Tumour necrosis factor alpha. 12, 37, 38, 45, 60, 68, 69, 71

VMAT Volumetric Modulated Arc Therapy. 10, 12, 15

1 Introduction

1.1 Thesis overview

Cancer is a pathological condition that affects millions of individuals and ranks second among the most lethal diseases in Europe [1], with the lung cancer being the deadliest type [2] (see Figure 1.1). This not withstanding, over the course of the last and the current century the field of cancer care has witnessed massive improvements in terms of outcomes and invasiveness reduction, with the implementation of both new treatment techniques and modalities. The increase in the oncolytic potential of these therapies, however, was not matched by an eradication of the risk of normal-tissue damage, hence the necessity of more research in the field. In these regards, mathematical and computational models can provide invaluable features, allowing researchers to perform fast hypothesis-testing on both spatial and temporal multi-scales.

Contextually, this thesis deals with the implementation and characterization of mechanistic models of Radiation-Induced Lung Injuries (RILI), using the relatively novel Agent-Based (AB) approach [3].

In this first chapter, an overview of the fundamental Radiotherapy (RT) concepts is provided, followed by a description of the pathogenesis of the RILI and the role of computational and mathematical modelling as predictive tools for estimating complication probabilities. Chapter 2 explores the main concepts of AB modelling, providing examples from the open-source platform BioDynaMo (BDM) [4, 5], which implements them. Furthermore, personal contributions to the framework, which was employed to develop the models outlined later in the thesis, are documented. The implementation of a 3D Agent-Based Model (ABM) of Idiopathic Pulmonary Fibrosis (IPF) (a disease whose pathogenesis resembles that of the radiation-induced lung pneumonitis and fibrosis) together with results that match previously published experimental studies is then detailed in Chapter 3. The following chapter (see Chapter 4) documents the implementation of a 3D ABM of Radiation-Induced Lung Fibrosis (RILF) in an alveolar segment irradiated with photons. The model shows the temporal evolution of both the cellular and the chemical dynamics in a time frame that spans 3 years and the results, concerning patterns of onset of the disease and its degree of severity, match qualitatively experimental studies. Finally, Chapter 5 outlines the implementation of the aforementioned alveolar duct model in a Monte Carlo (MC) simulator of radiation transport, namely Topas-nBio [6], and a corresponding input/output interface to BDM. The two software are employed to simulate realistic photon distributions and compare the effect of a temporal fractionation scheme on the model outcomes as well as that of protons.

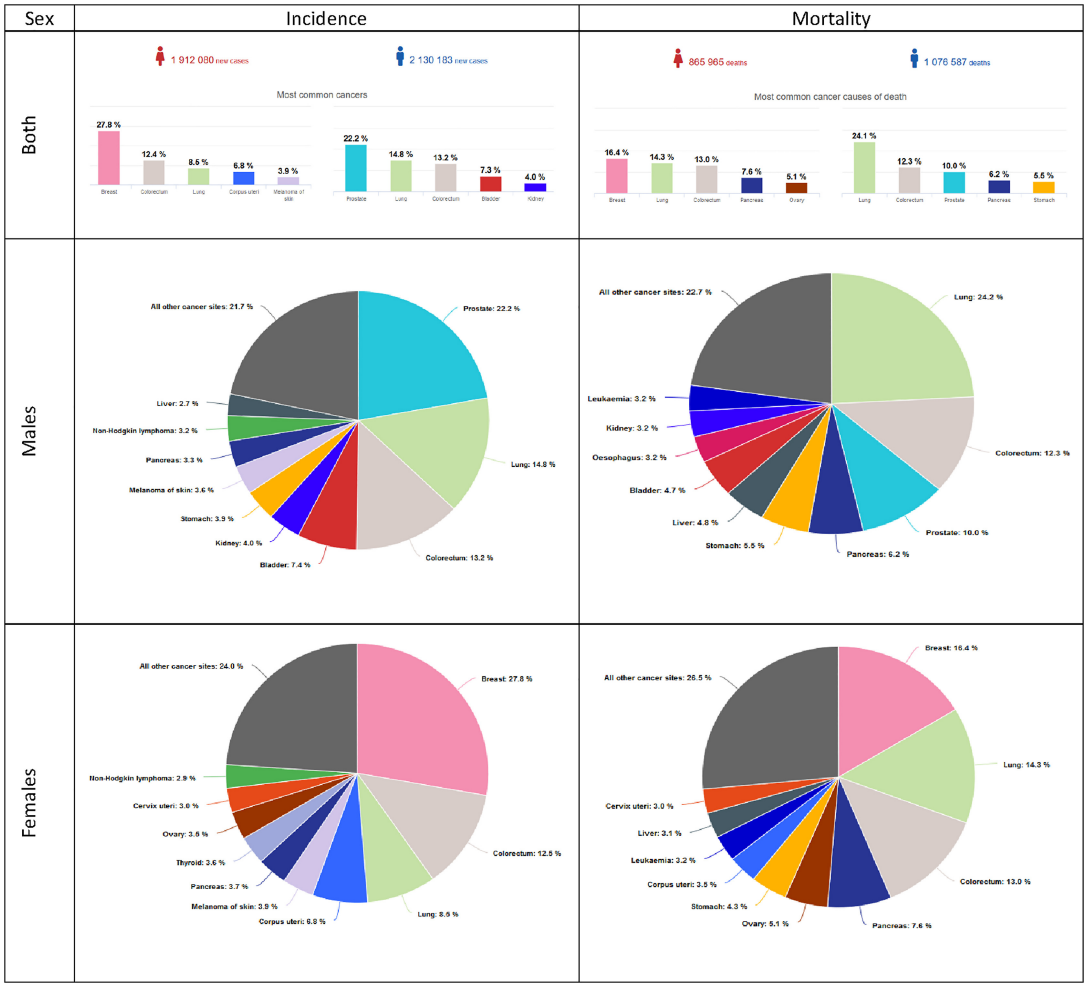

Figure 1.1: Incidence and mortality rate of cancer by sex in Europe. Figure from [2].

1.2 Radiation therapy

Unlike pharmaceutical treatments, RT for cancer care exploits external beams to deliver energy to the target regions. The aim of the energy deposition, in turn, is the ionisation and subsequent damage of the tumour cells' DeoxyriboNucleic Acid (DNA) molecules which, if unresolved, can trigger cell-killing mechanisms. The aforementioned energy can be delivered both by photons, charged and uncharged particles and although the radiation-matter interaction mechanisms of the listed carriers differ substantially, the dose D, with SI-unit Gray [Gy] and defined by the absorbed energy E to a volume element of mass m, divided by the mass of the volume itself, as follows

$$D = \frac{E}{m} \quad [1Gy = 1J/kg] \tag{1.1}$$

can be used to characterise in a first approximation the extent of the damage.

Since Chapter 4 and Chapter 5 deal with the effect of photons and protons on the pulmonary tissue, the next subsections will provide a brief outlook on the respective interaction mechanisms.

1.2.1 Photons interactions

Photons, in the form of x- or γ rays, are carriers of the electromagnetic radiation which undergo both elastic and inelastic scattering and are absorbed by the matter mainly via Photoelectric, Compton, Auger effects and Pair Production [7]. As a result, they indirectly ionize the cell DNA (i.e. the main cellular target for the ionizing radiation) by either releasing electrons of biological molecules (mainly H_20) and turning them into unstable radicals or by generating high energy electrons that can further interact with the target molecules. In this regard, photon irradiation is sparsely ionizing. Irrespective of the nature of the photon-matter interaction, the traversal of a volume of thickness x by N_0 photons will result in the "survival" of $N \leq N_0$ of them, according to the following equation

$$N = N_0 \cdot e^{-\mu x} \tag{1.2}$$

where μ is the absorption coefficient characteristic of the material.

The depth-dose profile for photon beams shows a distinctive shape, (see Figure 1.2) with an initial build-up region, whose position depends on the beam energy, caused by the Coulomb interactions and subsequent energy deposition of the secondary electrons. Since a decrease in the number of photons takes place at the same time, the delivered dose reaches a maximum at the end of the build-up region which is followed by an exponential decay.

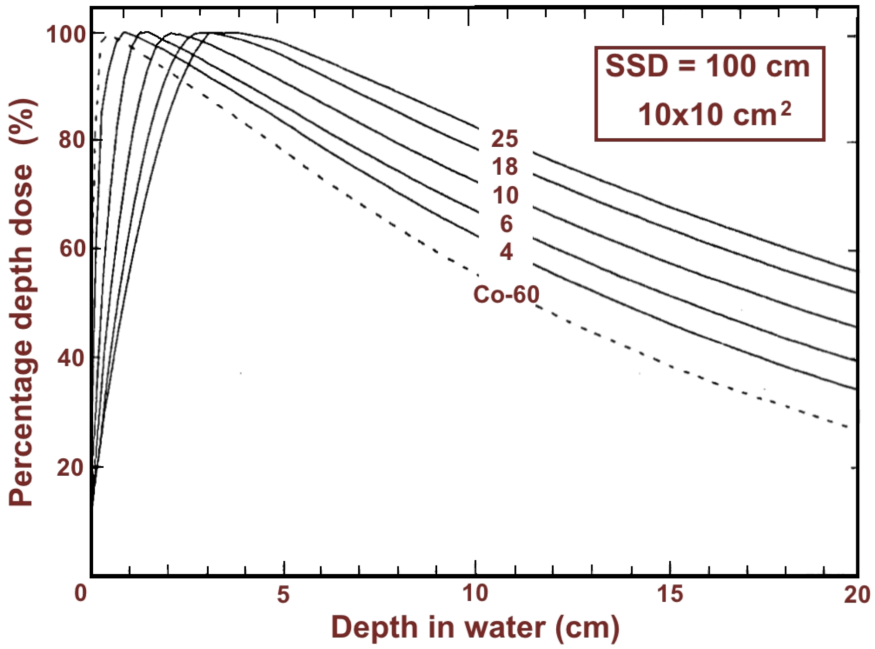

Figure 1.2: Percentage Depth-Dose distribution as a function of the depth in water for different photon beam energies. SSD=Source-to-Surface Distance.

Most clinical photon beams are generated through Bremsstrahlung radiation using linear accelerators and, at the typical (high) energies used in radiotherapy, the Compton effect dominates.

1.2.2 Protons and heavy ions interactions

Protons and, in general, charged particles, can generate dense ionization, meaning that they collide with and ionize thousands of atoms in a small volume, with mean free paths on the order of the DNA size.

The underlying reason resides in the interaction mechanisms of these particles, dominated by Coulomb interactions. As they travel through a medium, charged particles slow down and lose kinetic energy which is absorbed by the medium itself. The infinitesimal loss of energy dE in an infinitesimal path length dx due to Coulomb interactions is termed Linear Energy Transfer (LET) (SI units $keV/\mu m$)[7] and is modelled, for the interactions with the target electrons, by the Bethe-Bloch equation:

$$-\frac{dE}{dx} = 4\pi \frac{e^4 Z_p^4}{m_e v^2} \frac{N_A Z_t \rho_t}{A_t} \left[ln \frac{2m_e v^2}{< I > (1-\beta^2)} - \beta^2 \right] \tag{1.3}$$

where m_e, e and v denote the mass, charge and speed of the electron and β is the relative projectile speed. $< I >$ is the mean ionisation potential, N_a is the Avogadro number and $Z_{p,t}$ is the charge of the projectile/target.

Due to dependence on the speed (and therefore energy) of the projectile, as expressed by Equation 1.3, the LET of charged particles (with the exception of electrons) increases as they slow down, with most of their energy being released in a fraction of their path which corresponds to the so-called Bragg peak (see Figure 1.3) [8]. Moreover, for charged particles, direct ionization (i.e. damage of the cellular DNA molecule by direct ionization and excitation) dominates over the indirect one.

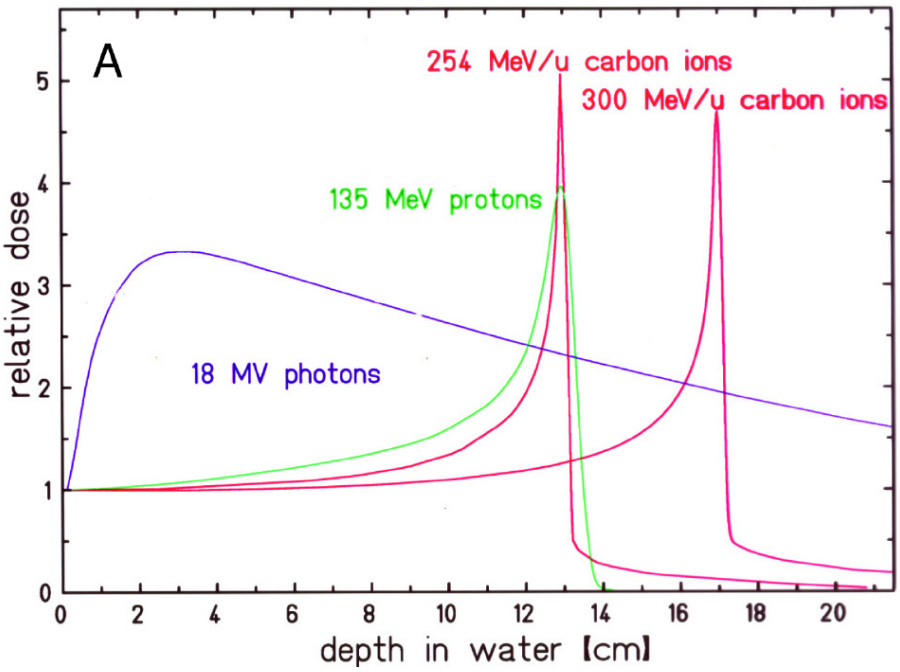

Figure 1.3: Relative Depth-Dose distribution as a function of the depth in water for photons, protons and carbon ions. Differences in range straggling at the same depth for different particles are visible. Figure from [8].

Different initial energies of the charged particle beams result in different positions of the Bragg peak, with deeper (but less pronounced) peaks for higher energies. However, as can be seen in Figure 1.3, differences in the projectile charge produce different depth-dose curves with the same target material. Protons, for example, show an increased range (and energy) straggling at the same depth of the Bragg peak with respect to Carbon ions.

The energy loss through multiple Coulomb interactions is a stochastic process described by a Gaussian

probability distribution with standard deviation given by

$$\sigma_{range} \propto \frac{1}{\sqrt{M}} \tag{1.4}$$

where M is the mass of the particle [8]. As a result, lighter particles (such as the protons) are more affected by range straggling. With carbon ions, however, the fragmentation of the projectile can be observed and leads to lighter fragments being generated in the collisions. Equation 1.3 shows that, with a little reduction in energy and speed, lighter particles (i.e. with lower Z_p) have a lower relative energy loss and can thus travel further, resulting in a characteristic long tail after the Bragg peak.

Finally, given the LET of a particle beam with fluence (i.e. number of particle traversals per perpendicular unit area) F the following relation holds

$$D[Gy] = 1.6 \cdot 10^{-9} \cdot LET \left[\frac{keV}{\mu m}\right] \cdot F \left[\frac{part}{cm^2}\right] \cdot \frac{1}{\rho} \left[\frac{cm^3}{g}\right] \tag{1.5}$$

from which the number of traversals needed to deliver a certain dose D can be computed.

1.2.3 Cellular radiobiology

The ultimate goal of RT is killing cancer cells and, to do so, radiation is exploited to damage the genetic material of the cells in its DNA and trigger mechanisms that eventually lead to the cell death. Although the death of a terminally differentiated cell might correspond to the loss of its functionality (such as the ability to perform gas-blood exchange in the epithelial cells of the lungs), the reproductive death, i.e. the inability to proliferate, represents the lack of survival for a stem cell. Such cells are said to be non-clonogenic, in that they are unable to generate new colonies. As such, their mere presence is not representative of tissue/tumour damage, but rather their colony-forming capability should be assessed [7]. While high doses ($>$ 100 Gy) are required to make non-proliferating cells non-functional (due to either the presence in multiple copies of the cell organelles, or the ability of the cell to regenerate them), 2 Gy are sufficient to induce enough damage to the DNA (which is unique) such that mitotic death or apoptosis are triggered. The clearance of a tumour via RT, therefore, translates to the shifting of the cancer-stem cells phenotype to a non-proliferating one.

The DNA, which resides in the cell nucleus, is a polymer made up of a sugar-phosphate backbone and nucleotides, assembled in a double helix on a nanometre scale. Although damages to the DNA can be grouped into three categories, namely base damages, Single Strand Break (SSB) and Double Strand Break (DSB), the first two are rarely lethal. Figure 1.4 shows the tracks of a proton and a carbon ion with the corresponding ionization events at the DNA scale.

As can be seen, heavier ions (such as carbon ions) are able to induce much more complex damages due to the extremely high ionization density that is observed around the particles' tracks. If we consider a cell nucleus with geometrical cross section A, for an ion beam with fixed LET, the Equation 1.5 shows a linear correlation between the number of particle traversals (i.e. the fluence F) and the delivered dose. Assuming that each traversal will result in one or more interactions between the particle and the nucleus content (i.e. the DNA), the probability density function of the number of hits n can be represented by a Poisson distribution, with average λ. If a single complex damage (i.e. a DSB) is enough to trigger the cell death, the cell survival is achieved only for $n = 0$ with probability given by $e^{-\lambda}$. As mentioned above, λ, the average number of hits, is linearly correlated with the delivered dose, which can thus be replaced to give $S = e^{-\alpha D}$, where S is the survival probability and α a radiosensitivity parameter. Finally, if two SSB, generated by two different tracks, are close enough, they can interact and generate a DSB, whose effect

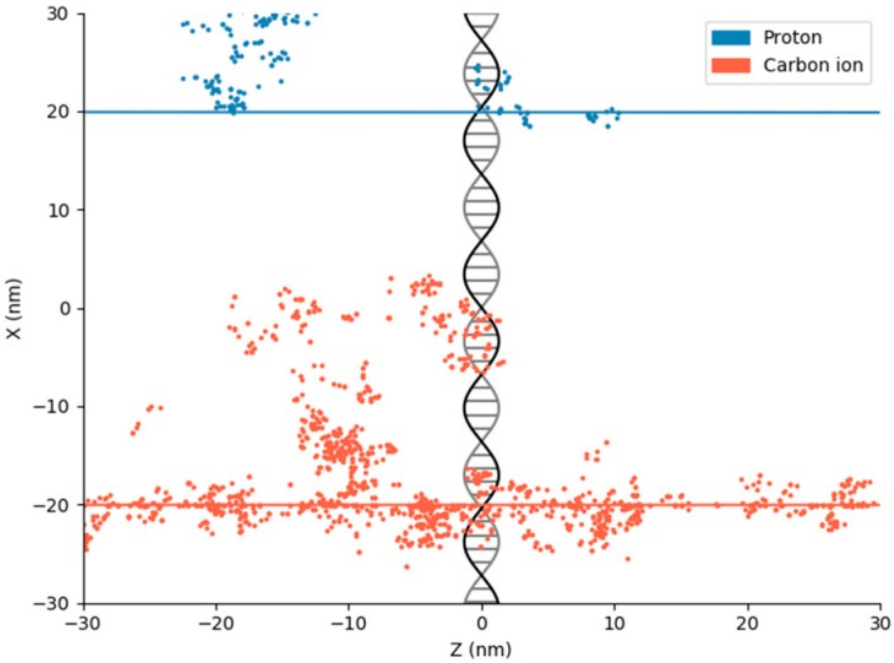

Figure 1.4: Different ionization densities for protons and carbon ions tracks at the DNA scale. Denser ionization for carbon ions is observed. Figure from [9].

can be taken into account in the previous equation to give

$$S = e^{-\alpha D - \beta D^2} \tag{1.6}$$

where β is another radiosensitivity parameter related to the occurrence of SSB coupling. Equation 1.6 describes the Linear Quadratic (LQ) model and the implications of this formulation can be seen in Figure 1.5. Experimentally, healthy single cells are seeded into dishes, irradiated and finally allowed to grow colonies which are counted to determine the actual surviving (i.e. clonogenic) fraction, as described earlier [7]. When the LQ model is employed to describe the cell surviving fraction, the ratio α/β can be used to fully characterize the radiosensitivity of cell lineages. For example, tumour cells, on average, have a high α/β ratio. As the radiosensitivity increases, the quadratic component of the cell killing becomes less and less important and single tracks are enough to induce DSBs. Consequently, low doses are sufficient to kill the cells: if cancer cells are more radiosensitive than the surrounding somatic ones, RT is able to damage the cancerous tissue while sparing the normal one. As the dose is increased, the difference between the surviving fraction of radioresistant and radiosensitive cells narrows, with the quadratic component of cell killing becoming dominant. The predictions of the LQ model, however, begin to diverge at high doses employed by some radiotherapeutic techniques in the clinics. Consequently, a universal survival curve model was developed [11] that assumes a multitarget description (where a single hit of multiple targets is required for cell killing to happen [12]) for doses higher then a certain threshold D_T.

The radiosensitivity of cell lineages is far from being constant, but it rather depends on both endogenous and exogenous (but not limited to the environment) factors that can alter the radiation response. It depends, for example, on the phase of the cell cycle, on the oxygen concentration, on the presence of radioprotectors/radiosensitizers and (with respect to the treatment) on the fractionation and the use of high-LET radiation. Among these modifiers, oxygen plays an important role as it can fix the indirect radiation damage to the DNA. In fact, an ionizing radiation field crossing the cell nucleus will not only

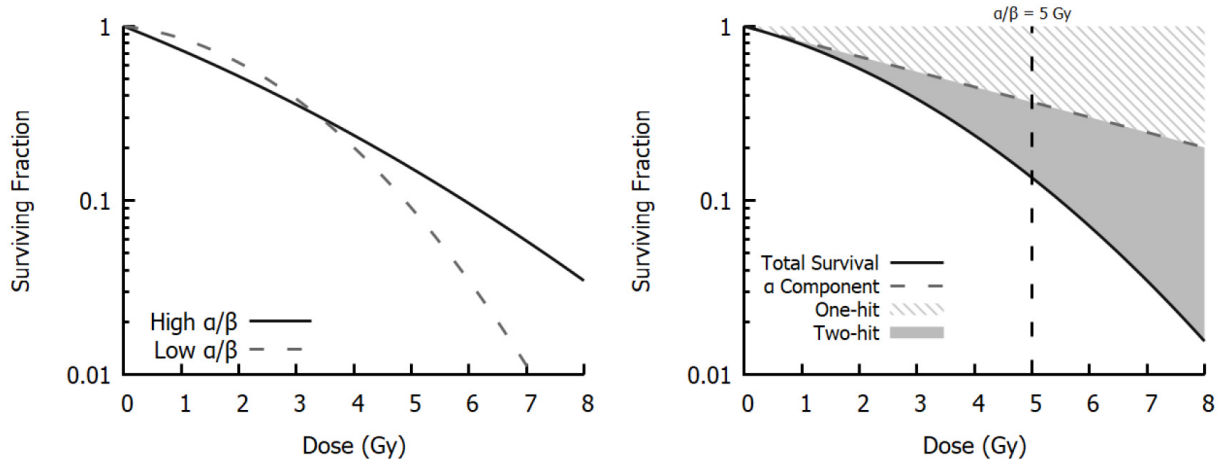

Figure 1.5: Surviving fraction as a function of the dose for different cells radiosensitivities. For higher α/β ratios, the linear component has more impact and lower survival is observed at low doses. On the right, the relative importance of the LQ model parameters in the cell survival curve. Figure from [10].

cause direct damage to the double helix, but also generate radicals. This process, which is dominant for x-rays (it accounts for about 70% of the total damage [13]), can indirectly damage the DNA as the radicals interact with and destabilize its backbone. In the presence of oxygen, the damage can be fixed with a stable change of the target that thus enhances the radiation efficiency. This boost is quantified by the oxygen enhancement ratio, defined as

$$OER = \frac{D_{hypoxic}}{D_{normoxic}}\bigg|_{isoeffect} \tag{1.7}$$

which measures the additional dose needed to obtain the same effect at lower-than-physiologic oxygen concentrations.

Another modifier of the radiation response, widely exploited in multiple radiotherapeutic modalities, is the dose temporal fractionation, consisting of prolonged treatments at low doses (usually between 2 and 3 Gy) equally spaced in time (usually 24 hours in the clinics). The rationale for this comes from the ability of somatic cells to relatively easily and quickly repair sublethal damages and thus behaving like unirradiated cells. If enough time between subsequent irradiations is allowed, radioresistant cells (see Figure 1.5) can recover and the ”shoulder” in the LQ model of surviving fraction can be repeated. This, overall, results in an increased sparing of the normal tissue for the same total delivered dose, with the survival given by

$$S = e^{-n(\alpha d + \beta d^2)} \tag{1.8}$$

where n is the number of fractions and d is the dose per fraction. Since the efficacy of the treatment schemes depends not only on the number of fractions, but also on their size, the total delivered dose is usually normalised to the equivalent dose in 2-Gy fractions that would result in the same biological effect, according to the following equation:

$$EQD2 = n \cdot d \cdot \frac{1 + \frac{d}{\alpha/\beta}}{1 + \frac{2}{\alpha/\beta}} \tag{1.9}$$

Equation 1.9 allows direct comparison of different treatment schemes by means of their respective EQD2.

The human cells possess 3 main mechanisms of DNA repair following a radiation-induced damage which differ by repair speed, precision and availability in the cell cycle phase (see Figure 1.6) [14]. Consequently,

although it is estimated that 1 Gy of (low LET) radiation can generate 40 DSB per cell [15], only a few are unrepaired or misrepaired and thus lethal for the cell. The first mechanism, named non-homologous end-joining, can quickly repair damages throughout the whole cell cycle, but is error-prone. Homologous recombination is, on the contrary, precise, but slow and necessitates of DNA templates which are available only during the S and G2 cell cycle phases. Finally, microhomology-mediated end-joining is very slow and highly error-prone, but can be used as a backup plan by the cell when the other repair mechanisms fail.

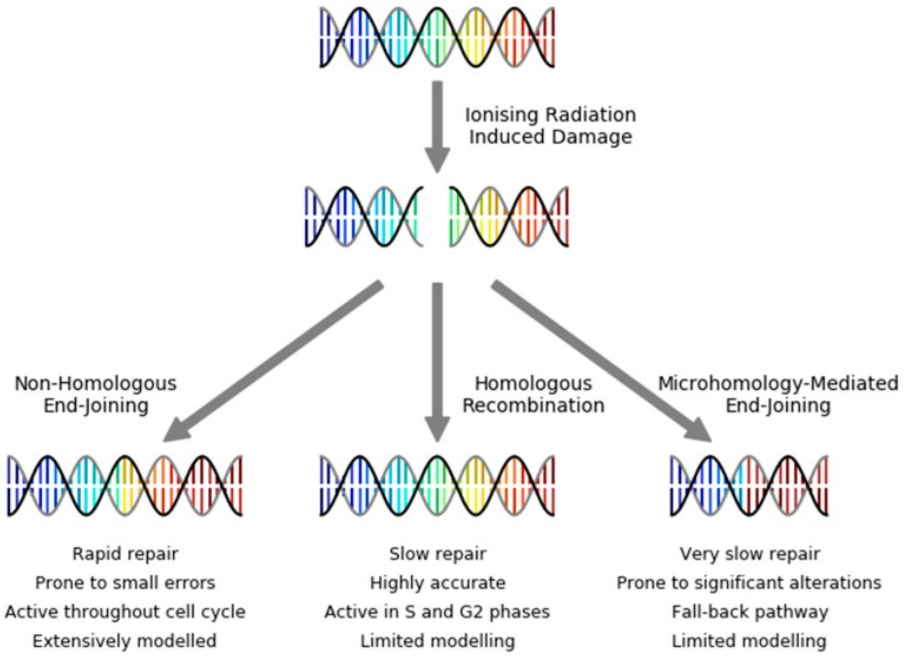

Figure 1.6: Main cellular DNA repair pathways following radiation-induced DSB. Figure from [9].

Failure to repair the DNA damages or misrepair will not always lead to the cell death, but also to its senescence. Cellular senescence, which plays an important role in the pathogenesis of RILI (see section Radiation-Induced Lung Injuries and Chapter 4), triggers a phenotypic shift characterized by a slow metabolism and the absence of mitosis and apoptosis [16]. Interestingly, it can be exploited in RT as it both stimulates bystander damage to the neighbouring cancer cells and limits the available space for the tumour growth.

In the clinical practice, favouring of a radiation quality over another requires comparisons. To this aim, the concept of Relative Biological Effectiveness (RBE) was introduced which measures the relative difference in terms of dose between two radiation fields (usually ions and photons as a reference) to achieve the same biological effect (such as the same cell killing) and is given by Equation 1.10 [17]. As can be seen in Figure 1.7, the RBE changes for different endpoints and, for the cell survival, it reaches its maximum at $D = 0$, while it tends to the unity for $D \to \infty$.

$$RBE = \left. \frac{D_{\gamma}^{ref}}{D_{ion}} \right|_{isoeffect} \tag{1.10}$$

The RBE is a complex parameter that encompasses multiple underlying physical and biological phenomena [17] and is used to convert the physical dose to the biological effective dose. Moreover, its dependence on the particle energy and speed (and therefore LET) causes it to vary along the beam path and imposes evaluations both in the plateau and peak regions when using charged particle (see Figure 1.3). While in

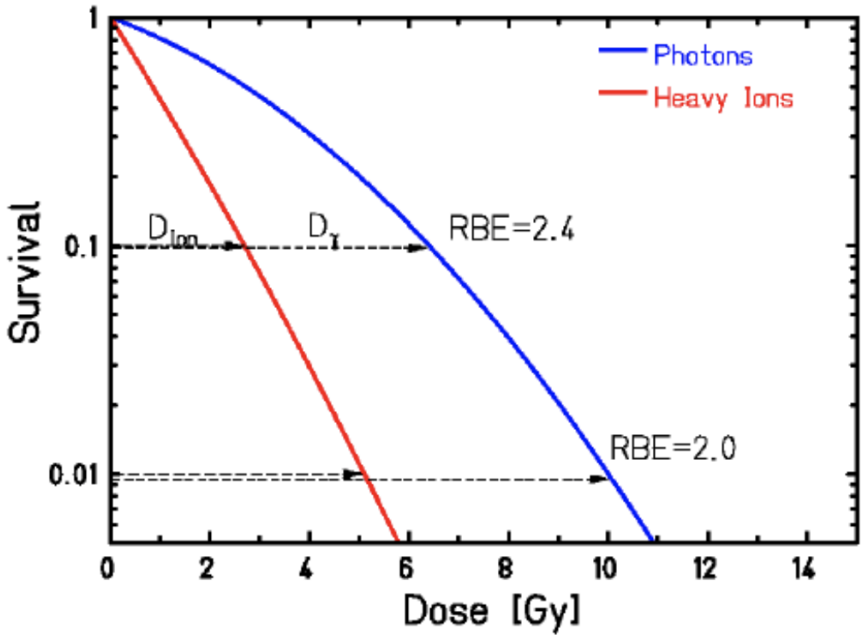

Figure 1.7: RBE for heavy ions and photons. For an isoeffect (i.e. same survival) a lower dose is needed for heavy ions with respect to photons.

the clinics it is assumed that photons and protons have a constant RBE of 1 and 1.1, respectively, for carbon ions at the Bragg peak this value is much higher. Multiple computational models have been developed to compute the RBE and, among them, the local effect model allows its computation for different ions and tumour types [18].

1.2.4 Radiation therapy techniques

In clinical practice multiple techniques are employed to maximise the dose delivered to the tumour while minimizing the dose to the Organ At Risk (OAR). Following an initial screening of the patient with, for example, a Computed Tomography (CT) scan, a treatment plan is created by contouring the Organ At Risk (OAR) and target volumes and by setting a prescribed dose for each region. An algorithm is then used to optimize the plan according to the constraints described above and with an inverse technique that determines the required dose distributions. A corresponding Dose-Volume Histogram (DVH), similar to that showed in Figure 1.8, is then generated, which reports on the y-axis the percentage of target volume (both for the tumour and the OAR) receiving at least the dose indicated by the value on the x-axis.

Among the most common RT techniques, 3D Conformal Radiation Therapy (3DCRT) is the least sophisticated, characterized by the employment of geometric field shaping alone (using, for example, multileaf collimators) to make it conformal to the target volume and the subsequent delivery from different angles. More advanced techniques include the Intensity Modulated Radiation Therapy (IMRT) which combines the geometric field shaping with the modulation of its intensity, thus providing improved sparing of the OAR without losses in the dose to the target volume (see Figure 1.8) [20]. In fact, as opposed to the uniform radiation intensity of the 3DCRT, in the IMRT the intensity can change between different fields and all of them are optimized at the same time during the treatment planning. Moreover, direct comparisons between the two techniques in Non-Small Cell Lung Cancer (NSCLC) patients showed lower rates of normal-tissue

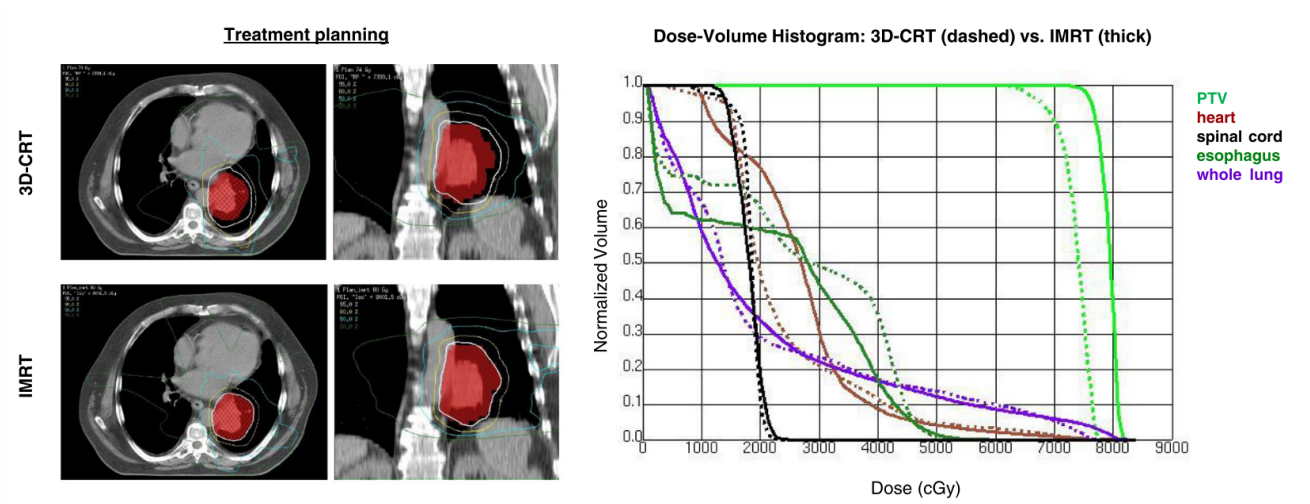

Figure 1.8: Treatment plan and DVH for 3DCRT and IMRT for NSCLC IMRT shows better OAR sparing and increased tumour dose with respect to 3DCRT.Figure from [19].

complications [21]. However, the use of Volumetric Modulated Arc Therapy (VMAT), an IMRT delivery techniques which employs a rotating gantry to deliver the dose in a 360-degree arc around the patient, resulted in increased toxicity with respect to standard IMRT in another NSCLC cohort study [22].

Finally, Stereotactic Body Radiation Therapy (SBRT) and Stereotactic Body Proton Therapy (SBPT) use photons and protons, respectively, in hypofractionated (i.e. high doses) regimes to damage small volumes of the target volume. This results in higher rates of normal-tissue sparing as the dose is distributed to multiple beamlets that converge at the target. It is usually employed in patients for which limited treatment options exist, such as early-stage NSCLC patients [23]. When charged particles are used, multiple Bragg peaks are superimposed by modulating the energy of each beam, so that they add up to a 3D flat dose distribution named spread-out Bragg peak.

1.3 Radiation-Induced Lung Injuries

Despite the advancements in RT techniques, complete shielding of the OAR remains unfeasible and, therefore, the probability that normal tissues will experience some complications is not negligible. This thesis focuses on the mechanistic modelling of the RILI, namely Radiation-Induced Pneumonitis (RIP) and RILF. This section provides a brief overview of the structure and physiology of the human lung and outlines the pathogenic mechanisms of the RILI. Additional details can be found in the introductory sections of Chapter 3 and Chapter 4.

1.3.1 The human lung

The respiratory system serves as an interface between the atmospheric gases and the human bloodstream. As such, its main functions are the filtration and transport of oxygen and carbon dioxide into and out of the body, respectively. Starting its path in the trachea, oxygen flows through the conducting (or proximal) airways until it reaches the transitional bronchioles (see Figure 1.9). From there, the oxygen diffuses to the hundreds of millions [24] of terminal alveoli that line the acinar (or distal) airways, where the proximity to the capillary network allows the gas-blood exchange to take place [25]. Together, proximal

and distal airways make up the tree-like structure of the lungs where the root, the trachea, branches (quasi-)dichotomously for about 20-25 generations. At each branching, two narrower daughter are generated and, between the transitional bronchioles and the alveolar sacs, the number of alveoli per segment increases with further generations. Finally, the acinar airways (that, together with the transitional bronchioles, constitute the parenchyma of the lungs) are named after the acini, respiratory units segmented into alveolar ducts where all the airways participate in gas-blood exchange [26].

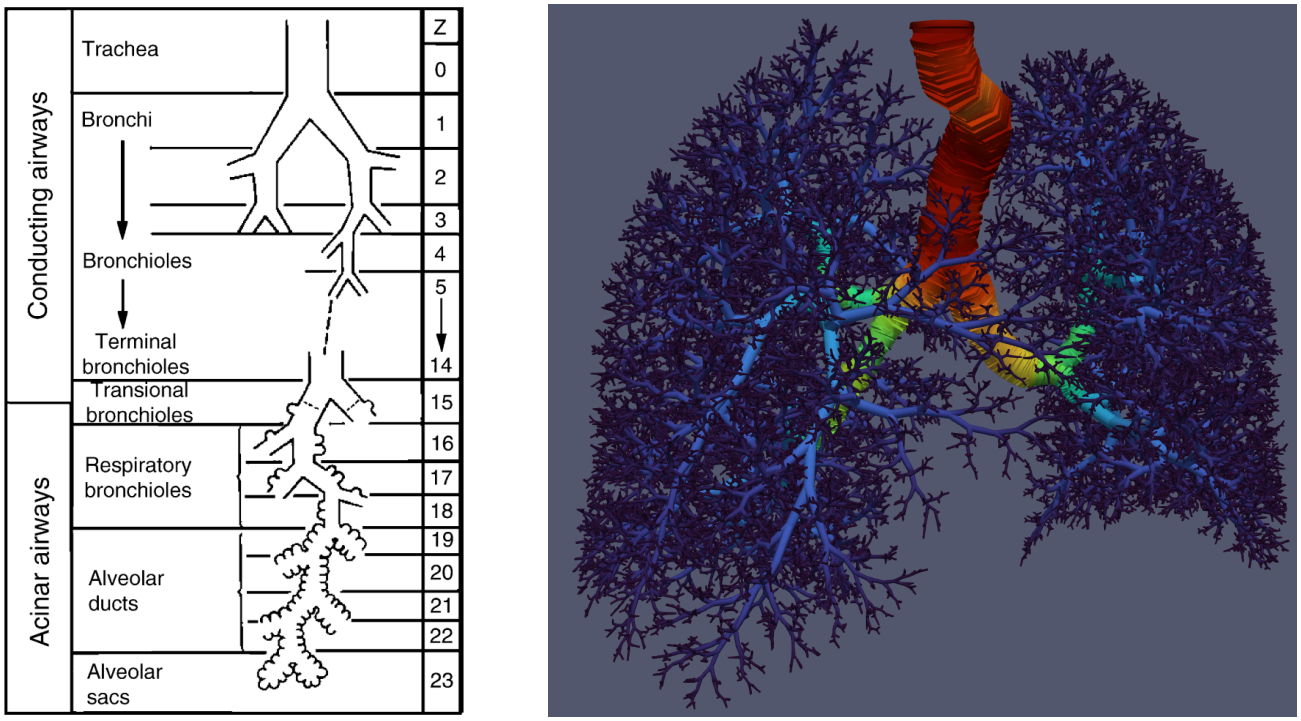

Figure 1.9: Models of the human airways. **A** Proximal and distal airways as a dichotomic tree through 24 generations. Figure from [27]. **B** Model of the entire human lungs color coded according to the airways diameter (darker colors for narrower segments).

At the cellular scale, the cell population of the respiratory system can be roughly categorized as follows: epithelial cells (with a further distinction between those in the airways, such as basal, goblet, club and ciliated cells, and those found in the alveoli only), endothelial cells (such as arterial and capillary cells) and stromal cells (such as smooth muscle cells, mesenchymal cells) [28]. Narrowing the focus to the alveoli, whose shape can be approximated by an hollow sphere, the main cell types are the Alveolar Epithelial Cells of type 2 (AEC2), which serve as stem cells and can differentiate into the Alveolar Epithelial Cells of type 1 (AEC1), the AEC1, which are terminally differentiated and form the air-blood barrier, the alveolar macrophages which patrol the environment inside the alveolus and take part in the immune response, the endothelial cells, which constitute the blood network that lines the alveoli, and the interstitial cells, such as fibroblasts and myofibroblasts, which synthesize structural components of the ExtraCellular Matrix (ECM) [29]. (see Figure 1.10A).

1.3.2 Pathogenesis of RILI

The relatively high sensitivity of the lungs and, in particular, of the alveolar region, makes them susceptible to radiation-induced damage and, consequently, limits the lethal doses that can be delivered to the thoracic

region [30]. The avoidance of such effects implies limitations in terms of both the Mean Lung Dose (MLD) and the fraction of irradiated volume, which hamper effective treatments.

Following the interaction of the ionizing-radiation with the alveolar tissue, direct and indirect damage (through, among others,Reactive Oxygen Species (ROS)) to the DNA of the epithelial and endothelial cells can either trigger their apoptosis or a phenotypic shift to a senescent state (see Figure 1.10). As a result, the cell loss narrows the alveolar septum, limits the surfactant production and the overall vascular integrity is reduced (causing pulmonary edema). This acute phase, which takes place in the first minutes to hours after the damage, is followed by a subacute reaction characterized by inflammation. The senescent cells, unable to repopulate the depleted regions, acquire the so-called senescence-associated secretory phenotype and secrete factors, such as the Monocyte chemoattractant protein 1 (MCP1), the Transforming Growth Factor Beta (TGFβ) and the Tumour necrosis factor alpha (TNFα), that attract inflammatory cells , like the Monocyte-derived Macrophages (M0), that differentiate into Alveolar Macrophages of type 1 (M1) and Alveolar Macrophages of type 2 (M2). Additional secretion of chemokines and cytokines from these cells, including Platelet-Derived Growth Factor (PDGF), Interleukin 13 (IL13) and the already mentioned TGFβ, cause more damage to the neighbouring cells and the infiltration of inflammatory cells (such as neutrophils and lymphocytes), recruited by those already present, is facilitated by the abnormal vascular permeability. In parallel, chemical and mechanical signals coming from the disrupted environment stimulate the Endothelial to Mesenchymal Transition (EndMT) and the Epithelial to Mesenchymal Transition (EMT) which enlarge the population of myofibroblasts. This phase, which coincides with the RIP, can last several months and yet is reversible. Symptoms usually include dyspnea, mild fever and non-productive cough [31]. However, if not resolved, the increased proliferation, migration and differentiation into myofibroblasts of the fibroblasts, mainly caused by the elevated amount of TGFβ, which senescent cells and M2 secrete, lead to a permanent change of the alveolar structure. This alteration, which is caused by the exaggerated secretion of ECM by the myofibroblasts, establishes the RILF, characterized by the stiffening and scarring of the alveoli which can result in pulmonary failure and eventually death.

Although the occurrence of RILI is not uncommon (with up to 25% of incidence in patients irradiated in the thoracic region [23]) a full understanding of its onset and development is lacking and some modelling efforts, both on the computational and animal level, are often based on data from patients suffering from IPF. The two diseases, in fact, show some similarities, although the causes of the IPF are currently unknown.

1.3.3 Risk factors

The onset and extent of RIP (and it's potential worsening to RILF) can be influenced by treatment-, disease-/cancer- and patient-related risk factors. Indeed, technological advancements both in terms of treatment planning and delivery systems, such as the aforementioned IMRT, VMAT and SBRT [20], have resulted in lower incidences of RIP and help preventing the disease [21], but additional constraints could be inferred by matching the corresponding DVHs to clinical end points. Specifically, constraints on the MLD and on the irradiated volume can be specified. The treatment-related risk factors that have proved to have the most predicting power for the onset of the RIP are $V_{20} \geqslant 30 - 35\%$ (i.e. 30%-35% of the total irradiated volume receiving more than 20 Gy), $V_5 \geqslant 65\%$, MLD $\leqslant 20Gy$ [33, 34, 35, 36].

Concerning the disease-/cancer-related risk factors, both the tumour (target) location and volume have been correlated with the onset of RILI. Multiple retrospective studies have shown increased frequency of RIP in patients irradiated in the lower lobe [36, 37]. Potential explanations include the higher range of motion (which can thus reduce the treatment precision and/or increase the irradiated volume) or an increased cell radiosensitivity. As for the volume, in patients with bigger tumours a higher incidence of RIP has been documented, most probably due to the increase in the size of healthy lungs irradiated [38, 39]. Furthermore, the proximity of the lung to the heart and, consequently, the portion of irradiated heart,

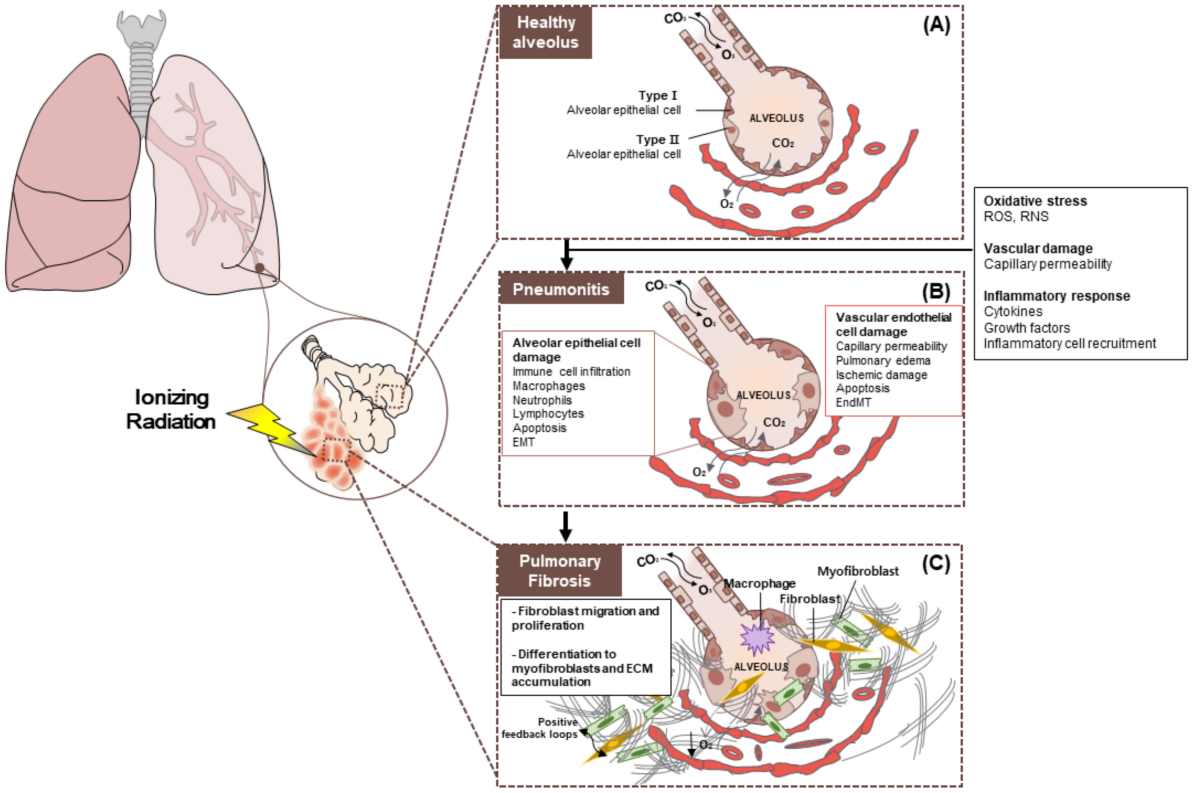

Figure 1.10: Pathogenesis of RIP and RILF. **A** In the healthy alveolus the gas-blood exchange takes place thanks to the AEC1 population which is maintained by the AEC2. **B** Ionizing radiation can damage both the epithelial and endothelial cells, promoting tissue disruption and infiltration of inflammatory cells, a condition termed pneumonitis **C** If not resolved, chronic inflammation leads to tissue scarring as the mesenchymal population is increased (via fibroblasts differentiation, EndMT and EMT) and secretes exaggerated amounts of ECM. Figure from [32].

proved to be correlated with higher risks of developing RIP and RILF [40].

Finally, patient-related characteristics that have been shown to influence the probability of developing RILI are the age [41], the health status, the presence of comorbidities [42] and the smoking history [23]. Older age ($\geqslant 50-60$ years), a worse overall health status, presence of chronic obstructive pulmonary disease or interstitial lung disease and currently being (or have been) a smoker are all risk factors associated with a higher risk of developing RIP. However, some studies have shown increased damage resistance from RT in the lungs of smokers probably due to the already damaged epithelium [43]. Interestingly, the role of sex has not been fully clarified and the results are controversial.

1.3.4 Clinical assessment

RIP is a disease that requires clinical diagnosis and to date no laboratory test can identify it without some level of uncertainty. Other diseases, such as the aforementioned obstructive pulmonary disease and the interstitial lung disease might be misdiagnosed as RILI, but pulmonary function tests can be employed to distinguish them. The Radiation Therapy Oncology Group [44] and the Common Terminology Criteria for Adverse Events [45] are the most widely used scoring systems in clinical practice (see Table 1.1 for the

RILF). They categorize RIP and RILF patients based on the severity of their symptoms and image findings and while the first disease usually develops within 6 months from the treatment, the latter is manifested later and can develop over the course or multiple years.

Grading scale	Grade 1	Grade 2	Grade 3	Grade 4	Grade 5
CTCAE v5.0	Radiologic pulmonary fibrosis < 25% of lung volume associated with hypoxia	Evidence of pulmonary hypertension; radiographic pulmonary fibrosis 25–50% associated with hypoxia	Severe hypoxia; evidence of right-sided heart failure; radiographic pulmonary fibrosis > 50–75%	Life-threatening consequences (e.g. hemodynamic/pulmonary complications); intubation with ventilatory support indicated; radiographic pulmonary fibrosis > 75% with severe honeycombing	Death
RTOG	Asymptomatic or mild symptoms (dry cough); slight radiographic appearances	Moderate symptomatic fibrosis (severe cough); low grade fever; patchy radiographic appearances	Severe symptomatic fibrosis; dense radiographic changes	Severe respiratory insufficiency/ Continuous O2/ Assisted ventilation	Death

Table 1.1: Grading scales used in clinical practice for the RILF. CTCAE v5.0 Common terminology criteria for adverse events, version 5.0 [45], RTOG Radiation Therapy Oncology Group [44], EORTC European Organization for Research and Treatment of Cancer

Although chest radiographies can help in the detection of early signs of RILI, CT scans are preferred in the clinics due to their higher sensitivity. Moreover, early and late CT changes can be distinguished which characterize the subacute and chronic phases of the RILI. Among the former, different patterns, appearing 3-4 weeks after the end of the irradiation period, have been identified, such as: diffuse and homogeneous increase in the attenuation of the pulmonary parenchyma, diffuse ground-glass opacity, patchy consolidation and/or ground-glass opacity [46]. CT findings in the RILF phase, identifiable 6-12 months after the irradiation with stabilization within 2 years [20] can, instead, include: volume loss, bronchiectasis, architectural distortion, mass- or scar-like opacities around the tumour (in-field) or in the region of the tumour [20, 46] (see Figure 1.11). Both focal and diffuse aggregations can be observed, with transitions from patchy to solid/discrete consolidations [47]. However, while in asymptomatic patients radiological changes might manifest, in symptomatic patients these changes might require years to develop [20]. Other modifications observable in later stages include, for example, crazy-paving patterns over backgrounds of ground-glass opacities [48] caused by septal thickening.

From a quantitative point of view, multiple studies have identified common patterns and shifts in the overall radiodensity of the lungs. In fact, from the analysis of follow-up CT scans registered to the radiation planning CT, both temporal patterns and dose-density relations (in terms of Hounsfield Units (HU)) were found. Among these, the density change as a function of the dose has proved to follow a sigmoidal curve after VMAT and IMRT when averaged over all time points and when constrained to month-long periods

a. b.

Figure 1.11: Follow-up CT scans showing RILI. **A** Appearance of ground-glass attenuation and nodules in the right upper lobe 4 months after RT. **B** RILF next to the chest wall 26 months after completion of RT.Figure from [49].

after the irradiation [31, 50, 51, 52]. Moreover, two distinct components in the time evolution of the total density change were outlined after IMRT for multiple dose ranges, with a peak in the early phase between 3 and 6 months followed by a reduction and a constant progression [31, 53]. Interestingly, two patients cohorts treated with either SBRT or SBPT showed similar radiographic endpoints, though the inflammatory responses had different dynamics [54]. Finally, it is worth mentioning that physiological and molecular changes in mice treated with RT that developed RILF have been correlated with the decrease in functioning lung volume and the increase in the average lung density [55]. Surrogates of these quantities, which have been condensed under a Fibrosis Index (FI), are discussed in more detail and used as estimators of the severity of the RILF in Chapter 4 and Chapter 5.

1.4 Normal Tissue Complication Probability Models

In the clinical setting, different treatment plans can be quantitatively compared by the doctors via the corresponding dose-response curves which act as interfaces to the underlying biophysical models. The dose-response curves, in turn, are derived from the models that perform best when fitting a clinical dataset. In fact, the ultimate goal of RT is the widening of the therapeutic window, defined as the region between the dose-response curves of the tumour, the Tumour Control Probability (TCP), and that of the normal tissue, the Normal-Tissue Complication Probability (NTCP). This section provides an overview of some of the existing NTCP models, together with the main assumptions and differences.

When NTCP models are built, the focus is shifted from the response of a single/few cells to that of a whole tissue. However, it must be noted that injury and radiation-induced morbidity are different outcomes and clinical symptoms may not arise despite severe treatment differences. As an example, the responses of the pulmonary tissue can change abruptly and the total dose can be increased substantially in light of a reduction in the irradiated volume or the use of a temporal fractionation scheme [56]. As discussed in the previous sections, when radiation-induced damage to the pulmonary tissue is taken into account, RIP and RILF are the main potential outcomes for which complication probability curves can be defined. It is worth noting that tissues can be classified as early- or late-responding depending on the relative shape

of their dose-response curve [7]. In fact, early-responding tissues are characterized by fast-proliferating cells that result into early appearances of the irradiation effects. This tissues have high α/β ratios and thus high radiosensitivity as the fast turnover leads to the exposition to the irradiation of more cells during sensitive phases of the cell-cycle. Tumours and skin, for example, are early-responding tissues. Conversely, late-responding tissues, such as the lungs and the heart, are characterized by larger ratios of functional cells which can thus survive if not stimulated to proliferate. Thanks to this feature, they show lower α/β ratios and are susceptible to changes in temporal fractionation schemes. Consequently, their response to low-dose fractions is low, as opposed to that of early-response tissues, and makes them perfect candidate for the sparing effects of the hyperfractionation schemes [10].

NTCP can be broadly categorized into two main classes: phenomenological and mechanistic. While models in the former class make no assumptions on the underlying biological mechanisms and focus on fitting existing population or individual clinical data, those in the latter are built on radiobiological foundations and take into account aspects of the tissue architecture [57]. Moreover, the mechanistic ones can be further categorized depending on the nature of the response they simulate. As a side note, recently the use of data-driven approaches (such as machine learning-based, which take a step further from the phenomenological models) has been explored [58], where from large amount of data patterns are learnt and features recognized that can help in the prediction of normal-tissue toxicities.

1.4.1 Phenomenological models

The first observations on dose-response curves date back to 70 years ago [59] and yet, despite the overall advancements in the field, nowadays there is general consensus about the originally proposed "s-shape" (i.e. a sigmoid) [60]. When this shape is interpreted as a potential cumulative distribution, it points to an underlying probability distribution of the threshold of the damage-inducing dose in a population of patients, resulting from the intrinsic radiosensitivities and the stochasticity of the energy deposition [57]. If such a probability distribution, $p(x)$, exists, then a general mathematical definition of the NTCP can be written as in Equation 1.11, where D represents the delivered dose.

$$NTCP(D) = \int_{-\infty}^{D} p(x)dx \tag{1.11}$$

In this regard, multiple formulations of $p(x)$ have been proposed and all of them, when integrated, result in slightly different "s-shaped" dose-response curves such as the probit, the logistic, the log-logisitic and the Poisson models. Due to their similarity, the use of a model rather than the others, which were derived from the normal, logistic, log-logistic and Poisson distributions, respectively, is dictated mainly by the ease of application with a given pool of clinical data. However, for comparison purposes the different dose-response curves are often parametrized (and fully characterized) by two parameters. The first one, D_x, is a position parameter used to indicate the dose required to induced a response x. Typical values for x are 50 and 37 (an approximation of e^{-1}) for which D_x is written as D_{50} and D_{37}, respectively. The second parameter, γ, was introduced in [61] and is related to the steepness of the dose-response curve via the following relation:

$$\gamma = D \cdot \frac{dNTCP(D)}{dD} \tag{1.12}$$

γ is thus a dimensionless number that measures how much the NTCP will change, relatively, following a 1% change in the delivered dose, normalized by the dose [61]. For characterization purposes, γ, the scale parameter, is typically provided at the maximum gradient, such as $\gamma_{max} = \gamma_{50}$. It's worth noting that the dose at which γ reaches its maximum value is higher than the one at which the gradient of the dose-response curve ($dNTCP(D)/dD$) is maximum and the two shouldn't be confused [57]. Moreover,

D_x and γ, which can be fitted to the available clinical data, are specific for each organ and will depend on the endpoint considered.

The Lyman model [62], further improved by Kutcher & Burman [63] and then Mohan [64], is the most widely used NTCP model in clinical practice. It is rooted in the probit model which assumes that the radiosensitivity of a population of patients follows a normal distribution [59], given by

$$p\left(D|\mu,\sigma\right) = \frac{1}{\sqrt{2\pi}\sigma} exp\left[-\frac{1}{2}\left(\frac{x-\mu}{\sigma}\right)^2\right] \tag{1.13}$$

where μ and σ are the mean and standard deviation of the distribution. Using Equation 1.11, the NTCP for the probit model reads

$$NTCP\left(D|\mu,\sigma\right) = \frac{1}{\sqrt{2\pi}} \int_{-\infty}^{\frac{D-\mu}{\sigma}} exp\left(-\frac{x^2}{2}\right) dx \tag{1.14}$$

which can be rewritten using the aforementioned parametrization, with D_{50} and γ, as

$$NTCP\left(D|D_{50},\gamma_{50}\right) = \frac{1}{2}\left\{1 - erf\left[\gamma_{50}\sqrt{\pi}\left(1-\frac{D}{D_{50}}\right)\right]\right\} \tag{1.15}$$

where erf is the error function defined as $erf(t) = \frac{2}{\pi}\int_0^t e^{-x^2}dx$.

Although the strength of the probit model relies in its simplicity as it provides a tool for direct estimates of the effect of independent sources of uncertainty (such as the radiosensitivity or the delivered dose) on the resulting NTCP, it assumes an homogeneous irradiation of the whole organ. Based on previous observations on the volume-effect [65], that is, smaller volumes can tolerate higher doses and the experimental data support the existence of power law, Lyman [62] modified the probit model accordingly. In the new formulation, the tolerance dose (such as the D_{50}) is a function of the irradiated volume given by $D_x(V) = D_x(1)\cdot V^{-n}$, where $D(1)$ is the potential dose delivered to the full organ that would result in the same response, V is the fraction of the volume that is treated and n, typically bounded in the interval [0,1], is a fitted parameter that controls the strength of the volume-effect. Lower values of n reduce the relative contribution of the volume factor and indicate that the effect is mainly driven by the maximum delivered dose. Conversely, for values of n close to 1, the volume-effect becomes stronger. Moreover, the standard deviation σ of the probability distribution of the radiosensitivity is approximated by $m\cdot D_{50}(V)$, where m is another free parameter. These adaptations are combined in the new NTCP formulation, which reads:

$$NTCP\left(D,V|D_{50},m,n\right) = \frac{1}{\sqrt{2\pi}}\int_{-\infty}^{t} e^{-x^2}dx \tag{1.16}$$

where $t = \frac{D-D_{50}(V)}{m\cdot D_{50}(V)}$ and $D_{50}(V) = D_{50}(1)\cdot V^{-n}$.

Since the Lyman model can estimate the NTCP only for homogeneously, although even partial, irradiations, the Kutcher-Burman [63] reduction scheme can be used to calculate an effective volume V_{eff} irradiated to the maximum dose in the organ, D_{max}, by transforming an inhomogeneous DVH into a single-step histogram. Given N histogram bins where the $i-th$ bin has height (i.e. fractional volume) V_i and is centred on the dose D_i , the reduction scheme is given by

$$V_{eff} = \sum_{i=1}^{N}\left(\frac{D_i}{D_{max}}\right)^{\frac{1}{n}}\Delta V_i \tag{1.17}$$

When V_{eff} and D_{max} are used in the Lyman formulation of the NTCP, the model is called Lyman-Kutcher-Burman model.

An alternative formulation, proposed by Mohan [64], suggests the use of the Equivalent Uniform Dose (EUD) which, delivered uniformly to the whole organ, would result in the same complication probability as that of the D_{max} delivered to the partial volume given by V_{eff}. A reduction of the DVH is bypassed in this case and rather the dose to the irradiated voxels is used. The EUD is defined as follows

$$EUD = \left(\sum_{i=1}^{N} V_i D_i^{1/n} \right)^n \tag{1.18}$$

The NTCP is then given by Equation 1.16, where D is replaced by EUD.

1.4.2 Mechanistic models

The radiobiological knowledge lays the foundations of the mechanistic approach, where cell dynamics and/or tissue architecture are employed to provide a more concrete representation of the mechanisms underlying the dose-response curve. Among them, the Poisson model (for TCP, but the description can be easily adopted for NTCP modelling) assumes that tumours can be eradicated only when all the clonogenic cells (i.e. the cancer stem-like cells) are killed [66]. Therefore, larger doses are needed for larger populations. Analogously, a normal tissue (or a portion of it) will survive if it will not be depleted of all its stem cells. With a similar reasoning as that shown in Subsection 1.2.3, based on the assumptions that the target of cell survival is the cell DNA, hits are independent and a single hit is enough to induce the mitotic death of a cell, following an irradiation to the dose D the number of hits in a cell will be distributed according to a Poisson distribution and thus the probability of cell survival, S corresponding to 0 hits, can be written as:

$$S(D) = e^{-D/D_0} \tag{1.19}$$

where for $D = D_0$ the survival is lowered to 37% and results in a log-linear cell survival curve. If the initial number of stem cells is N_0, those that will survive an irradiation to the dose D will be:

$$N(D) = N_0 e^{-D/D_0} \tag{1.20}$$

Under the assumption that, due to differences in radiosensitivity and dose deposition, some statistical variations from one tumour/normal tissue to another will be observed and that cells will undergo mitotic death independently (which is a strong simplification), the number of surviving cells will also follow a Poisson distribution, where Equation 1.20 can be used as a parametrization. Assuming that tumour control and, equivalently, normal tissue complication is achieved with 0 survival, the Poisson NTCP reads

$$NTCP(D|D_0) = e^{-N_0 exp(-D/D_0)} \tag{1.21}$$

For comparison purposes, Equation 1.21 can be reparametrized using γ and D_x, as mentioned in the previous section. Equating the second derivative of Equation 1.21 to 0,provides the maximum value of its gradient. At this value, the dose corresponds to NTCP$=37\%$, indicated by D_{37}. These values can be combined to give

$$\gamma = \frac{ln(N_0)}{e} \tag{1.22}$$

and

$$D_x = D_0 \left[e\gamma - ln\left(ln(100) - ln(x) \right) \right] \tag{1.23}$$

Finally, for $D = D_{37}$ the NTCP is given by

$$NTCP\left(D|D_{37}, \gamma\right) = e^{-exp[e\gamma(1-D/D_{37})]} \tag{1.24}$$

The work of [67], which provides a simpler version of the Poisson model, formulated using base 2 instead of e, places greater emphasis on the tissue architecture. Within it, the relative seriality model is presented, based on the concept of the Functional Subunit (FSU)s, borrowed from a previous study [68]. An FSU is the largest amount of tissue (or pool of cells) that can be regenerated from a single surviving stem cell while retaining its function and can be described either morphologically (in anatomical terms, examples are the nephrons in the kidneys) or functionally (i.e. with respect to its repair capabilities). Although general consensus on the definition of an FSU for a specific organ or tissue might not exist (in the lungs, for instance, both the acinus [69] and the alveolus [70] have been previously identified as potential FSUs, where the ability of the stem cells to migrate and repopulate a certain region was questioned. However, the latter is used in the models of RILF presented in this thesis), there's agreement on the assumption that FSUs can be structurally arranged either in parallel, serially or as a mixture of the two [67] (see Figure 1.12). An example of serial arrangement is the white matter in the spinal cord [68], where the loss

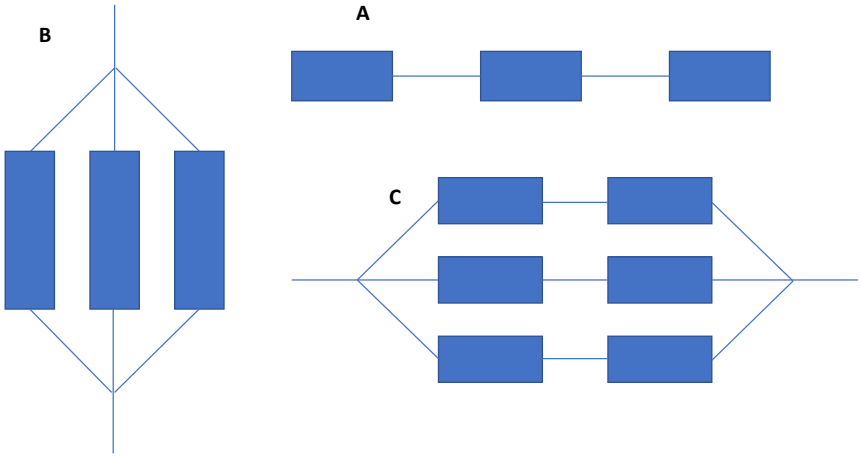

Figure 1.12: FSU architectures. **A** Serial arrangement. **B** Parallel arrangement. **C** Mixed arrangement.

of a single FSU would result in the failure of the tissue, or, equivalently, the saturation of the dose-response curve which would closely resemble a quantum response [68]. For these organs, survival has a stronger dependence on the number of clonogenic cells per FSU, as all of them must be killed for a critical reaction to occur. Conversely, parallel organs, such as the lungs, heart and liver, have many FSUs performing the same actions in parallel and the overall organ function can be retained if only a few of them are depleted. However, the loss of FSUs inevitably results in an increased workload for the surviving ones and a threshold can be defined for the minimum amount of undamaged tissue (or number of surviving FSUs) needed for an organ to maintain its functionality. This threshold, named functional reserve, is usually high for parallel organs and close to 1 for the serial ones. Alternatively, using the concepts provided in the previous section, it can be asserted that parallel organs have a stronger volume effect, with coefficient n close to 1 (see Equation 1.17 and Equation 1.18), while for purely serial organs the maximum dose plays a bigger role on the overall survival. Finally, in mixed architectures FSUs are arranged both in parallel and serially and, in reality, tissues (especially the normal ones) have this structure (or can be modelled as such). Having this in mind, it is clear that tissue survival (either NTCP or TCP) can't be described solely in terms of cell radiosensitivity, but the FSUs arrengement (i.e. the tissue architecture) must also be taken into account. In light of these assumptions, tumours have predominantly a parallel structure since all the clonogenic cells must be eliminated to achieve tumour control [67].

When modelling NTCP, the relative seriality model [67] assumes different formulations, depending on

the architecture of the organ. For serial organs, a complication will occur if at least one FSU is damaged. This can be modelled as

$$NTCP = 1 - \prod_{i=1}^{M} \left(1 - p_i\left(d_i\right)\right) \tag{1.25}$$

where M is the number of FSUs, d_i and p_i are the dose and the survival probability of the $i-th$ FSU, respectively. Conversely, for parallel organs all the FSUs must be killed for a normal-tissue complication to take place, modelled as

$$NTCP = \prod_{j=1}^{N} p_j\left(d_j\right) \tag{1.26}$$

where N, d_j and p_j are equivalent to the parameters of the previous definition. Finally, the formulations presented above can be combined to give the NTCP for mixed organs with M connections in series and N connections in parallel exposed to a non-uniform dose distribution, as follows

$$NTCP = \prod_{j=1}^{N} \left[1 - \prod_{i=1}^{M} \left(1 - p_{ij}\left(d_{ij}\right)\right)\right] \tag{1.27}$$

Assuming that all the FSUs are equivalent and thus have the same complication probability $p_{ij}\left(d_{ij}\right) = p\left(d_{ij}\right)$ and using the relative seriality coefficient $s = \frac{M}{M \cdot N} = \frac{1}{N}$ proposed by [67], with V_i relative volume of the $i-th$ FSU, the NTCP can be rewritten as

$$NTCP\left(D|s,V\right) = \left[1 - \prod_{i=1}^{N} \left(1 - p\left(d_i\right)^s\right)^{V_i}\right]^{\frac{1}{s}} \tag{1.28}$$

Finally, the (individual) critical volume model [69, 71, 72, 73] emphasizes the role of the stem cells in the formulation of the NTCP, merging concepts from the aforementioned representations and inspiring the definition of the RILF Severity Index (RSI) presented in Chapter 4. The model assumes that the architecture of the majority of normal tissues is somewhere in between serial organs (with a critical element) and fully parallel organs (i.e. tumours) and that given a certain total number of FSUs N, at least M (i.e. the critical volume) must be damaged to observe loss of functionality in the organ. Moreover, each FSU has k stem cells with radiosensitivity defined by LQ model (i.e. the α and β parameters) and the FSU is killed when depleted of all of them [72]. Under these assumptions, the NTCP, formulated in terms of the cumulative binomial probability, is given by

$$\begin{aligned} NTCP\left(D|\alpha,\beta,M,N,k\right) = \sum_{t=M+1}^{N} \binom{N}{t} P_{FSU}^{t}\left(1 - P_{FSU}\right)^{N-t} = \\ \sum_{t=M+1}^{N} \binom{N}{t} \left[\left(1 - exp\left(-\alpha D - \beta D^2\right)\right)^k\right]^t \left[1 - \left(1 - exp\left(-\alpha D - \beta D^2\right)\right)^k\right]^{N-t} \end{aligned} \tag{1.29}$$

It's worth noting that Equation 1.29 assumes an homogeneous dose distribution and identical FSUs, but alternative formulations of the model for population responses and/or non-homogeneous irradiation have been implemented as well [73]. Finally, for large values of M and N, Equation 1.29 can be approximated by a normal distribution.

1.4.3 Modern modelling approaches in radiobiology

The modelling approaches outlined in the previous sections present some limitations as, for instance, cellular dynamics (including damage repair and repopulation) is not taken into account [69] and disease progression as a function of time as well as bystander-induced damage can't be replicated [74]. Furthermore, DVHs, used as inputs for the predictions, hide information regarding the spatial distribution of the dose [75] and can potentially prevent the delivery of higher doses to the tumour, especially when highly conformal techniques are used. This lack of spatial information about the dose distribution poses additional concerns as regions of heterogeneous radiosensitivities have been shown to exist in normal-tissues, such as the lungs [75].

Mechanistic modelling of radiation responses encompasses multiple stages and scales, ranging from the physical/chemical to the cellular and tissue (see Figure 1.13). While the agent- and the equation-based approaches are usually employed to model the later stages/bigger scales, the physical and chemical steps can be simulated using MC methods [76]. Widely employed in the modelling of stochastic processes, this technique can simulate radiation transport and energy deposition in matter. As such, MC methods can be used to replicate the dose delivery in a biological sample and extract spatial information about the dose distribution. TOPAS-nBio [6], for example, can simulate particle transport and dose depositions at the micro and nano scales and, in combination with the ABM platform BDM [4, 5] (see Chapter 2 for an in-depth outline) is used to implement the hybrid model described in Chapter 5. The spatial dose distributions provided by the MC modelling platforms can therefore replace the DVHs as inputs for the downstream layers of mechanistic modelling, though alternatives to that have been proposed in previous studies [77]. From there, estimates of the number of radiation-induced DNA strand breaks can be obtained [78] and used in DNA repair mechanisms simulators [14] to predict individual or population cell survivals. Although

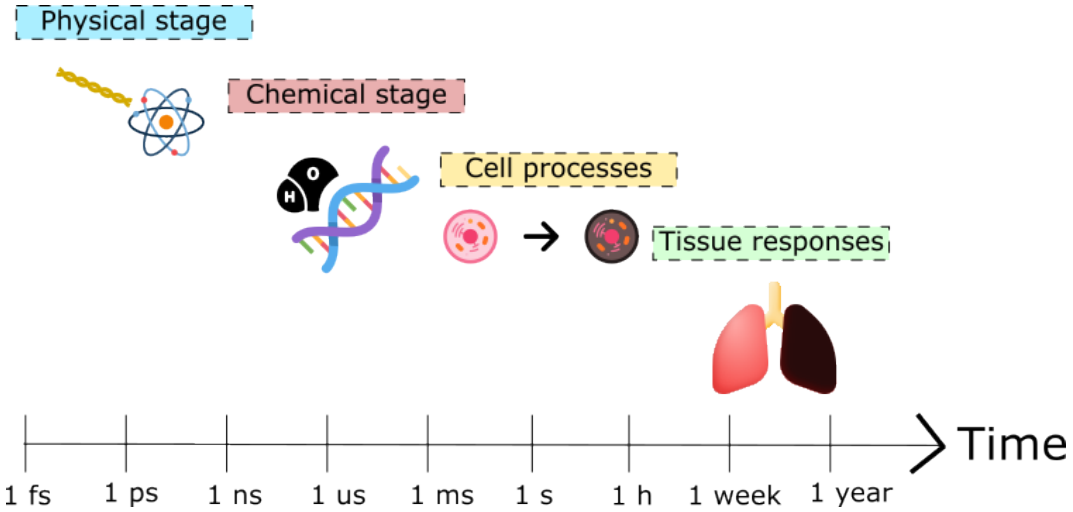

Figure 1.13: Stages of radiation response: in the physical stage, the radiation ionizes atoms and molecules, ROS are generated. DNA damage and fixation takes place in the chemical stage, triggering damage repair mechanisms and eventually cell apoptosis or senescence. If multiple cells are damaged, responses at the tissue level (such as RILI) are observed.

the NTCP estimates of the mechanistic models presented in the previous section are mainly dictated by the cell/FSU survivals, that of the radiation-induced damage is a much broader picture [9]. In the context of RIP and RILF, mechanisms such as the cellular senescence and the bystander-induced damage have proven not-negligible roles in contributing to the severity of the damage [79]. As such, they should be taken into

consideration for a more comprehensive approach in NTCP modelling. Though with different granularity, the AB and the equation-based modelling are examples of relatively modern mechanistic approaches. They can be employed to summarize and incorporate the current radiobiological knowledge into both TCP and NTCP modelling as well as generate/test new hypotheses and investigate the effect of changes in the treatment modalities on the outcome. The AB approach (which, together with its applications, will be the subject of Chapter 2) involves the use of computational agents to simulate processes and systems [3]. Agents, in turn, are independent, potentially heterogeneous entities characterized by a state and equipped with sets of rules that are grouped in behaviours. These make them capable of sensing, reacting to and interacting with the environment and other agents. On the other hand, with the equation-based approach ordinary and partial (if both space and time are described) differential equations are employed to describe the average dynamics of cell populations and, often, the diffusion of substances in the extracellular space [80]. Although the two can be combined by either using an agent representation of the cells and partial differential equations for the substances [81] or ordinary differential equations to describe the behaviours of the cell agents [82], temporal and spatial scales under investigation drive the modelling approach. With reference to the previous examples, an ABM would represent senescence (or, more generally, the cell cycle phase) as a state when modelling at the cell scale, while an equation-based model could use a differential equation to describe the average dynamics of all the senescent cells in the simulation. Equation 1.30 shows the generic form of a partial differential equation that can be used to describe the cell dynamics in an equation-based model [83]

$$\frac{\partial C_i}{\partial t} = \underbrace{\frac{\partial^2 C_i}{\partial \mathbf{X}^2}}_{\text{diffusion}} + \overbrace{\alpha C_i}^{\text{proliferation}} - \underbrace{\mu C_i}_{\text{death}} + \overbrace{f(C_i, S_j)}^{\substack{\text{substance-mediated} \\ \text{production/decay}}} \tag{1.30}$$

Given a cell compartment or population i, the contribution to its concentration C_i at a specific location in space and time can be written in terms of diffusion from/to neighbouring locations (where $\mathbf{X}$ is a position vector), proliferation (with rate α), death (with rate β) and some external factor j (such as oxygen or glucose)-mediated production/decay as a function of both the cell and the substance concentration S_j . As can be seen, once the initial conditions have been set such an equation-based model will give deterministic results. On the contrary, stochasticity can be implemented in an ABM by adding probabilistic rules in the agents' behaviours. Equation-based models allow for much faster simulations as single cells and their mechanical/chemical interactions are not simulated, but the spatial characterization capabilities offered by the ABM approach can be crucial when simulating, for instance, radiation-induced bystander senescence. An agent-based implementation of such a mechanism (modelled in terms of differential equation in [74]) is outlined in Chapter 4. Finally, it's worth noting that NTCP estimates could greatly benefit from incorporating the effect of the immune system or concomitant therapies, both extensively modelled in the mathematical oncology field using the approaches mentioned above [84].

In this thesis, the ABM is combined with equation-based and MC methods to model RILI from the dose-deposition stage to the (partial) tissue response.

2 BioDynaMo

The mechanistic models describing the damage to and the response of the pulmonary tissue outlined in Chapter 3, Chapter 4 and Chapter 5 were developed using BDM [4, 5], an open-source AB modelling framework in the development of which I have taken part. At the time I started working with BDM and its team, AB modelling frameworks were not a novelty, but what made BDM stand out were its performances such as its ability to simulate millions of agents in 3D on a common laptop. I joined discussions and meetings in the past years to help making BDM even more user-friendly and figure out which features could be essential for biological simulations, although its simulation domain has become much broader. In particular, I developed new demos, improved the precision and capabilities of the diffusion module and simplified the installation of BDM on High-Performance Computer (HPC)s, so as to allow larger simulations to be performed. Furthermore, BDM is hosted on GitHub and the approval of new changes not only needs the consensus from the BDM board, but must also satisfy a number of tests aimed at verifying that none of the existing features has been damaged by the new code.

BDM can simulate complex biological systems, involving multi-behaviours agents, interactions between them via chemical and mechanical signalling as well as reaction and diffusion of chemical species. In this chapter an overview of the main AB modelling concepts implemented in BDM will be presented together with a short outline of my contributions.

2.1 Agent-Based Modelling

The AB approach is a form of computational modelling that aims at representing phenomena at multiple spatial and temporal scales by means of agents. Informally, an agent Ag is an autonomous entity that inhabits an environment and is capable of interacting with it and with the other agents (see also the definition in Subsection 1.4.3) through actions in the set Ac and perceptions in the set Per. Let's assume that, at each and every time-step t_i, the environment is in one of the discrete states of the finite set E and define R as the set of all possible sequences (i.e. runs) r of an agent's actions and the corresponding state changes of the environment. If R^E is the subset of R of the runs that end with a state change, then an agent can be formally defined as a function that, given a sequence of actions and state changes, returns the action to perform [85], as follows:

$$Ag : R^E \rightarrow Ac \tag{2.1}$$

A very simple agent is then provided with two functions: see, that allows it to get insights (perceptions) on the environment and $action$ that generates the following action using these perceptions:

$$\begin{aligned} see &: E \rightarrow Per \\ action &: Per \rightarrow Ac \end{aligned} \tag{2.2}$$

With analogies from Subsection 1.4.3, perceptions can set and update the internal state of an agent (used as an input), while the actions are the behaviours the agents' are equipped with and can alter the environment (including the other agents within it).

In BDM each agent is implemented as an independent (C++) object with properties that define its state, such as its shape (spherical or cylindrical), volume, mass, position and user-defined state variables, and behaviours. Each behaviour is a structure composed of actions that are executed sequentially and can have a state as well. When an agent undergoes a division event and a new one is created, behaviours and state variables can be inherited by the daughter. Conversely, an existing agent can be removed from a simulation either by itself or from other agents by invoking the resource manager. Moreover, behaviours can be assigned to the agents at initialization time, or added/removed later. The next paragraph provides examples of agents' behaviours where the features offered by a decentralised approach (such as that of the ABMs) can be appreciated.

The model outlined in Chapter 4 can simulate the onset of RILI in an alveolar segment consisting of 18 alveoli stacked in 3 layers with 6 tangent alveolus each. An alveolus is defined as an hollow sphere with 3 main cell populations arranged concentrically from the internal to the external layer as follows: mesenchymal, epithelial and immune (for further details refer to Chapter 4). Figure 2.1a shows a lateral view of the alveolar segment in ParaView (the default visualizer for BDM) where all the non-epithelial cells have been filtered out. The epithelial cells can be in one of 5 states: type 2 (in green), type 1 (in blue, see Subsection 1.3.1 for the biological background), senescent (in white), damaged (in red) and apoptotic (in black). The healthy type 2 alveolar epithelial cells can be damaged by the radiation and either change their state into the damaged one or become apoptotic. After some time in the damaged state, they transition to senescence and are then capable of damaging the neighbouring healthy cells (bystander senescence). All the aforementioned state changes are examples of cells behaviours, consisting of checks at each time step (for example, for the damaged to senescent transition, the total time spent in the first state) followed by updates in the state variables (which include cell type and characteristics). In Figure 2.1a a feature only mentioned in Chapter 5 is displayed: the damage, at the beginning of the simulation, is limited to the first layer (on the right hand side) and once the simulation is started the bystander damage can take place. Figure 2.1b shows only the damaged cells in the first layer, while Figure 2.1c refers to a later point in time where both intraalveolar and interalveolar bystander damages have progressed to the top of the alveolar segment (third layer). The damaged cells have become senescent (in white) and, by moving on the spherical surface, have damaged healthy alveoli. This happens notwithstanding the presence of macrophages (not shown in the figure) which can clear the senescent cells (see Chapter 4 for further details). In fact, in the first part of the simulation the damage progression speed exceeds that of the senescent clearance. The implementation of the bystander senescence behaviour was suggested by the work of McMahon et al. [74], where a similar dynamics is investigated and modelled analytically. More specifically, healthy type 2 epithelial cells count the number of senescent cells within an "infection radius" corresponding to the alveolar radius and, if this number exceeds a threshold, a time counter (i.e. an internal state variable) is increased. Then, a random number is generated and there's a negative exponential probability (where the time counter is the characterizing parameter) that the healthy cell will become damaged. Again, all this rules are encoded and packed into a single behaviour which is assigned to the healthy cells. Epithelial, mesenchymal and immune cells are all equipped with complex behaviours that regulate their migration patterns around the alveolus (such as the random migration and the neighbourhood-informed migration). To give an idea of the computational burden of the simulations, it's worth noting that, just to compute the migration vectors, operations that involve rotational matrices are evaluated at the behaviours' frequency for each agent.

The environment is defined by a three-dimensional Cartesian mesh (called uniform grid) with regular cubic voxels that span the whole space and size determined by the maximum dimension of the largest object in the simulation. Consequently, the largest object(s) will be the only one(s) that fill a voxel entirely, while other agents might find neighbours in the voxel they occupy. However, even though the volume of a simulation object can span more than one voxel, it belongs to the one where its center of mass is located.

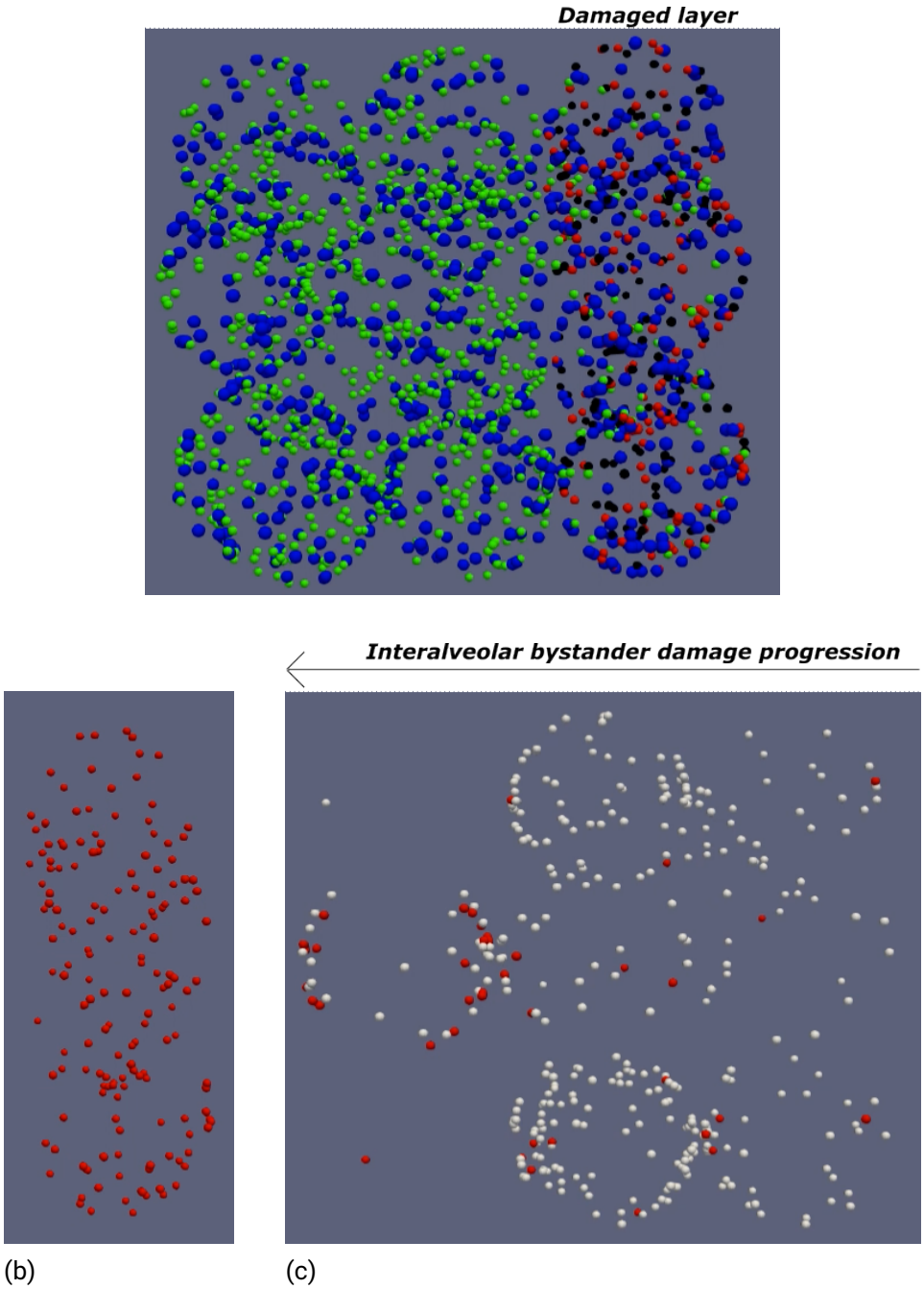

(a)

(b)

(c)

Figure 2.1: Progression of the bystander senescence in a partially damaged alveolar segment. **a** lateral view of the alveolar segment showing only the epithelial cells. Damage is limited to the first layer. **b** non-damaged cells filtered out, the first layer is shown at the beginning of the simulation. **c** progression of the bystander senescence: damaged cells have transitioned to the senescent state and have damaged via bystander interactions the neighbouring alveoli further up the alveolar segment.

For mechanical interactions purposes, a micro-environment of an agent is defined which includes its voxel and the surrounding 26 and defines the volume that the agent can interact with. When the forces acting on an agent under consideration j are computed, only the simulation objects i in its microenvironment are taken into account. The resulting displacement depends on the sum of all the interactions, where each force has both a repulsive and an attractive component and is given by

$$F_{ij} = k \cdot \delta - \gamma \cdot \sqrt{r \cdot \delta} \tag{2.3}$$

In Equation 2.3 k and γ are given constants, δ is the overlap between i and j and r is a combined measure of the spherical/cylindrical radii

$$r = \frac{r_1 r_2}{r_1 + r_2} \tag{2.4}$$

Computing the resulting force acting on an agent, the (potential) following translation and finally applying the displacement are examples of commands packed into an operation, triggered by the scheduler at each time step. In BDM both standalone- and agent-operations exist that are executed only once or for each agent, respectively, with a predefined frequency. Agents' behaviours are another example of agent-operation whose default frequency can be reduced (or, in another terms, not run at each time step) to simulate a larger temporal scale. This can be useful to reduce the computational burden in the presence of processes that take place at lower temporal scales, such as the diffusion of substances.

2.2 Diffusion

In addition to the operation that computes the mechanical forces and those user-defined (for instance to export parameters, as done in the models presented in Chapter 3, Chapter 4 and Chapter 5), the "continuum" operation is in charge of running each continuum model defined within the simulation (such as scalar and vector fields). Among them, the diffusion of extracellular substances is a default continuum model that is triggered at each time-step. Similarly to the uniform grid mentioned in the previous section for the mechanical forces, to handle the diffusion the simulation space is split into cubic voxels with identical size that together constitute the diffusion grid. Multiple diffusion grids can be initialized, one for each substance, and for each of them the user specifies the diffusion constant D, the decay parameter λ, the resolution r and an optional binding coefficient for multi-substance interactions. The resolution corresponds to the number of voxels per dimension (or, in other words, a resolution of 10 means that the diffusion grid is made up of 1000 voxels in total) and different substances can have different resolutions. However, the resolution, together with the total size of the simulation space (which is shared between the diffusion grids), dictates the size of each voxel Δx which, together with the time-step length Δt and the diffusion constant D, must satisfy the Courant-Friedrichs-Lewy (CFL) stability condition (see Chapter 3). Space and time are thus discretized to solve Partial Differential Equation (PDE)s in the form

$$\frac{\partial C}{\partial t} - D_C \nabla^2 C = S - \lambda C \tag{2.5}$$

using the Forward Euler in Time and Central in Space method (FTCS) scheme, where S is a source/sink term that represents the interactions between the agents and the diffusion grid. In fact, agents can access the concentration of a substance in the voxel they are located and update its value. Moreover, at initialization time, it is possible to specify the initial concentration distribution of each substance using either a constant value or a user-defined function.

Since in RILI substance-mediated depletion has been observed (such as the Matrix MetalloProteinases (MMP)-mediated depletion of the ECM, see Chapter 3 for further details), I've implemented the mechanism

in the solution scheme of the diffusion PDEs. As previously mentioned, when a new diffusion grid is created before the start of a simulation, a set of parameters that characterise its dynamics must be provided. Among them, when initializing substances that are depleted users can provide optional parameters that indicate the name of the depleting substance and the binding coefficient that dictates the strength of the interaction. In those cases Equation 2.5 thus reads as follows

$$\frac{\partial C_i}{\partial t} - D_{C_i}\nabla^2 C_i = S - \lambda C_i - \mu C_i C_j \tag{2.6}$$

where C_i is the concentration of the depleted substance, C_j is the concentration of the depleting substance and μ is the binding coefficient. For the resolution of the PDE, the product μC_j is regarded as an additional decay constant (such as λ) and when a binding coefficient is provided in the definition of a substance, then a "depletion" Euler grid object is created instead of the "standard" Euler grid. Put simply, when C_i is computed for the next time step $t + \Delta t$, the standard formula is used (see the next section) and then the factor μC_j is subtracted from the concentration computed. As a side note, a substance can be depleted by multiple substances with different binding coefficients.

2.2.1 Boundary conditions

When I joined the BDM team, two Boundary Condition (BC)s for the diffusion grids (i.e. shared between all of them) were available: the closed and open boundaries. When using the first one, the substances could not leave the simulation space, while the second allowed for leakage in the open space. Since none of the formulations was defined in formal terms, I've implemented the Dirichlet and Neumann BCs to allow more control over the behaviours of the substances at the boundaries.

Dirichlet BCs specify the values of the concentration C on the boundaries throughout the whole simulation and, if the requested concentration is 0, these are called homogeneous [86]. For example, they may be used to simulate a system that forces the external layer of the simulation space to maintain a fixed concentration or temperature (see Figure 2.2a). Regarding the actual code implementation, the Dirichlet BCs are easily introduced as, for each time step and concentration computation, the index of the current voxel is checked. If the voxel lies within the inner region of the simulation space the standard formula is used, otherwise the voxel belongs to the boundaries and therefore the actual BCs are evaluated. This means that, for each voxel at the boundaries, a user-defined function is invoked that sets the concentration of that voxel for the next time-step. Such function $f(\mathbf{x}, t)$ might depend on the position of the voxel and on the current time step and the evaluation of the concentration narrows down to

$$C(\mathbf{x}, t) = f(\mathbf{x}, t) \tag{2.7}$$

Conversely, the Neumann BCs specify the value of the derivative of C with respect to a normal unitary vector and the implementation in the Forward Euler in Time and Central in Space method (FTCS) is not straightforward. They might be used, for example, to simulate inward/outward fluxes or a net zero flux (as is done in the simulations outlined in Chapter 4 and Chapter 5. See Figure 2.2b). Similarly to the algorithm for the Dirichlet BCs, for the inner voxels the concentration is computed using the standard formula, while an updated version is required for the voxels on the boundaries. In what follows the derivation of the equation in 1D is provided, together with an outline of the Finite Difference (FD) methods used in BDM to compute the temporal evolution of the concentration of the substances.

The 1D diffusion equation (with no decay and source terms) reads

$$\frac{\partial C}{\partial t} = D\frac{\partial C^2}{\partial x^2} \tag{2.8}$$

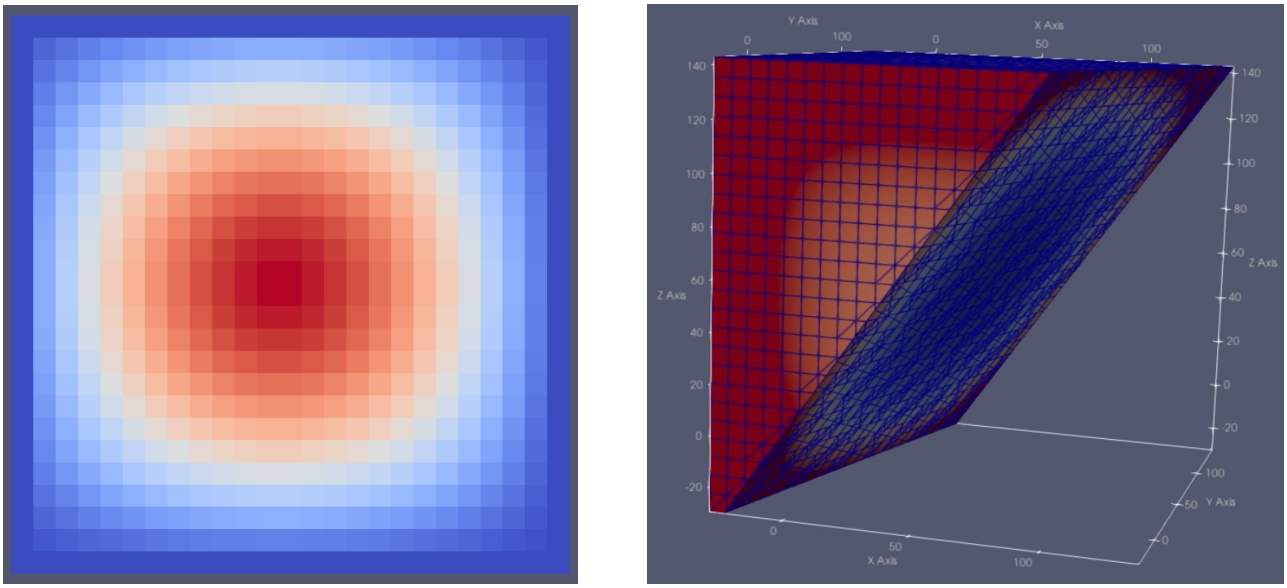

(a) (b)

Figure 2.2: Diffusion grids with BCs in place. **a** section of the cubic simulation space with homogeneous Dirichlet BCs. A substance with $C > 0$ diffuses isotropically from the center towards the boundaries. There, the BCs ensure that the concentration is $C = 0$ (in blue). **b** cubic diffusion space sectioned with positive Neumann BCs that simulate an inward flux from the boundaries (in red) towards the center.

where $C = C(x, t)$ and D is the diffusion coefficient. To solve the equation, a domain must be specified as well as BCs. Here we will take into account Neumann BCs on a 1D domain given by $x_{left} \leq x \leq x_{right}$. The Neumann BCs specify the value of the derivative at the boundary(s) of the domain, namely:

$$\frac{\partial C}{\partial \mathbf{n}} = f(\mathbf{x}), \forall \mathbf{x} \in \partial\Omega \tag{2.9}$$

where $\mathbf{n}$ is an exterior (thus pointing outwards) normal vector to the boundary $\partial\Omega$ and $f(\mathbf{x})$ is a given scalar function.

Finite Difference (FD) methods involve the use of FD expressions to approximate derivatives. These expressions can be used (for example) by computers to numerically solve differential equations. The three main types of FD methods are: forward difference, backward difference and central difference. The solution to the Equation 2.8 proposed here involves the forward and central expressions only, therefore the backward is not presented. The forward difference approximation for the first derivative is given by

$$\frac{f(x + \Delta x) - f(x)}{\Delta x} = f'(x) \tag{2.10}$$

The central difference approximation for the first derivative is given by

$$\frac{f(x + \Delta x) - f(x - \Delta x)}{2\Delta x} = f'(x) \tag{2.11}$$

The central difference approximation for the second derivative is given by

$$\frac{f(x + \Delta x) - 2f(x) + f(x - \Delta x)}{\Delta x^2} = f''(x) \tag{2.12}$$

Equation 2.8 can be rewritten using Equation 2.10 for the time derivative and Equation 2.12 for the space derivative, leading to the following

$$\frac{C(x,t+\Delta t)-C(x,t)}{\Delta t}=D\frac{C(x+\Delta x,t)-2C(x,t)+C(x-\Delta x,t)}{\Delta x^2} \tag{2.13}$$

Which can be rearranged to give

$$C(x,t+\Delta t)=C(x,t)+\frac{D\Delta t}{\Delta x^2}\left[C(x+\Delta x,t)-2C(x,t)+C(x-\Delta x,t)\right] \tag{2.14}$$

Equation 2.9 can be approximated using equation Equation 2.11

$$\frac{C(x+\Delta x)-C(x-\Delta x)}{2\Delta x}=K(\mathbf{x}) \tag{2.15}$$

For the sake of simplicity, in what follows we will consider $K(\mathbf{x})$ constant, i.e. $K(\mathbf{x})=K$. Both the time and the space domain must be discretized to solve Equation 2.8 numerically. The discretization of the time domain is straightforward: given a discrete time step Δt, the total time τ is divided into T equally spaced intervals with $t_k=k*\Delta t$, for $k=0,1,...,T$. Analogously, the one dimensional spatial range (a grid for higher dimensions) $0\leq x\leq L$ is divided into N intervals, called *cells*, by N+1 evenly spaced points, called *walls*. The spacing between two consecutive walls or cells is Δx and the cells, located at the midway point between two walls, are identified by $x_i=i*\Delta x$, for $i=0,1,...,N-1$. To distinguish the location of the cells from that of the walls, the latter are denoted by fractional indices of the form $x_{i+\frac{1}{2}}$, so that $i+\frac{1}{2}$ refers to the wall located between the cells *i* and *i+1*. A spatial domain discretized with 10 cells and 11 walls can be seen in Figure 2.3 .

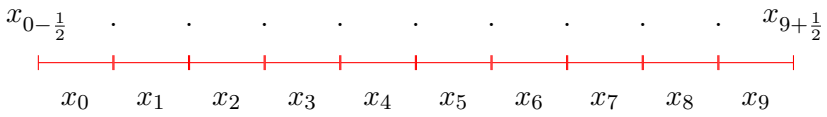

Figure 2.3: 1D spatial domain discretized with 10 cells

Using the discretization scheme presented above, Equation 2.14 can be rewritten for the cells' positions as

$$C_i^{k+1}=C_i^k+\frac{D\Delta t}{\Delta x^2}\left[C_{i+1}^k-2C_i^k+C_{i-1}^k\right] \tag{2.16}$$

and the same can be done for Equation 2.15, the formulations of which, at the walls' positions, are

$$\left(\frac{dC}{dx}\right)_{i+\frac{1}{2}}=\frac{C_{i+1}-C_i}{\Delta x}=K(\mathbf{x})\longleftrightarrow C_{i+1}=C_i+K(\mathbf{x})\Delta x \tag{2.17}$$

$$-\left(\frac{dC}{dx}\right)_{i-\frac{1}{2}}=-\frac{C_i-C_{i-1}}{\Delta x}=K(\mathbf{x})\longleftrightarrow C_{i-1}=C_i+K(\mathbf{x})\Delta x \tag{2.18}$$

where the negative sign for the left wall results from the opposite directions of the gradient (e_x) and the exterior normal vector to the boundary ($-e_x$). Equation 2.16 thus provides a formula that can be iterated to compute the concentration at each time-step t_k for $1\leq i\leq N-2$, given that the initial values C_i^0 are known for each cell location. The Neumann BCs given by Equation 2.17 and Equation 2.18 can be used

to compute the concentration at the cells located on the boundaries of the spatial domain, i.e. for $i = 0$ and $i = N - 1$. In fact, Equation 2.16 at the boundaries involves the terms C_{-1} and C_N which are located outside the spatial domain. Equation 2.16 at the boundaries can then be written as:

$$i = 0 \rightarrow C_0^{k+1} = C_0^k + \frac{D\Delta t}{\Delta x^2}\left[C_1^k - C_0^k + K(\mathbf{x})\Delta x\right] \tag{2.19}$$

$$i = N - 1 \rightarrow C_{N-1}^{k+1} = C_{N-1}^k + \frac{D\Delta t}{\Delta x^2}\left[-C_{N-1}^k + C_{N-2}^k + K(\mathbf{x})\Delta x\right] \tag{2.20}$$

By solving Equation 2.16 for the cells located at $1 \leq i \leq N - 2$ and Equation 2.19 and Equation 2.19 for $i = 0$ and $i = N - 1$ respectively, it is therefore possible to compute the concentration at each cell location for $t > 0$.

2.2.2 Additional parameters checks

In addition to the existing CFL condition on the diffusion grid parameters, I've contributed to the implementation of two additional checks. The first one is a stability criterion that extends the CFL condition by taking into account the decay parameter λ. In particular, it was derived by applying the von Neumann stability analysis (cfr. [86], section 2.10.3.) on Equation 2.5. This leads to the following condition that ensures that the approximation error will not grow exponentially:

$$\left(\lambda + \frac{12 \cdot D}{\Delta x^2}\right)\Delta t \leq 2 \tag{2.21}$$

For $\lambda = 0$ Equation 2.21 becomes the CFL.

The second check ensures that, given a set of parameters $\{\lambda, D, \Delta x, \Delta t\}$, the concentration of the corresponding substance will never drop below 0 in any voxel. Assuming $C(x, t) \geq 0$, by requiring that $C(x, t + 1) \geq 0$ the following must be satisfied

$$1 - \left(\lambda + \frac{6 \cdot D}{\Delta x^2}\right)\Delta t \geq 0 \tag{2.22}$$

Again, for $\lambda = 0$ Equation 2.22 reduces to the CFL.

2.3 Examples

In this section further contributions to the BDM project are presented, together with the relative features implemented and/or experimental results obtained.

2.3.1 Monolayer growth

I've developed a BDM demo that simulates the growth of a 2D monolayer of tumour cells (in terms of total number of cells and diameter of the tissue) over a 1 month period. The results, shown in Figure 2.4 in blue, exhibit a good agreement with the experimental data presented in [87]. More specifically, the simulation starts with a predefined pool of cells placed on the xy plane that go through a cycle consisting of 4 phases: G1, S, G2, M. Cells start in the G1 phase and at each time step the transition to next phase is achieved if a randomly generated number is smaller than a certain transition probability. This probability, in turn, is given by the ratio between the age of the cell and the maximum possible duration of the state, which

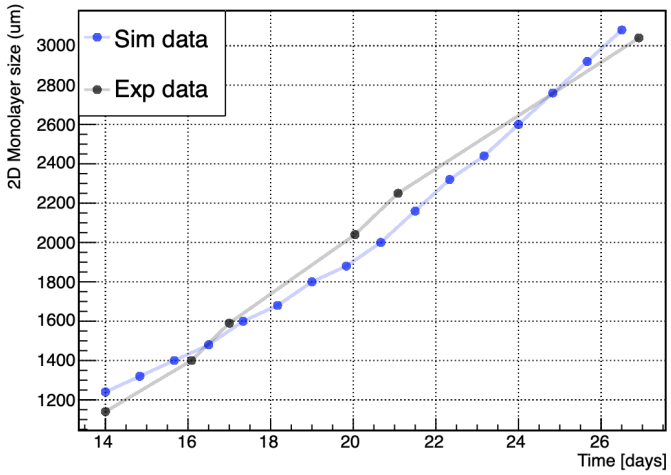

Figure 2.4: Size of the diameter of a 2D monolayer of cancer cells as a function of time. Blue dots shows data from a simulation performed with a model implemented in BDM, while the black dots represent the results reported in [87]. Overall a good agreement was observed at all time points.

ensures a certain degree of heterogeneity within the cell population. Moreover, at each time step each cell grows a little, but the cell volume can't exceed a certain threshold. When a cell reaches the mitosis phase (M), if it's big enough and if the number of neighbours falls below a predefined threshold as well (representing the contact-induced quiescence phenomenon), the cell can divide into two identical cells and the daughter inherits all the internal state parameters from the mother. Finally, cells can't move freely, but in Equation 2.3, which defines the interaction force between two agents, the attraction and repulsion parameters were tuned so as to accelerate the separation between the mother and daughter cells.

2.3.2 HPC installation and testing

To further increase its performances (i.e. reduce the total computational time) and/or run multiple simulations in parallel, BDM can be installed on an HPC. In fact, the presence of many cores on a node can speed up the calculation by orders of magnitude as the load is shared among them and, since each node can run a separate simulation, the effect of different sets of parameters on the simulation's outcome can be investigated. For the models presented in Chapter 3, Chapter 4 and Chapter 5, the simulations were run on multiple nodes of a cluster not only to test different parameter values, but also to speed up the results collection and improve the statistical significance. BDM uses OpenMP [88] to parallelize the agents' operations on multiple cores, but at the time I joined the BDM team the installation procedure on HPCs was still ambiguous. Therefore, I contributed to the implementation of the definition file that installs BDM in a Singularity container [89]. This ensures that the installation can be performed on multiple operating systems and doesn't require the user to deal with the package manager of the cluster or have root privileges (via the *–fakeroot* option).

Once installed on an HPC, tests were performed to quantify the improvements in terms of performance. In particular, a modified version of the *Tumour concept* demo (see the BDM webpage for more information) with 10^6 initial cells and unitary division probability once reached the required volume, was run. Different numbers of steps were simulated with increasing cores and the total simulation time measured. Figure 2.5 shows the results for 500, 650 and 750 simulation steps run on 4, 8, 16 and 32 cores. Not unexpectedly, the computational time decreases as the number of cores increases, but the gain in time reduction can be

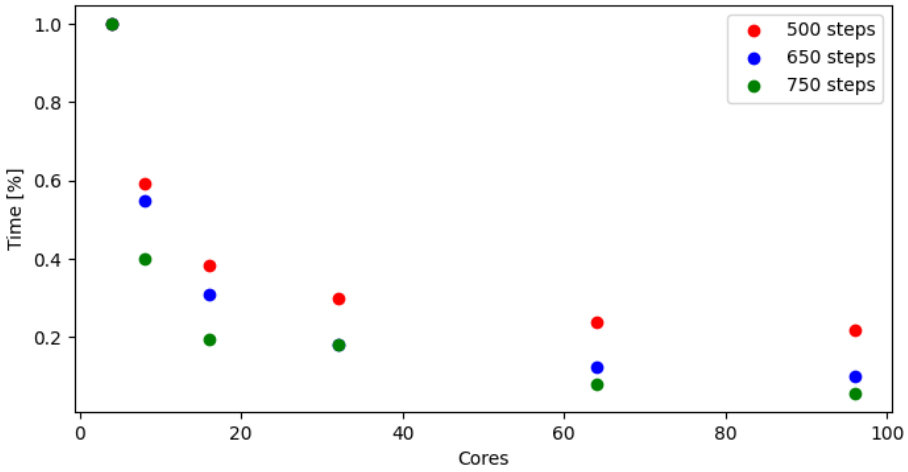

Figure 2.5: Fractional simulation time of the *Tumour concept* demo as a function of the number of cores for different numbers of steps. The simulation time with 4 cores is used as a reference (i.e. fractional simulation time = 100%). The total simulation time decreases exponentially with an increase in the number of cores, but there are diminishing gains as the upper end of the set is approached.

appreciated more at the lower end of the cores set. However, it is clear that there are huge benefits from running simulations on multiple cores and the greatest are observed for longer running simulations.

2.3.3 Lung substructures

Given that previous modelling efforts in modelling RILI mechanistically didn't employ agents, I've modelled substructures of the lungs at multiple scales to explore the relative advantages and disadvantages. At first a model of alveolus was developed that represents several cell types (see Figure 2.6a), including: AEC1, AEC2, M1, M2, endothelial cells, pericytes, mast cells, plasma cells, lymphocytes and fibroblasts [28]. The alveolus was implemented as an hollow sphere, with the AEC1 being the biggest cells and the endothelial cells lining the alveolus to form four capillaries that converge at the north and south "poles". Since BDM supports only spherical and cylindrical shapes, all the cells were assumed to be spheres and the average volume, as reported in the literature, was converted to that of a sphere. Using the Fibonacci lattice algorithm, epithelial and interstitial cells were distributed evenly on the alveolus surface and the position of those that fell into the alveolus opening drawn randomly. Moreover, cells were assigned behaviours that allowed them to check their position and "escape" the alveolar ring (i.e. the opening) in case they entered it.

To replicate a full alveolar segment, the number of alveoli was at first estimated based on the actual size of a human segment [25] and then 4 layers of 6 alveoli each were stacked and centred on an internal axis to obtain a cylindrical shape (see Figure 2.6b). Finally, to build a (partial) pulmonary acinus, a regular dichotomous tree was constructed for the first 3-4 generations by evenly distributing the axes of the alveolar segments. Then, for the further generations, polar and azimuthal angles were generated randomly and an algorithm was used to check that the axes didn't collide. The alveoli that fell into the junctions between different alveolar segments were then removed to simulate a continuous structure (see Figure 2.6c and Figure 2.6d).

Although realistic, the elevated number of agents of the model described above and the repeated checks for the position of the cells made the simulations heavily time-consuming. To reduce the simulation time, only the main cell types were maintained (inspired by [90]) and the alveoli were reshaped to resemble

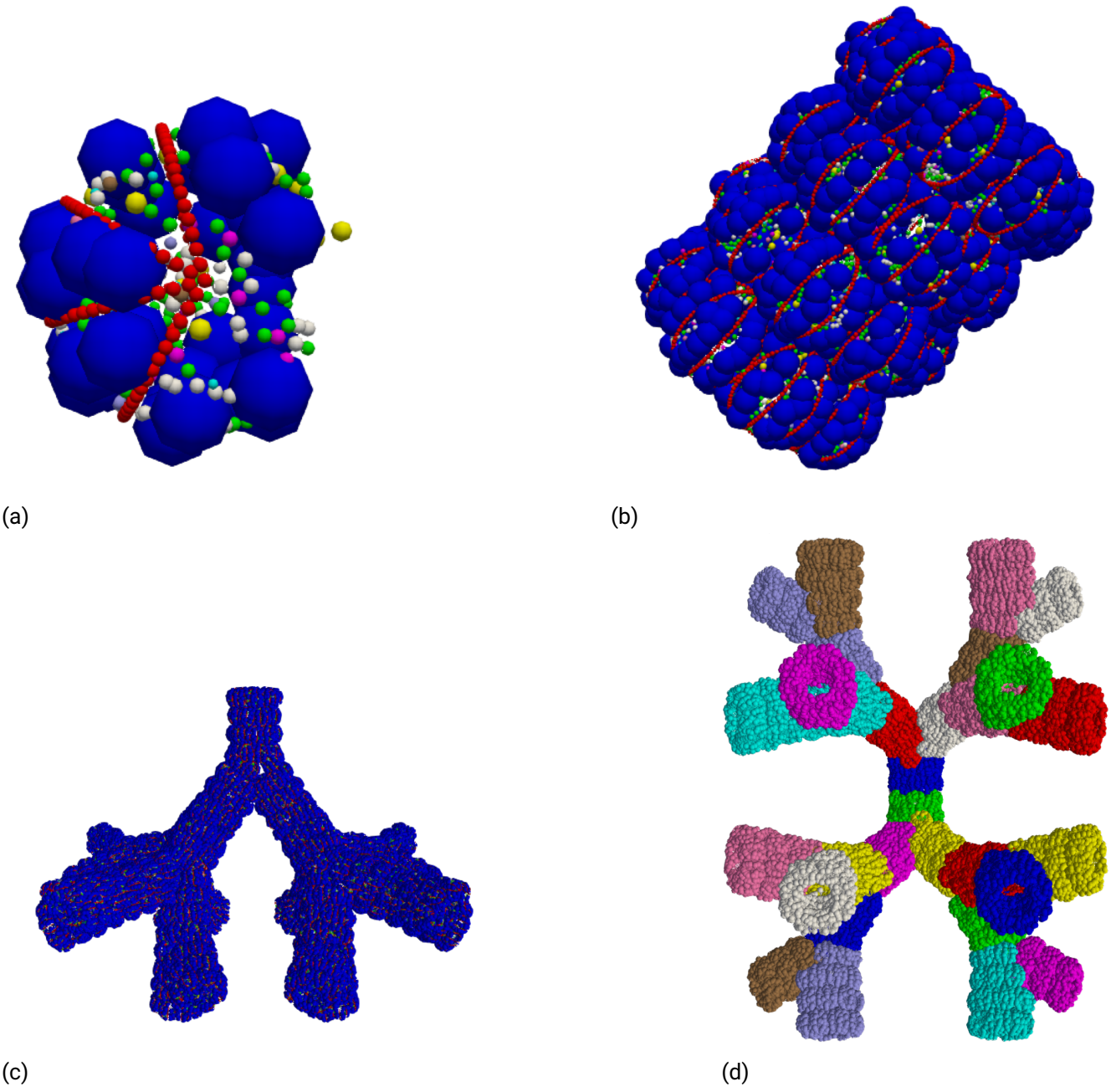

Figure 2.6: Substructures of a pulmonary acinus modelled with different granularities. **a** Hollow sphere that represents an alveolus with AEC1 in blue, AEC2 in green, endothelial cells in red, fibroblasts in white, M2 in yellow, M1 in violet, pericytes in brown, mast cells in light blue. **b** alveolar segment with 4 layers of 6 alveoli each stacked on top of each other. **c** 5-generations pulmonary acinus seen from the front. Cell colors are the same as in figure **a**. **d** 5-generations pulmonary acinus seen from the bottom. Different alveolar segments have different colors and all the cells that belong to an alveolar segment are coloured in the same way.

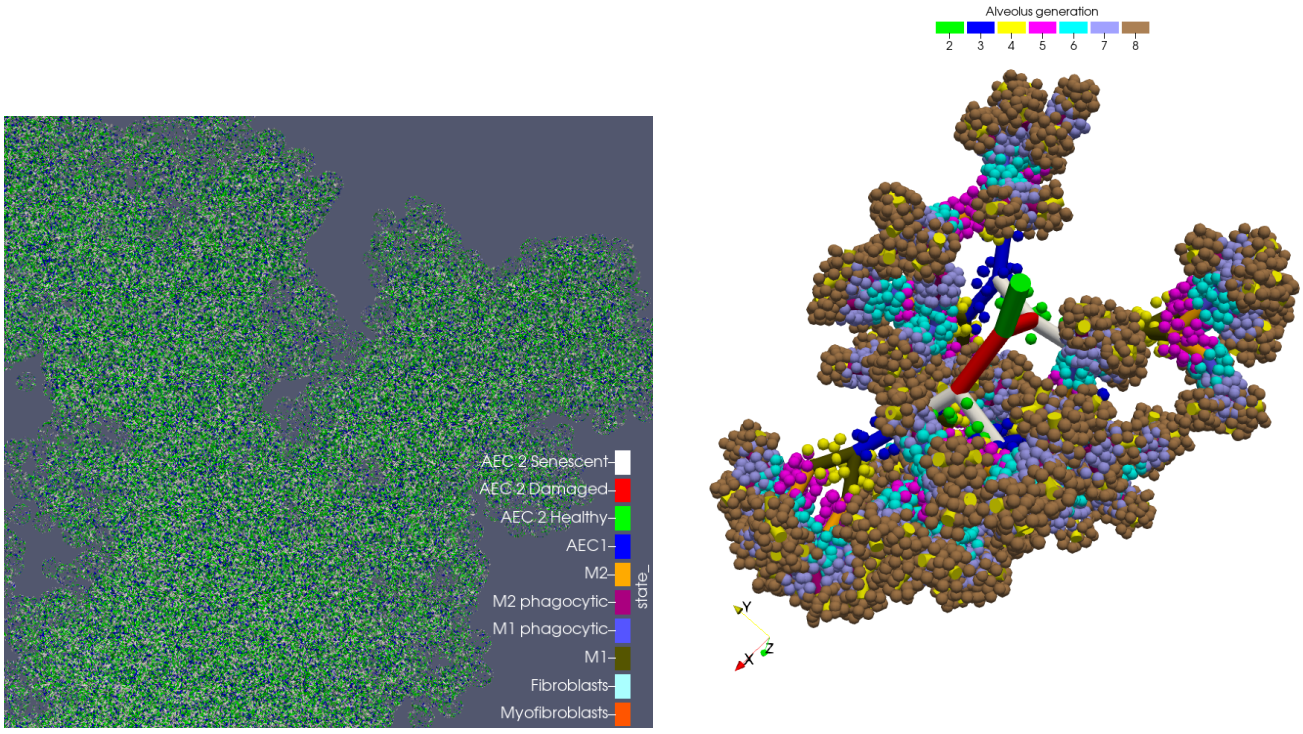

(a) (b)

Figure 2.7: Partial model of pulmonary acinus at different agent scales. **a** 9-generations acinus where single cells are modelled as agents. Different colors are used to discriminate the cell types, however, the smaller structures (i.e. alveoli and alveolar segments) are hardly distinguishable.. **b** 9-generations acinus where full alveoli are modelled as agents. Different colors are used for each generation and the alveolar segments are represented by cylinders.

spheres, thus avoiding the overstep into the alveolar ring (though the cells still had to be constrained on a spherical surface). The results of this reimplementation can be seen in Figure 2.7a, however this model wasn't used to simulate the onset of RILI as the time required for a simulation was still prohibitive. In fact, due to the nature of RILI, its onset and resolution can be observed only after months or even years and although the simulation time-steps can be made larger, they must comply with the constraints imposed by the algorithm that solves the diffusion of the extracellular substances. To further reduce the simulation time, two strategies were employed. The first one involved using fewer, larger agents to simulate multiple cells at once. This approach led to the structure shown in Figure 2.7b where each agent represents one alveolus and was further scaled up to implement the model described in Chapter 3 which successfully replicated the onset of the IPF. The second strategy was more trivial and involved limiting the simulated portion to an alveolar segment, where each agent represented a cell. The models outlined in Chapter 4 and Chapter 5 were developed following this second strategy and could simulate the onset of RILF as well as common ECM patterns and severity indexes.

3 A 3D Agent-Based Model of Lung Fibrosis

This chapter was published in 2022 in Symmetry Vol. 14, Issue 1:90, Nicolò Cogno et al. "A 3D Agent-Based Model of Lung Fibrosis", Copyright MDPI (2022)[82].

3.1 Introduction

Lung fibrosis is characterized by the progressive aberrant accumulation of ECM accompanied by the depletion of healthy epithelial tissue, which eventually result in poor gas exchange, increased lung stiffness, and death [91]. Despite having an idiopathic origin in most of the cases (referred to as IPF), RILF is commonly observed in cancer patients treated with thoracic ionizing radiation, representing the major dose-limiting factor [32]. Regardless of the damage source, similar pathways have been identified in the pathophysiology of both IPF and RILF [92].

Fibrosis is thought to originate from the lung parenchyma, where more than 300 million alveoli, functional units responsible for gas exchange, reside [27, 91, 93]. The alveolar epithelium, which includes alveolar epithelial cells of types I (AEC1, the actual gas exchanger) and II (AEC2, stem cells responsible for the preservation of the epithelium) [94], can aberrantly react to injury and trigger inflammatory responses [95, 96, 97, 98] (see Figure 3.1). When damaged AEC2 are unable to repair properly, they can either undergo apoptosis or activate and adopt a senescent phenotype [99]. If the latter occurs, AEC2 cells lose their progenitor capability (thus leading to AEC1 depletion) and release proinflammatory and profibrotic factors through the acquisition of a Senescence-Associated Secretory Phenotype (SASP) [92, 98]. The deterioration of the epithelial membrane, along with the release of cytokines and chemokines, such as the TNFα, and the MCP1 or CCL2, activates the Th1 immune response and allows M0 (which later differentiate into classically activated or type I macrophages, M1) to breach into the alveolus [92, 93]. M1 macrophages can then differentiate into their alternatively activated form, M2, and represent an additional source of TNFα, which is able to reverse the transition [100]. M2 macrophages, in turn, secrete a plethora of mediators (including the active form of the transforming growth factor beta, TGFβ_a [101, 102], PDGF [103], IL13 [104], MMP [105], and Tissue Inhibitors of MetalloProteinases (TIMP) [105] which affect several cellular species. Among these, fibroblasts are mesenchymal cells that secrete inactive TGFβ (TGFβ_i) [106], the ECM [107], and are able to differentiate into myofibroblasts. The ECM is degraded by the MMP, whose effect is inhibited by TIMP [108]. TGFβ (which can be activated by damaged AEC2 [109] and whose secretion by M2 is amplified by IL13 [110]), in its active form, increases the proliferation of fibroblasts [111], stimulates their differentiation into myofibroblasts [112], and damages healthy AEC2 cells [113]. IL13 further enhances the proliferation of fibroblasts [114] together with the basic fibroblast growth factor (bFGF or Fibroblasts Growth Factor 2 (FGF2)) secreted by the AEC2 [115, 116], while PDGF triggers the differentiation of the fibroblasts [117]. Myofibroblasts deposit additional ECM [118] (a mechanism intensified by TGFβ [119]) and have a pivotal role in the remodeling process that takes place in the alveolar region. The population of mesenchymal cells can be further expanded through the EMT, a process by which activated AEC2 differentiate into fibroblasts and/or myofibroblasts [120]. The overall effect is an increase in the number of ECM-secreting cells that leads to the abnormal accumulation of the ECM.

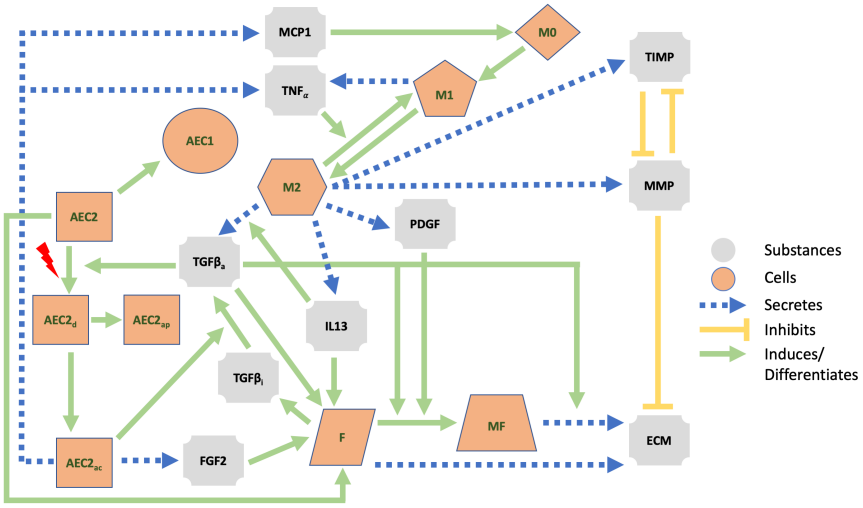

Figure 3.1: Schematic representation of the main cells, extracellular mediators, and pathways in lung fibrosis. AEC1 = alveolar epithelial cells type 1, AEC2 = alveolar epithelial cells type 2, AEC2$_d$ = damaged AEC2, AEC2$_{ap}$ = apoptotic AEC2, AEC2$_{ac}$ = activated AEC2, F = fibroblast, MF = myofibroblast, M1 = type 1 macrophage, M2 = type 2 macrophage, M0 = monocyte, MMP = matrix metalloproteinases, ECM = extracellular matrix, TIMP = tissue inhibitors of metalloproteinases, IL13 = interleukin 13, TGFβ_i = inactive form of the transforming growth factor beta, TGFβ_a = active form of the transforming growth factor beta, FGF2 = basic fibroblast growth factor, TNFα = tumor necrosis factor, PDGF = platelet-derived growth factor, MCP1 = monocyte chemoattractant protein 1.

Although the chain of events presented in Figure 3.1 above highlights a causal link between the lung damage and the fibrosis onset, it only unfolds the backbone of a disease that is far from being fully understood [92]. The motivation to elucidate this link stems from multiple factors, including the lack of animal models that thoroughly reflect the human complexity and the time needed for the fibrosis to fully develop [121]. In light of these considerations, in-silico or computational models represent invaluable tools towards a better understanding of complex biological (among others) systems [122] and hold the potential for several clinical applications. In fact, at present, high-performance computers allow us to simulate experiments at a fast pace, with moderate costs and without the need for laboratories. In-silico modeling is nowadays applied in clinically relevant research, whose applications include, but are not limited to, drug design, clinical decision making, treatment optimization, and personalized medicine [123]. Computational models lay the foundations for personalized medicine and drug development: the parameters of a validated disease model can be calibrated to reflect patients-specific conditions and the simulation outputs employed to elaborate tailored therapies. Moreover, computational models are powerful tools for addressing a various number of diseases on multiple scales, ranging from the subcellular to the global, as recently shown for COVID-19 [124, 125]. The use of the aforementioned models in biomedical frameworks has a well-defined pattern: the theoretical prototype is originally built on the basis of available in-vitro and/or in-vivo data and implemented in-silico; the model is then used to simulate existing data and altered until a good match between in-silico and laboratory data is observed; finally, in-silico models are used to predict new data for clinical studies [122].

Equation-based modeling and AB modeling are common and powerful approaches when it comes to implementing computational models, with the choice being mainly affected by the spatiotemporal scales of the simulated phenomenon [126]. On the one hand, EBMs assume homogeneous populations and consist of sets of ordinary differential equations or PDEs that are evaluated at every time step and location [127,

128]. On the other hand, heterogeneities among entities of the same species (i.e., randomness) in the simulation space can be recapitulated by ABMs in which interacting individual agents behave according to a set of rules [129, 130]. While EBMs are better suited for fast time scales and small spatial scales (e.g., to represent diffusing molecules), ABMs can properly reproduce larger systems (such as cells and tissues) at slower time scales, with a special emphasis on agent–agent and agent–environment interactions [126]. Finally, hybrid ABMs combine the methodologies described above by making extensive use of synchronization techniques and data feeding from one system to the other so that broader scenarios can be reproduced [130].

In this paper, we outline the implementation of a hybrid ABM of lung fibrosis by means of an innovative software simulation platform (namely, BDM [4]) and show that it has the potential to reproduce results from other studies. Key mechanisms extracted from reviewed literature are encoded into simple sets of rules and used to define the behaviors of the agents. Moreover, we include chemical mediators that diffuse through the extracellular space and allow for long- and short-range inter-agent interactions. We began by calibrating the parameters of our model in order to reproduce the homeostatic conditions of the distal lungs. When the homeostasis was established, we introduced damage sources of various intensities and stored the model's readouts as the symmetry of the system was broken.

The goal of the present study is the development of a solid and up-to-date model to be later on employed as a research tool and further expanded with additional layers to suit specific use-cases. Both EBMs and ABMs of lung fibrosis can already be found in the literature [90, 131, 132, 133, 134], but while the use of the mean field approach in the former limits their ability to recapitulate the heterogeneous nature of the biological systems, the latter are typically implemented on small 2D spatial scales, the simulated time frames are short, and both the number of cells and geometrical structures do not reflect the features of the lungs. Our model seeks to overcome the major limitations of the previous models.

3.2 Materials and Methods

In the following sections, the implementation of our hybrid multi-agent-based model is detailed. More specifically, we (i) present the geometry and features of the simulation environment motivated by its morphological counterpart, (ii) describe how the diffusion and interaction of substances are implemented, and (iii) outline how agent behaviors are derived from previous works and the related parameters tuned.

3.2.1 Framework and Implementation

The simulation model is implemented with BDM 1.0 [4], an open-source software simulation platform that allows users to build and run multi-scale simulations. The elements of the simulation, i.e., the simulation space, the entities inside it, and the interaction rules, are encoded in the C++ language and simulations can be carried out on common laptops, even with limited computational resources, or cluster nodes. The source code for the model can be found in the supplementary material, (available online) while installation instructions for BDM are available at https://biodynamo.org/docs/userguide/.

In BDM, discrete time is marked by simulation time steps (whose length can be defined by the user) and agents are instances of the Agent class. Variability between agents from different populations can be emphasized by defining custom attributes, which altogether define the state of an agent, whereas agent–agent and agent–environment interaction rules are wrapped in behaviors. Behaviors, in turn, are executed for each agent at every time step when certain conditions are satisfied. In addition, changes in the state of each agent, i.e., in one or more of its attributes, can be automatically stored during the simulation and made available for a subsequent graphical visualization of the simulation. Finally, standalone

operations, executed once per time step (see [4] for more details), can be defined and used, for example, to gather data throughout the simulation (see Section Initial Conditions and Input/Output System).

Python 3.9 (more specifically the libraries SciPy, MatPlotLib, NumPy and ROOT) is used to gather and plot the outputs of different simulations. Our simulations are performed on

- a MacBook Pro 2018 running macOS Big Sur on a 2.3 GHz Quad-Core Intel Core i5 processor with 8 GB RAM;
- a compute node of the Lichtenberg HPC system running CentOS 8.2 on 2x 2.3 GHz Intel Cascade-Lake AP 48-cores processor (96 total cores) with 384 GB RAM.

3.2.2 Building the Simulation Space

Human and mammary airways can be split in two subsystems: the proximal, ending with the terminal bronchioles, where conducting airways move air inside and outside the body, and the distal/peripheral, where the actual oxygen exchange takes place in the acinar airways [27]. Within the latter, further morphological structures can be distinguished: some 30,000 acini branch by irregular dichotomy for 8-9 generations, terminating with alveolar sacs. The non-terminal segments that make up the branches of an acinus are the alveolar ducts (256 per acinus on average [27]), onto which clusters of alveoli with common openings towards the lumen are localized (the same holds for alveolar sacs). Previous work has reported an average length of 730 μm and an average outer diameter of 600-699 μm for the alveolar ducts, which can be seen as hollow cylinders [26, 135]. Given that the most common shape of a human alveolus is a three-quarter sphere [136] with an average diameter of 260 μm [25], we estimate that each duct should serve between 18 and 24 alveoli, arranged in 3 rings of 6-8 alveoli each [137] (a slightly larger value can be found from the ratio between the total number of alveoli and the total number of segments).

Our model aims to mechanistically replicate the onset of lung fibrosis on a scale bigger than the cellular one as the disease affects large portions of the pulmonary tissue. For this reason, we build our simulation space as a dichotomic tree structure (see Figure 3.2) that mimics a part of an acinus and choose the alveolar segments as agents. The tree expands along the z-axis in the 3D simulation space and each segment has the same length (that is, the average segment length from [26, 135]), expressed in μm. Since the average segment length and outer diameter are similar, we replace the segments with the corresponding inscribed spheres (spherical-shaped agents are included in the BDM platform). The algorithm that we implement to build the structure is the following:

1. Given the number of generations Ngen, define the number of segments as $Nseg = 2^{Ngen} - 1$, the average segment length as avgSegLength, and the vector containing the coordinates of all the agents as Coords.
2. Set the coordinates of the agent 0 (the first alveolar segment) to 0., 0., 0. (i.e., the center of the simulation space), its unique index to 0, its origin to $0., 0., -avgSegLength/2$, and its end to $0., 0., avgSegLength/2$. Add $0., 0., 0.$ to Coords.
3. Loop $(Nseg/2)$ times. At each step (starting from 1):
   a) Define the index of the father agent (i.e., the one from which branch 1 and branch 2 stem) as $father = [(step + 1)/2] - 1$.
   b) Project the coordinates of the father agent along its axis by avgSegLength.
   c) For each of the two new branches:
      i. Generate random polar and azimuthal angles θ and ϕ.

ii. Rotate the projected father agent by θ and ϕ, keeping its origin fixed.

iii. If the branch doesn't overlap with the other agents already in the tree add its coordinates to Coords.

iv. If the branch overlaps with any of the other agents already in the tree, go back to step i.

4. Write Coords to a file, so that it can be used for multiple simulations.

Specifically, our tree branches at random angles for 7 generations and includes a total of 127 alveolar ducts, which fit inside a simulation volume of 10,000 μm^3 (or 1 cm^3). The ranges that we choose for θ and ϕ are [20°, 160°] and [45°, 89°], respectively, and are the smallest that allow the tree to fully develop without overlaps. Since the alveolar ducts could be further decomposed into multiple agents (i.e., the alveoli) made up of subagents (i.e., the cells, [3]), the agents in our model can be seen as meta-agents.

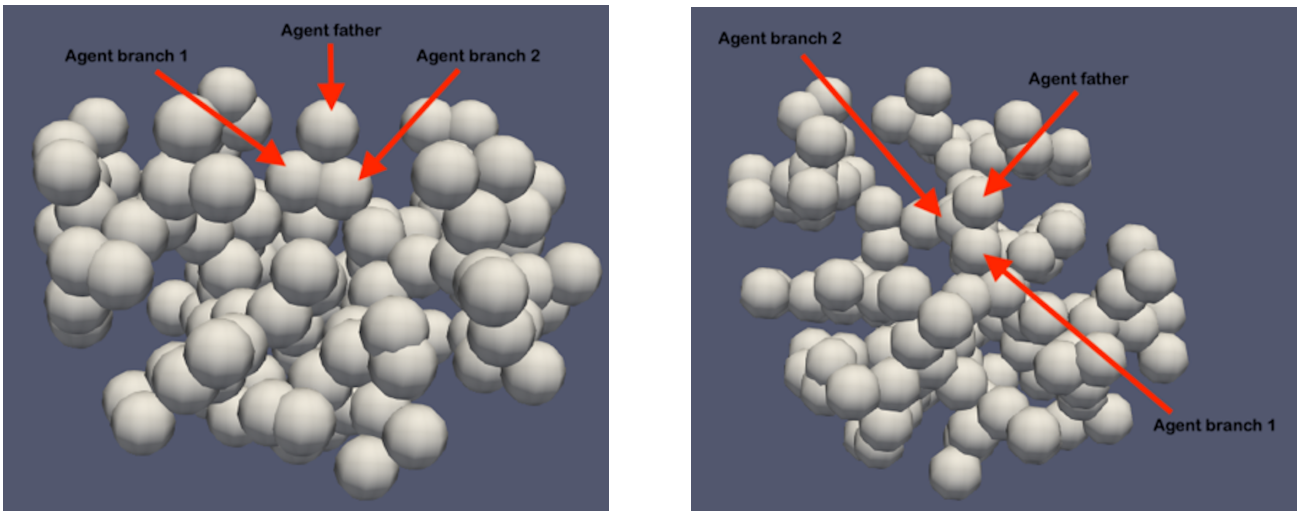

Figure 3.2: Graphical representation of the simulation space as a dichotomic tree structure.

3.2.3 Extracellular Mediators

As mentioned above, we implement an hybrid ABM, which is a model that encompasses both entities, called agents and fluids, that can diffuse through the simulation volume. More specifically, we include in our simulations extracellular mediators that affect the agents' environment. Mediators follow the general diffusion equation

$$\frac{\partial C}{\partial t} - D_C \nabla^2 C = S - \mu C \tag{3.1}$$

where C is the concentration of the mediator, D_C is the isotropic diffusion coefficient, S is the source term (the cell secretion in our model), and μ is the decay coefficient. The given coefficients (see Table 3.1) are specified at the beginning of a simulation for each substance together with the initial concentrations, which we set to be flat across the whole simulation space.

Extracellular Substance	Initial Concentration (gcm^{-3})	Diffusion Coefficient (cm^2day^{-1})	Decay Coefficient (day^{-1})	Source
$TGF\beta_a$	$2.51 * 10^{-12}$	$4.32 * 10^{-2}$	$3.33 * 10^2$	[90]
$TGF\beta_i$	$2.51 * 10^{-12}$	$4.32 * 10^{-2}$	$3.33 * 10^2$	Estimated
$PDGF$	$3.50 * 10^{-9}$	$8.64 * 10^{-2}$	3.84	[90]
$FGF2$	0	$5.62 * 10^{-2}$	1.66	[138, 139]
$TIMP$	$5.74 * 10^{-10}$	$4.32 * 10^{-2}$	21.60	[90]
ECM	$3.26 * 10^{-3}$	0	0.37	[90]
MMP	$3.66 * 10^{-8}$	$4.32 * 10^{-2}$	4.32	[90]
TNF_α	$2.50 * 10^{-8}$	$1.29 * 10^{-2}$	55.45	[90]
$IL13$	$3.20 * 10^{-8}$	$1.08 * 10^{-2}$	12.47	[90]
$MCP1$	0	$1.73 * 10^{-1}$	1.73	[90]

Table 3.1: Model parameters for the extracellular substances.

In order to solve the partial differential equations (PDEs) in the form of Equation 3.1 for each of the substances, BDM implements multiple resolution schemes (we adopt the central difference method). To this end, both space and time are discretized: the diffusion grids (defined for each substance) split the simulation volume into evenly-spaced 3D boxes (whose size $\Delta x = \Delta y = \Delta z$ can be defined by the user), while a constant global Δt defines the size of a time step. At each time step, the discretized concentration of each substance is updated within each box.

In our model, we set the resolution (that is, the number of diffusion grid boxes along each dimension) to 10 for each substance so that (i) the CFL stability condition $\left(\frac{D_C * \Delta t}{\Delta x^2}\right) < \frac{1}{6}$ for the PDE solver is fulfilled (a necessary condition for the explicit version of the central finite difference method) and (ii) each box (with volume 1000 μm^3) can enclose an agent (with diameter 700 μm). Moreover, we select the scheme "DiffuseWithOpenEdge" to make BDM run our simulations with open boundaries.

In order to support interactions among different substances (which are needed by our model as it simulates ECM and TIMP depletion by MMP and MMP depletion by TIMP), we extended BDM by implementing this feature in the diffusion source code. Specifically, we edited

- the function used to define substances at the beginning of a simulation so that both the depleting substance and the binding coefficient can be specified;
- the function that implements the central difference method by embedding the local depletion (i.e., $\mu_{AB} * A_i$, where μ_{AB} is the binding coefficient and A_i is the concentration of the depleting substance in the i-th box where the calculation is performed) into the decay term.

To assess whether our custom BDM is able to properly simulate interactions among different substances, we develop a basic model involving MMP and TIMP. The mediators are secreted by stationary agents located at the center of the diffusion grid boxes, with one agent per box. Our model is then used to simulate the diffusion and interaction of the substances for a time frame of 2 days with different Δt values: 1 s, 0.1 s, 0.01 s, 0.001 s. As expected, the results presented in Figure 3.3 show a negative correlation between the size of the time step and the accuracy of the model. In fact, smaller Δt values lead to greater agreement between the steady-state reached by the model and the theoretical results (represented by the dashed red line).

However, as Δt decreases, the time needed to simulate the same time frame increases linearly. Therefore, we select 0.1 s (the default value provided by BDM is 1 s) as the best compromise between model accuracy

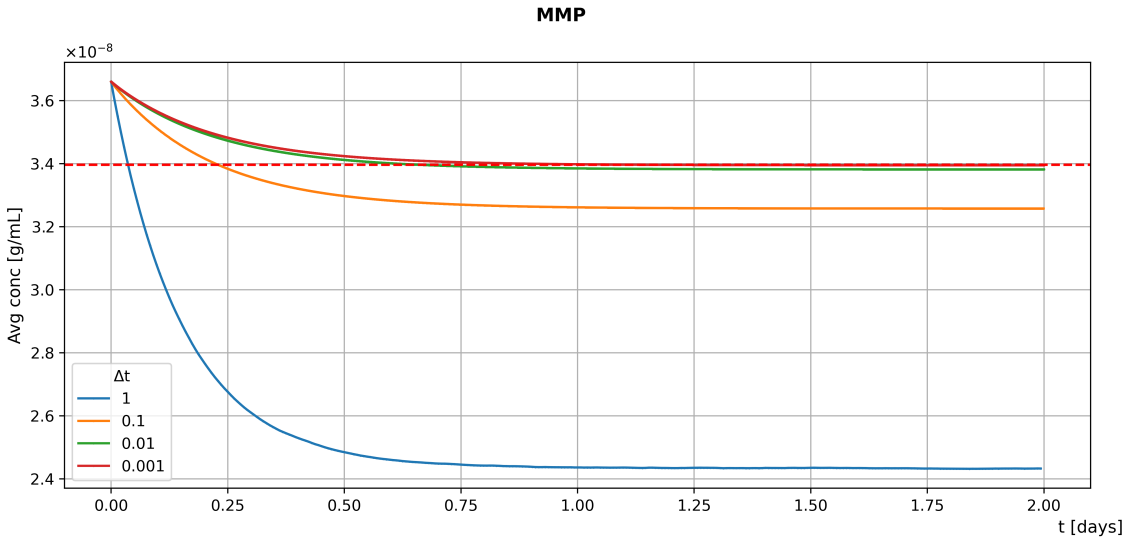

(a)

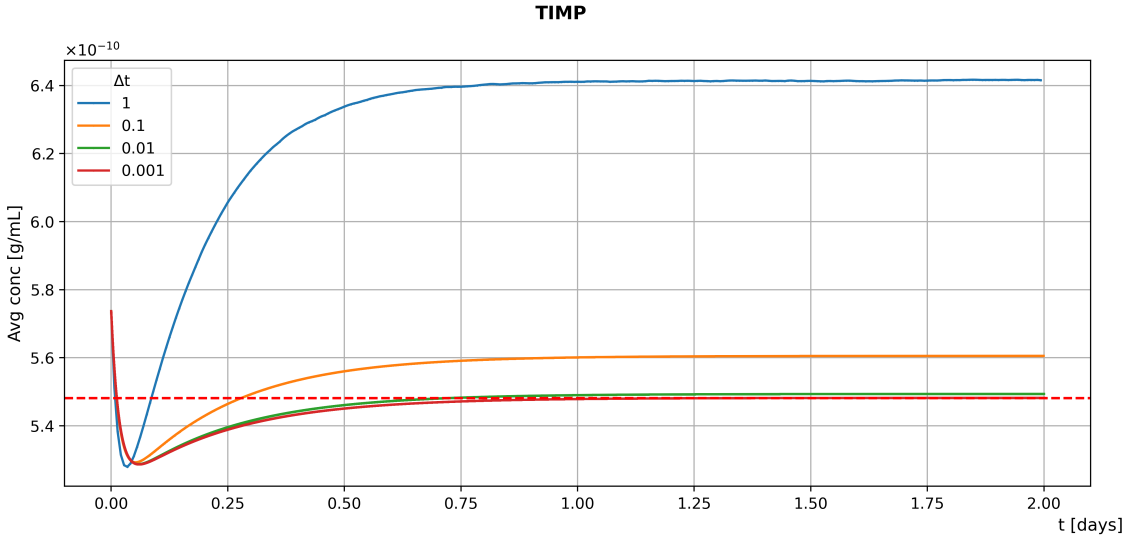

(b)

Figure 3.3: Time evolution of the average MMP (**a**) and TIMP (**b**) concentrations in a stationary simplified model simulation with different Δt values.

and computational costs (note that the CFL stability condition $\left(\frac{D_C * \Delta t}{\Delta x^2}\right) < \frac{1}{6}$ for the PDE solver is still fulfilled after this choice). Further evidence on the robustness of our model to changes in Δt is provided in Figure S2 (available online).

3.2.4 Hybrid Multi-Agent-Based Model

To build our hybrid multi-agent-based model, we follow the bottom-up approach: we gather observations found in the literature, then use this data to define the properties and behaviors on the microscale (i.e., on the agent level) and finally observe where these lead to on the macroscale. At any given time t, an agent is

fully defined by the set of all its attributes that together determine its state. To specify the attributes of our agents and the interfaces to read and write them, we implement the class alveolarDuct, which extends the BDM Cell class. Each agent in our simulations is therefore an instance of alveolarDuct, whose data members store the initial and current number of cells for each cell type (see Table 3.2). Essential data members such as the cell position and diameter, as well as the methods to access them, are inherited from the base class Cell.

Cell Type	Cell Number per Alveolus[1]	Source
AEC1	41	[29]
AEC2	69	[29]
M1	13	[29]
M2	12	[29]
Fibroblasts	24	[29, 90]
Myofibroblasts	36[2]	[29, 90]
M0[3]	65	[29, 90]

[1] Initial cell number. [2] Based on the ratio given in [90], which takes into account an initial inflammation, we assume that 60% of the fibroblasts differentiate into myofibroblasts. [3] Maximum number of M0 available per alveolus, based on the ratio 5 M0:1 M1 from [90].

Table 3.2: Model cell types and number.

As soon as a new agent is added to the simulation, it gets assigned its behaviors. Computationally, this involves defining a list of sequential operations (examples can be found in Figure 1B from [4]), encapsulating them in a named structure, and, finally, adding the structure to a vector of behaviors that is attached to the agent. After a time step Δt (the same used for the update of the concentration of the extracellular substances), each agent runs through all its behaviors; that is, it performs all the actions listed in each of them. Since all the agents in our simulations are alveolar ducts, they run the same behaviors at each time step. Nevertheless, since many behaviors depend on the local concentration of the mediators and different agents perceive different microenvironments, they evolve and act differently throughout the simulation.

The behaviors implemented in our model can be categorized, as shown in Table 3.3. As mentioned above, the behaviors share the same template but differ in the core section, which defines the actions that the agents must perform. Their implementation within the ABM is heavily influenced by the model of IPF, published in [90] as a mathematical formulation, where many aspects of the IPF are provided. Unless otherwise stated, concentration-dependent rates follow Michaelis-Menten kinetics

$$S = \frac{\lambda * C}{C + K} \tag{3.2}$$

where λ represents the maximum value of the rate, C is the local concentration of an extracellular substance, and K is the concentration at which the rate reaches half of its maximum value. Agents can directly measure the local concentration (i.e., that of the diffusion box they are located in) of a substance at each time step and use this quantity to determine the variable rates of their behaviors. These measurements must be repeated at every time step as the extracellular environment evolves throughout the simulation.

Secretion		Proliferation	Differentiation	Activation	Apoptosis
AEC2 TNFaSecretion	M2 PDGFSecretion	F Proliferate	AEC21 Differentiation	AEC2 Activation	Apoptosis
AEC2 MCP1Secretion	M2 MMPSecretion	F Addition	F MF Differentiation		
AEC2 FGF2Secretion	M2 TIMPSecretion	AEC2 Proliferate	M01 Differentiation		
AEC2 TGFbSecretion	M2 TGFbSecretion		M12 Differentiation		
F TGFbSecretion	M2 IL13Secretion		M21 Differentiation		
F ECMSecretion	M1 TNFaSecretion				
MF ECMSecretion					

Table 3.3: Agents behaviors.

The following subsections briefly outline each behavior.

Secretion Behaviors

Agents change the local concentration of a substance according to specific secretion rates. Given that the rates are known only for the initial number of cells, agents scale the rates with the current number of cells at every time step. Since each agent only keeps track of its own current number of cells (a property of the alveolar duct agents), the principle of local information exchange is not violated.

- PDGF/MMP/TIMP/IL13 secretion by M2, TNFα secretion by M1, TNFα/MCP1 secretion by active AEC2 (whose activation process is described in Section Activation Behaviors)), and TGFβ secretion by fibroblasts have similar templates and depend on constant secretion rates.

- Both FGF2 secretion by active AEC2 and ECM secretion by myofibroblasts are increased by TGFβ. Similarly, TGFβ secretion by M2 is increased by IL13. In our model, these dynamic rates are expressed by

$$\lambda_{FGF2,AEC2} * \left(1 + \lambda_{FGF2,TGF\beta} * \frac{TGF\beta}{TGF\beta + K_{FGF2,TGF\beta}}\right) \tag{3.3}$$

$$\lambda_{ECM,myof} * \left(1 + \lambda_{ECM,TGF\beta} * \frac{TGF\beta}{TGF\beta + K_{ECM,TGF\beta}}\right) \tag{3.4}$$

$$\lambda_{TGF\beta,M2} * \left(1 + \lambda_{TGF\beta,IL13} * \frac{IL13}{IL13 + K_{TGB\beta,IL13}}\right) \tag{3.5}$$

- As in [90], the constant secretion rate of ECM by fibroblasts is multiplied by the factor in Equation 3.6, where ECM$_{sat}$ is the value at which the ECM saturates. When ECM>ECM$_{sat}$, secretion is stopped.

$$\left(1 - \frac{ECM}{ECM_{sat}}\right) \tag{3.6}$$

- Activated AEC2 cells transform the latent form of TGFβ secreted by fibroblasts into its active form. Within the same time step, they reduce the local concentration of TGFβ_i and increase that of TGFβ_a by the same amount given by Equation 3.7, where K_{AEC2} is a saturation constant.

$$TGF\beta_i * \left(\frac{AEC2_{active}}{AEC2_{active} + K_{AEC2}} \right) \tag{3.7}$$

Proliferation Behaviors

Since the number of agents is constant throughout a simulation, proliferation behaviors simply translate into updates in the number of cells, which are stored as attributes by the alveolar ducts. The proliferation behaviors thus make use of the internal methods of the agents as an interface to update the number of cells of a specific type.

- The proliferation of AEC2 is governed by a constant rate that allows for the survival of both the AEC2 and AEC1 populations. To do so, at every time step, the AEC2 population increases by a constant fraction.
- Proliferation of fibroblasts depends on the number of healthy AEC2 in homeostasis and is further increased by damage-associated mediators such as FGF2, TGFβ_a, and IL13. To uncouple the two mechanisms, we implement (i) the F_addition behavior by which the number of fibroblasts is incremented according to a fixed fraction of AEC2 (represented by the parameter $\lambda_{F,AEC2}$), and (ii) the F_proliferate that computes the fraction of newborn fibroblasts using the rate in Equation 3.8.

$$\frac{FGF2}{FGF2 + K_{fibr,FGF2}} * \left(\frac{IL13}{IL13 + K_{fibr,IL13}} + \frac{TGF\beta}{TGF\beta + K_{fibr,TGF\beta}} \right) \tag{3.8}$$

Differentiation Behaviors

Differentiation behaviors act by updating cell numbers in pairs.

1. In AEC21_Differentiation and M12_Differentiation, the phenotypes of constant fractions of AEC2 and M1 are changed so that the AEC1 and M2 populations in homeostasis can survive.
2. M0 cells act as a reservoir for M1 cells (hence indirectly for M2 cells) both in homeostasis and in inflammatory conditions. In our model, we implement two different mechanisms within the same behavior to ensure that a minimum number of M1 is always maintained. We define a constant rate λ_{M01} for the M0 to M1 differentiation and use this value only if the concentration of MCP1 is too low to provide the M1 cells' baseline. As the inflammation develops and the MCP1 can sustain the growth of M1 cells, we use the differentiation rate in Equation 3.9, where the last factor ensures that M1 cells never exceed M0 cells, as described in [90]. As stated before, the principle of local information exchange is not violated since each alveolar duct agent records only its number of M0 and M1 cells. Therefore, λ_{M01} may assume different values for different agents.

$$\lambda_{M01} = \frac{MCP1}{MCP1 + K_{MCP1,M01}} * (M0 - M1) \tag{3.9}$$

3. Fibroblast to myofibroblast and M2 to M1 differentiation are implemented in F_MF_Differentiation and M21_Differentiation. Since both are triggered by extracellular mediators, their templates are similar, and the rates that describe the transitions are outlined in the following equations

(3.10)

$$\lambda_{M1,M2} * \left(\frac{TNF\alpha}{TNF\alpha + K_{M21,TNF\alpha}} \right) \tag{3.11}$$

Activation Behaviors

In our model, damage is a special case of the differentiation behavior in which cells, instead of changing their type, change their state. In our model, AEC2 can be found in three different states: healthy, damaged, and activated. At the beginning of a simulation, a fraction of healthy AEC2 in each alveolar duct (specified by the parameter hitProbability) can be damaged. By running the AEC2_Activation behavior, agents can then update the state of a constant fraction (i.e., rates are fixed) of damaged cells and turn them into the activated state. We assume that activated and damaged AEC2 cannot be repaired.

Apoptosis Behaviors

To simulate apoptosis, cells are removed from the simulations using the same AB methods used for the proliferation, i.e., cell line-specific rates control the fraction of cells that is updated at each time step. With the exception of AEC2 (whose apoptotic rate is increased by TGFβ and oxidative stress δ, as outlined in Equation 3.12), all the rates are static.

$$d_{AEC2} = d_{AEC2,0} * \left(1 + \frac{TGF\beta_a}{TGF\beta_a + K_{AEC2,TGF\beta}} + \delta \right) \tag{3.12}$$

At every time step, AEC2 apoptotic rates are updated for each agent according to the local TGFβ concentration.

3.2.5 Initial Conditions and Input/Output System

This section provides an overview of the data imported into (including the model parameters and their sources) and exported from the simulations and details how the I/O operations are implemented within the model.

Our model relies on two input sources: the list of cell positions and the parameter list. As detailed in Section Building the Simulation Space, the former is provided by an algorithm that outputs different structures for every run as the branching angles are randomly drawn. To avoid running the building algorithm prior to each simulation, we save its output on a ROOT [140] file (a high-performance open-source data analysis framework developed at CERN) and feed multiple simulations with the same input. When the simulation platform is started, a function reads the list of cell positions and adds as many agents to the simulation setting as their ”Position” attributes to one element of the list. The latter input source is a parameter list that consists of default parameters and custom parameters. Values for the default parameters are provided by BDM and can be overwritten by the user. We overwrite a few of them, as mentioned in the previous sections: the simulation time step, the size of the simulation volume, the resolution scheme for the PDEs, and the boundary conditions for the diffusion. Moreover, a list of almost 90 custom parameters (see the supplementary material, available online) includes behavior-specific parameters (such as rates), substance-specific parameters (as shown in Section Extracellular Mediators), and simulation-specific parameters (such as the names of input files and the number of simulation steps). When a new simulation instance is created, the file with the parameters list can be given as an argument so that its content becomes available to set up the simulation environment and the agents' behaviors and attributes. As a side note, single parameter values can be specified using the inline-config option to further

overwrite those in the parameters list. We take advantage of this feature to run multiple parallel simulations on the cluster nodes with different parameter sets.

The output of a simulation consists of: the time-evolution of the number of cells in each agent and the average concentration of the extracellular substances and (optionally) visualization data. To gather these data, we use the standalone operations provided by BDM and set a frequency for the measurements. Whenever the frequency is matched by the elapsed time steps, the following occurs

1. An operation runs through all the agents, collects the number of cells for each cell type, and stores the information in a vector.

2. Another operation exploits the agents as probes: it gathers their position, uses these positions to get the local concentration of all the substances, computes the average concentration for each substance, and finally stores the information in a vector (note that there is no measurement within the diffusion grid boxes where agents are not localized).

At the end of the simulation, each measurement is assigned its timestamp, and the vectors are exported to ROOT files [140]. If the Visualization parameter is set to true, the selected agent attributes are exported too, and their time-evolution can be visualized using ParaView.

Moreover, we implement a simple Python script to collect exported files from multiple simulations and generate graphical outputs showing the average of the measurements. The outputs are then used in a feedback system as inputs for the following simulation: in fact, the proliferation and differentiation rates, as well as the secretion rates, are adjusted according to the number of cells and the average concentrations, respectively. These parameters are then tuned until a stationary state is reached under homeostatic conditions (i.e., the concentration of the substances and the number of cells do not drift from the initial values listed in Table 3.1 and Table 3.2, respectively). For FGF2 (which is secreted by AEC2 in inflammatory conditions and is not explicitly included in the model from [90]), we assume that the necessary concentration to stimulate the same effect on fibroblasts proliferation as in [90] is that for which the following condition holds:

$$\frac{FGF2}{FGF2 + K_{fibr,FGF2}} = \frac{E}{K_E + E} \tag{3.13}$$

where the right-hand side of the equation comes from the mathematical model of IPF described in [90]; E represents the concentration of damaged AEC2, while K_E is the AEC2 saturation constant.

3.2.6 Sensitivity Analysis

Performing a full parameter sensitivity analysis is beyond the scope of this work due to its prohibitive time requirements. This notwithstanding, we selected five key parameters and performed a relative sensitivity analysis to assess how they affect the simulation outcomes. For each pair of altered parameter p and characteristic (or readout) c, the following indicators are computed:

$$D_{c,p,a} = \frac{C_{p,a} - C_{control}}{C_{control}} * 100 \tag{3.14}$$

$$S_{c,p} = \frac{\Delta_{c,p,a}}{\Delta_a} = \frac{D_{c,p,+a} - D_{c,p,-a}}{\Delta_a} \tag{3.15}$$

where a is the amount of change in the parameter p ($\pm 10\%$ in this work), and C is the measured outcome. $D_{c,p,a}$ is the index percentage of change and shows the relative change of the characteristic c with respect to the control value (i.e., in unaltered conditions) that occurs when the parameter p is altered by an amount a. The second indicator, $S_{c,p}$, represents the sensitivity and quantifies the effect of the variation

±a in the parameter p on the characteristic c. Finally, the results are presented using a relative sensitivity map, where each row represents the relative sensitivities $r_{c,p}$ of a selected simulation readout to all the altered parameters (shown in the column headers). $r_{c,p}$ is computed as the ratio between each $S_{c,p}$ and the maximum absolute value of $S_{c,p}$ for that particular characteristic.

3.3 Results

3.3.1 Homeostasis

Our model is run without damaged cells to simulate ideal homeostasis during a time frame of 30 days. The initial conditions are listed in Table S1 (available online), and the results, shown in Figure 3.4, are expressed in terms of the average concentration of the cell-hosting diffusion grid and the average number of cells per alveolus. The positive amount of myofibroblasts is used to simulate initial light inflammatory conditions.

To assess the ability of our model to reproduce homeostatic conditions in which both the average local concentration of the extracellular mediators and the average number of cells reach the steady-state, we measure their relative change between day 5 and day 30, as follows

$$\Delta_m = \left(\frac{m(t+1) - m(t)}{m(t)} \right) * 100, m\epsilon\{conc, cell\} \tag{3.16}$$

and provide Δm for the two quantities in Figure S1 (available online).

We assume that both the cell number and the concentration of the extracellular mediators are already in steady-state at day 5 since they never exceed the 10% bands and their relative changes stay below 0.025% throughout the whole simulated time frame. However, a slight decrease in the number of myofibroblasts, coupled with an increase in the number of fibroblasts, shows a tendency of the model to shift towards fully homeostatic conditions

3.3.2 Inflammation

To simulate the onset of fibrosis, our model is run with an initial amount of damaged AEC2 cells and replicates a time frame of 300 days. Different runs are performed for different initial (average) fractions $\overline{f}$ of damaged AEC2, where $\overline{f}\ \epsilon\{6.25, 10, 20, 30, 40, 50, 60, 70, 80, 90\}$% and the damage is heterogeneously spread over the simulation space (i.e., the fraction of damaged AEC2 cells within each alveolar duct is drawn from a normal distribution with average $\overline{f}$ and σ = 1%). More specifically, the value $\overline{f}$ = 6.25% allows us to compare the results from our simulations against those shown in [90] since the study reports the steady-state ratio $\frac{ActivatedAEC}{InitialAEC} = 0.0625$. Rather than a continuous damage (as proposed in [90]), healthy AEC2 cells in our model are damaged only at the beginning of the simulation and the active AEC2 cells cannot undergo apoptosis (i.e., they are never removed from the simulation). We make this assumption as our model aims to simulate the onset of lung fibrosis regardless of the cause for the damage to the AEC2 cells.

The initial conditions are listed in Table S1 (available online), and the results, shown in Figure 3.5, are expressed in Section Homeostasis. Though with slower dynamics, our results (for $\overline{f}$ = 6.25%) are in agreement with those provided by Hao et al. [90]. ECM accumulation, a surrogate of lung fibrosis severity, shows incremental rises for $\overline{f} \leq$ 40%. On the other hand, for $\overline{f}$ > 40%, the healthy AEC2 cells are unable to support the mesenchymal population, whose drop leads to a progressive decline in the final ECM concentration. This notwithstanding, we show that the loss of AEC2 progenitor cells is reflected by a sharp

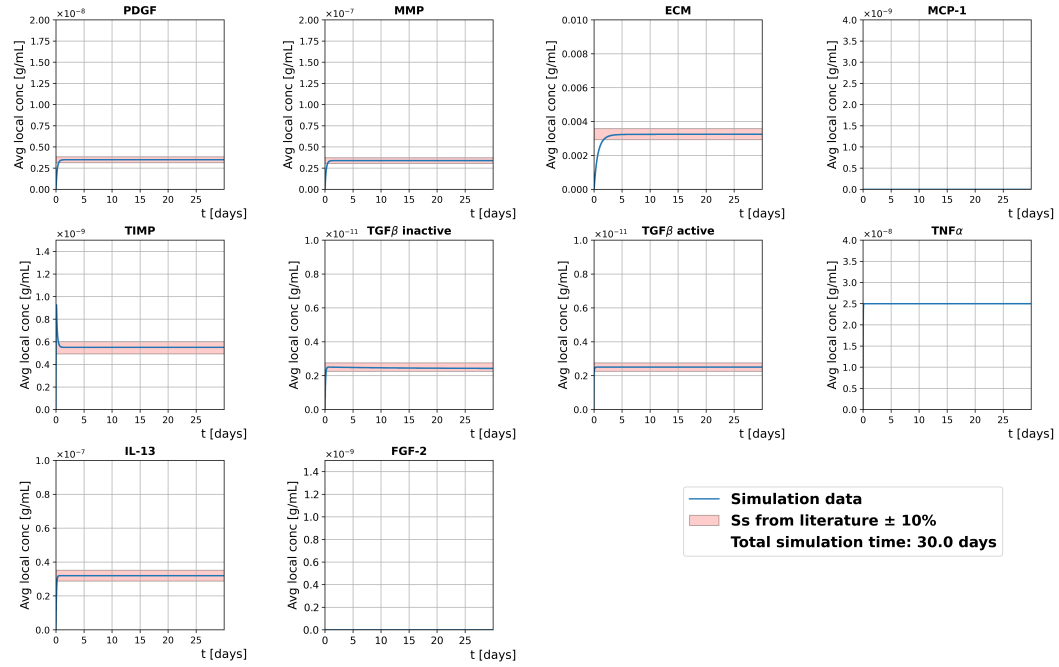

(a)

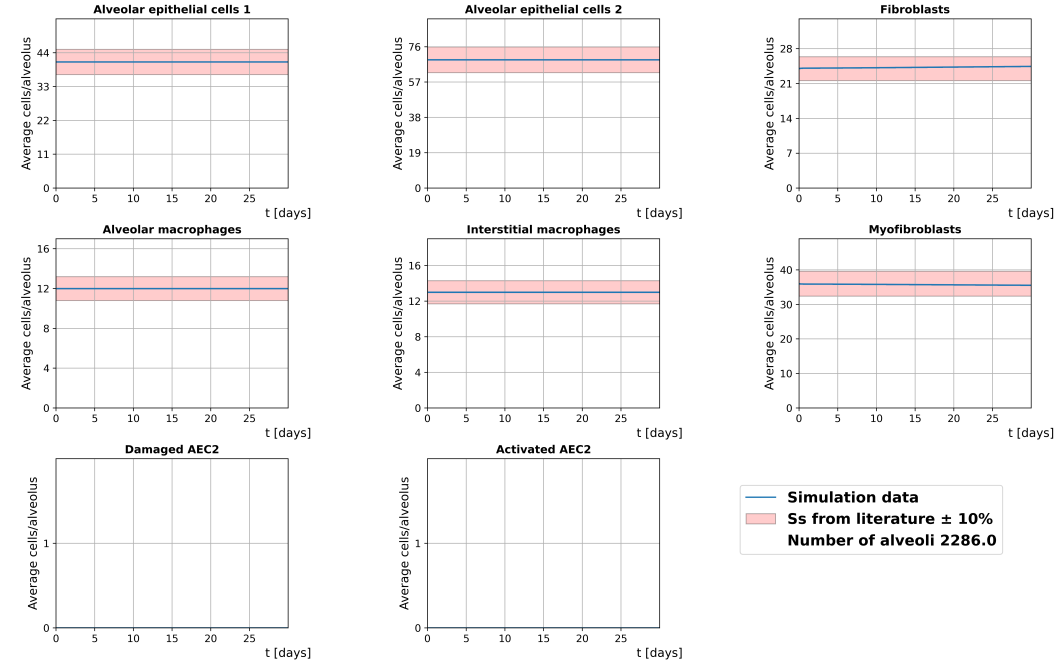

(b)

Figure 3.4: Time evolution of the extracellular mediators' average local concentration (**a**) and the average number of cells per alveolus (**b**) in homeostatic conditions. Red bands show the steady-states from the literature ±10%.

decline in the number of AEC1 cells that has been experimentally detected in lung fibrosis patients as a depletion in epithelial integrity [97].

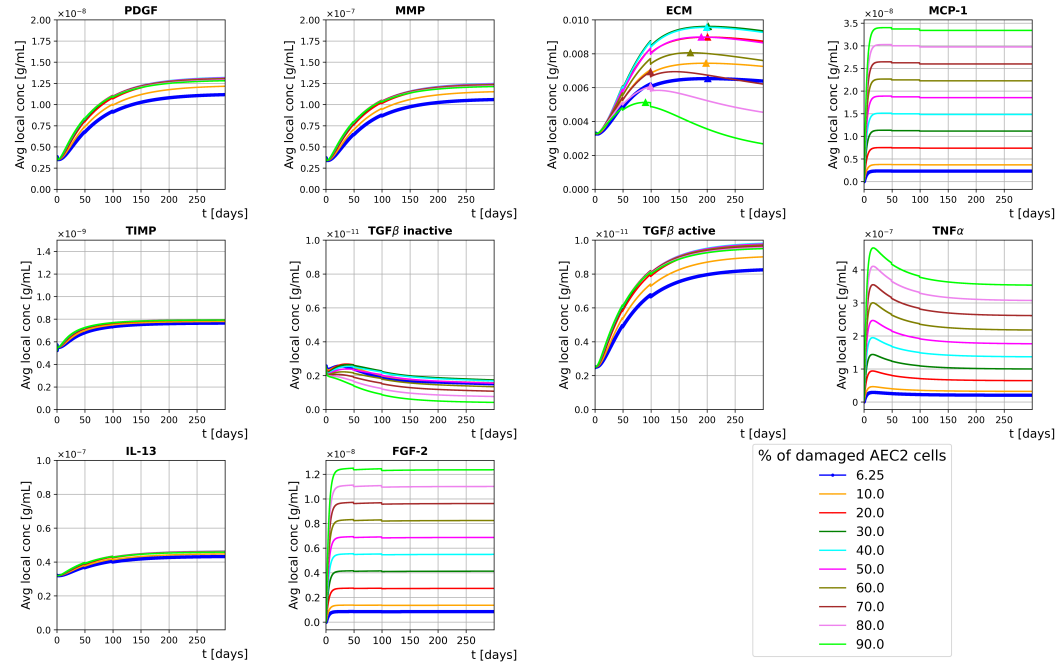

(a)

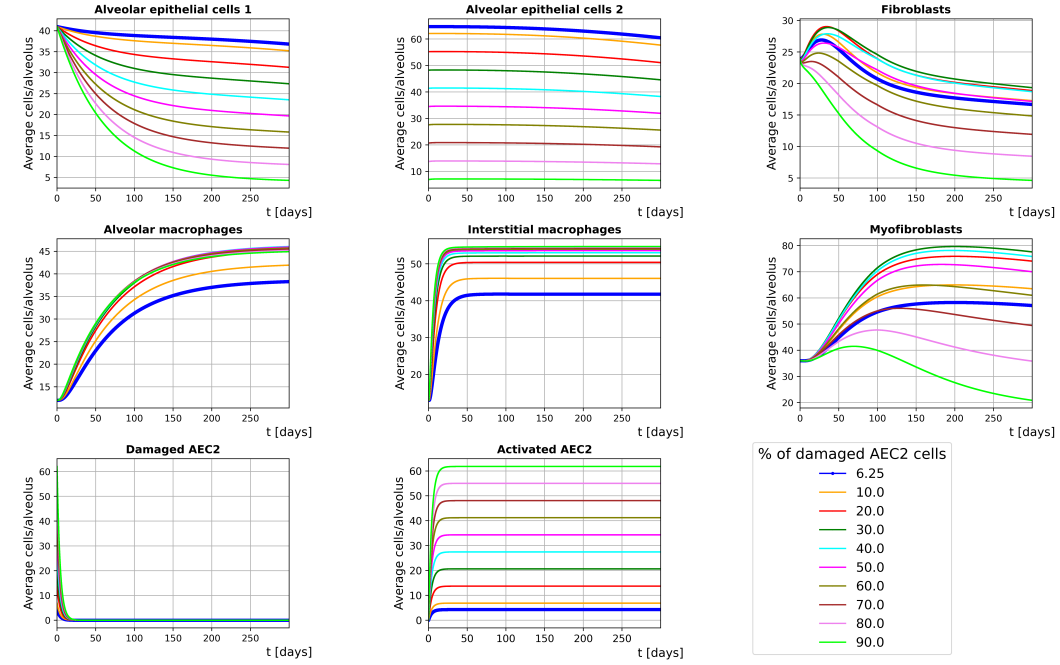

(b)

Figure 3.5: Time evolution of the extracellular mediators' average local concentration (a) and the average number of cells per alveolus (b) with initial heterogeneous damage. Different colors show different initial average fractions of damaged AEC2, and the thicker lines are used for $\overline{f}$ = 6.25%

In order to assess how the degree of damage correlates with the ECM distribution across the simulation space, the ECM concentration in each cell-hosting voxel of the diffusion grid is measured during the last

time step of the 300-days simulated time frame. By taking the ECM concentration as a surrogate for the attenuation coefficient (the use of which to monitor lung fibrosis is ordinary in the clinic [141]), we show the results through density distribution histograms in Figure 3.6.

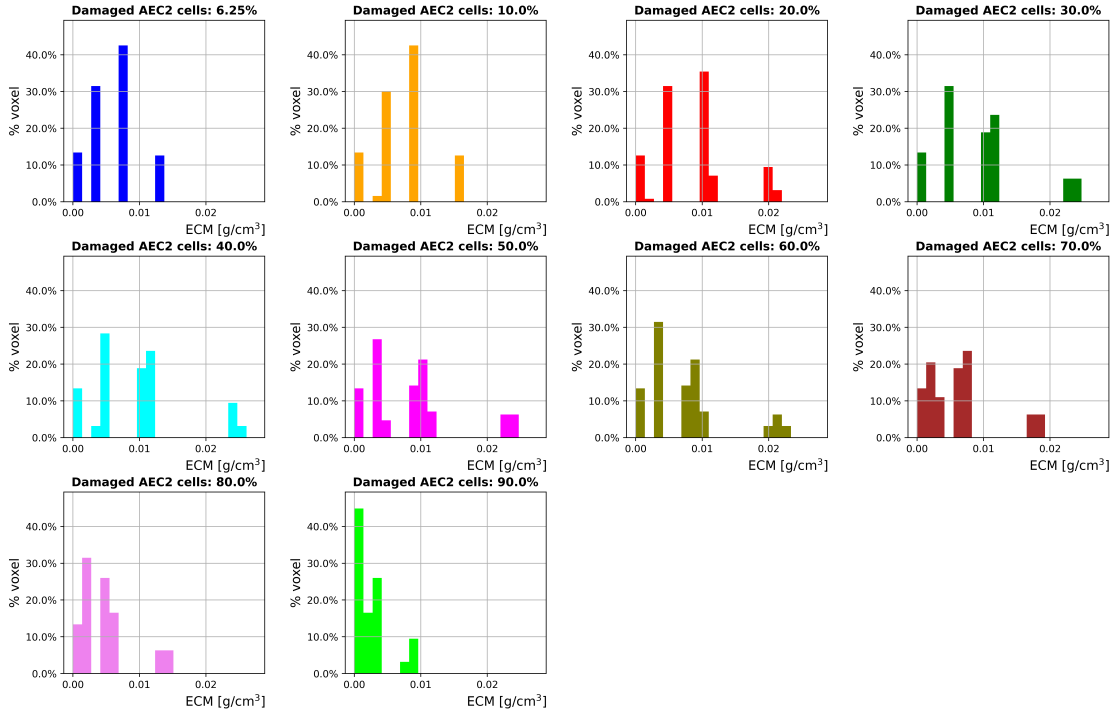

Figure 3.6: ECM distribution histograms for different initial fractions of damaged AEC2 cells (damage is heterogeneous). Shown is the ECM concentration from the cell-hosting voxels of the diffusion grid at the last time step of a 300-days simulated time frame. The ECM concentration is used as a surrogate for the Hounsfield CT units, while the voxel percentages represent the volume fraction filled with a certain amount of ECM.

Although Figure 3.6 provides the density distribution histograms for a late fibrotic phase only, the trends shown are qualitatively in agreement with the results provided in [55, 141], where lung fibrosis is induced by RT in mice. As expected, a right shift is observed for $\overline{f} \leq 40\%$, while the ECM density distributions progressively shift towards left for higher $\overline{f}$ values. It should be noted here that this kind of simulation output could be compared (after an appropriate conversion) against clinical lung CT readings, a feature that cannot be provided by 2D models and/or averaging methods. The three-dimensionality of our model enables the emergence of peculiar patterns and provides additional information to the curves showing the average ECM concentration. Interestingly, multiple animal and human studies [52, 55, 141, 142, 143, 144] have shown that higher irradiation doses (corresponding to larger amounts of initial damage) correlate well with sharper changes in CT density (and, therefore, ECM accumulation). This notwithstanding, the pathways that are triggered following greater initial damage to the AEC2 cells (as seen in RT treatments) have not been fully understood yet; therefore, we provide preliminary results and an introductory framework that can be employed for further research on radiation-induced lung fibrosis.

3.3.3 Sensitivity Analysis

We performed a parameter sensitivity analysis (see details and motivations in Section Sensitivity Analysis) by altering the following selected parameters: $\lambda_{ECM,TGF\beta}$, $\lambda_{TGF\beta,IL13}$, ECM_{sat}, λ_{M01}, and $\lambda_{F,AEC2}$(definitions are provided in Section Hybrid Multi-Agent-Based Model). Each parameter is altered by $\pm$10%, and the characteristics (both the cell numbers and the substance concentrations) are measured after a simulated time frame of 30 days so that the steady-state is reached (in homeostatic conditions). The relative sensitivity of the simulation readouts to the parameters listed above is shown in Figure 7.

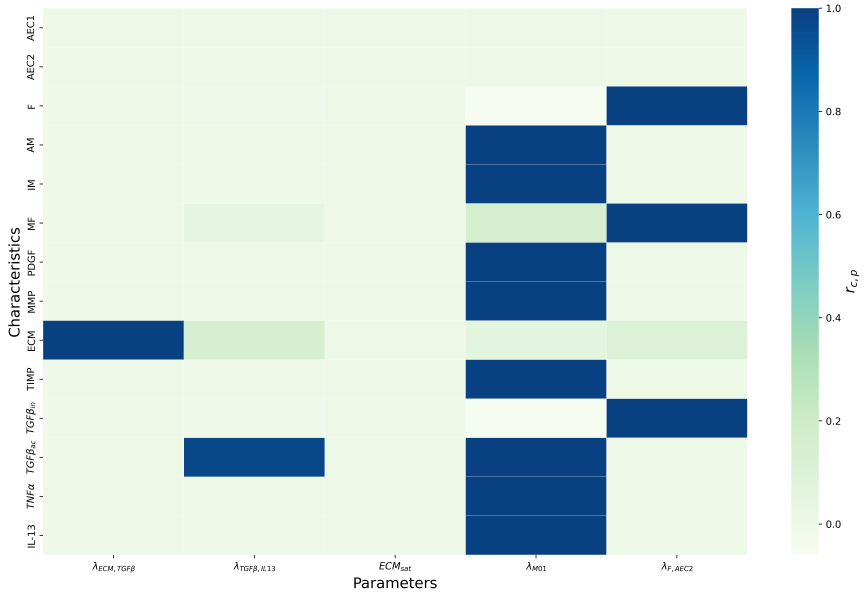

Figure 3.7: Relative parameter sensitivity map showing the impact of changes in the parameters on the characteristics. For each pair of characteristic c and parameter p, $r_{c,p}$ indicates the ratio between the sensitivity $S_{c,p}$ and the maximum absolute value of $S_{c,p}$ for that particular characteristic (i.e., computed over an entire row).

The sensitivity analysis showed that the impact of $\lambda_{ECM,TGF\beta}$ on the ECM concentration is stronger than that of any other parameter, including $\lambda_{F,AEC2}$. In other words, the effect that $TGF\beta$ has on the ECM secretion by the myofibroblasts exceeds the increase/decrease in their number induced by the same variation in $\lambda_{F,AEC2}$. Not surprisingly, λ_{M01} has proved to be the parameter with the biggest impact (among the five selected) on almost 60% of the characteristics. In fact, it controls the number of macrophages, which in turn secrete upstream regulators of several mechanisms. Finally, as expected, the number of fibroblasts and myofibroblasts and the TGFβ_{in} (secreted by F) are mostly sensitive to $\lambda_{F,AEC2}$.

3.4 Discussion

In this study, we outlined the development of a hybrid 3D ABM of lung fibrosis. The disease has been shown to be triggered by many factors, and its pathophysiology has not been fully understood yet. Within

this context, mathematical models and computational simulations have the potential to shed light on its mechanistic progression and allow for the testing of potential treatment candidates beforehand without the need for laboratories.

The simulation space of our model consists of a partial acinus built from morphometric data, in which stationary alveolar ducts act as agents whose behaviors are derived from biological findings and previous computational models. Each agent encompasses six distinct cell types secreting ten different extracellular substances. The results that we provide show that the model can qualitatively simulate the onset of fibrosis and represent a valuable extendable framework that can reproduce further scenarios on smaller and larger spatial and temporal scales. It should be noted that while the model may be seen as static, the shared extracellular space acts as a mutable environment, thus making it a time-varying network in which geometry plays a strong role.

We first calibrated the parameters of our model so that it could reproduce stationary homeostatic conditions for a time frame of 30 days. Specifically, we adjusted the secretion, proliferation, differentiation, and apoptotic rates of the cells within the agents in order to reproduce and maintain the initial conditions provided by Hao et al. [90]. To assess whether the model was able to reach its steady-state and that both the concentration of the extracellular mediators and the number of cells did not drift from the experimental values, we measured their time evolution along with their relative change. We showed that the simulated values never exceeded the 10% threshold, while their relative change remained below 0.005% for the entire simulated time frame. It should be noted that the concentration of the substances shown in Figure 3.4, Figure 3.5 and Figure 3.6 is the average concentration measured within the cell-hosting voxels of the diffusion grids.

We performed a parameter sensitivity analysis on 5 selected parameters and assessed their impact on 14 different characteristics (namely, the number of cells and the substances' concentration) in steady-state and homeostatic conditions. The analysis showed that, among the selected parameters, λ_{M01} had the greatest impact on the majority of the simulation readouts, highlighting the central role of macrophages in the model.

The second step introduced the external damage: we investigated the effect of different fractions $\overline{f}$ of damaged AEC2 cells at the beginning of the simulations and simulated heterogeneous damage by drawing those fractions from normal distributions with average $\overline{f}$ and σ = 1%. It has to be noted that incorporating heterogeneous damage allowed our model to run more realistic simulations as the amount of damage is randomly distributed in human fibrotic lungs. Moreover, the presence of randomness in individual behavior is a distinctive feature of ABM that cannot be implemented within traditional averaging methods (such as EBMs). Heterogenous fractions of damaged AEC2 cells result in different distributions of MCP1 that, in turn, show different chemoattractant effects on M1 cells. This indirectly affects the number of M2 cells within each alveolar duct and alters the amount of secreted TGFβ_a, which is reflected by different ECM patterns. The curves provided in Figure 3.6, with $\overline{f}$ = 6.5%, show that our model can qualitatively reproduce the results of Hao et al. [90]. Further, by perturbing the steady-state stability that characterizes the homeostatic situation, the symmetry of the system is broken, and we observe its evolution through an irreversible process towards its final state. We also show that increasing the fraction of damaged AEC2 leads to a corresponding rise in the concentration of ECM for $\overline{f} \leq 40\%$. Conversely, for $\overline{f}$>40%, we observed progressively decreasing amounts of ECM. The reason for this is the strong coupling between AEC2 cells and fibroblasts: as the fraction of damaged AEC2 cells exceeds the aforementioned threshold, the healthy AEC2 cells are no longer able to sustain the population of fibroblasts, an effect that is not counteracted by the additional FGF2 secreted by the active AEC2 cells. We further investigated the effects of different fractions of damaged AEC2 cells on the ECM distribution by measuring its concentration during the last time step of a 300-day simulation. The results, provided in Figure 3.6 as density distribution histograms, show a right shift of the ECM distribution for $\overline{f} \leq 40\%$ and a left shift for bigger values of $\overline{f}$.

Our study suffers from a few limitations worth noting. To begin with, the model simulates only a limited number of key pathways and cell types found in the distal airways (i.e., alveolar epithelial cells, fibroblasts, myofibroblasts, and macrophages) without taking into account oxygen diffusion and endothelial cells. Moreover, although the number of cells and the length scale of the geometrical framework were derived from in-vivo and in-vitro studies, our ABM was validated exclusively against in-silico experimental results. Finally, the cells secretion rates and the parameters describing the effect of extracellular mediators on cells secretion were adjusted with the aim of replicating experimental results and, thus, are not supported by any experimental finding.

The results provided in this paper prove that our ABM of lung fibrosis can successfully mimic the findings reported by previous studies. To the best of our knowledge, this is the first ABM of lung fibrosis implemented in three dimensions, supporting both substance diffusion and extracellular pathways on a geometrical framework that reflects morphometric data. Moreover, our model can simulate 30-day-long time frames with a time resolution of 0.1 s on a standard laptop. Accordingly, it may be employed as a starting point and easily extended for further use in the context of lung diseases (such as COVID-19 and asthma) by implementing additional layers of complexity, both on smaller and larger spatial scales as well as multiple sources of damage. Our multi-level damage approach might be of interest for simulating radiation-induced injuries as cells irradiated at different doses experience varying amounts of damage. The optimization of RT treatments and calculations of NTCP after irradiation are examples of applications that suffer from the limitations of the analytical models; these applications could benefit from the 3D framework of this ABM. Indeed, even stochastic EBMs have been proven to provide fewer scenarios and emergent patterns than ABMs in biomedical contexts [145]. Moreover, the possibility to easily implement interpatient variability by changing the acinar structure, the density of alveolar ducts, the cell damage sensitivity, and the number of cells makes it well suited for studies of personalized medicine and the clinical testing of drugs.

4 An Agent-Based Model of Radiation-Induced Lung Fibrosis

This chapter was published in 2022 in Symmetry Vol. 23, Issue 22, Nicolò Cogno et al. ”An Agent-Based Model of Radiation-Induced Lung Fibrosis”, Copyright MDPI (2022) [81].

4.1 Introduction

RILF and IPF are chronic lung diseases characterized by progressive stiffening of the alveolar walls leading to respiratory failure and eventually death [91, 93, 146, 147]. Despite sharing multiple pathways and a unique endpoint, IPF and RILF have different roots: while the former does not stem from a single known cause, the latter is the final stage of a causal sequence triggered by intracellular and extracellular ionizations.

Regardless of the damage source, AEC2 play a central role as triggers of both IPF and RILF [32, 92, 95, 98, 99, 147, 148, 149, 150]. Regarded as progenitor/stem cells, AEC2 are capable of self-renewal [98] and act as a reservoir for the terminally differentiated AEC1, which are responsible for the gas-blood exchange [94]. Irreparable injury to AEC2 is resolved either through apoptosis or a switch to a senescent phenotype [151] that allows AEC2 to secrete chemokines and cytokines that activate the immune response. Among those, the MCP1 draws the M0 into the alveolar lumen, where they differentiate into M1 macrophages [92, 93]. The latter can then differentiate into pro-fibrotic macrophages M2, which modulate the proliferation of mesenchymal cells. By secreting factors such as TGFβ, PDGF and IL13, M2 stimulates fibroblasts' proliferation and differentiation into myofibroblasts [101, 102, 103, 104]. Finally, ECM secreted by both fibroblasts and myofibroblasts stiffen the alveolar walls leading to lung scarring, which hinders breathing [107, 118] (see our previous work for more details [82]).

RILF and radiation pneumonitis constrain the maximum dose and irradiated volume in thoracic RT. Despite RT's extensive usage and proven effectiveness in cancer therapy, RILIs among lung cancer patients have been reported with a 7 to 30% incidence [33, 152, 153]. NTCP models are used to predict the risk of undesired endpoints given a patient's treatment plan [75] and can be classified into phenomenological, which rely only on clinical data, and biological, which take into account previous knowledge in the tissues' morphology [69]. Among the latter, the concept of FSUs is widely adopted [69, 72, 154] tissues are thought of as clusters of independent entities (the FSUs) capable of performing a specific organ function that can be fully regenerated by a single stem cell. The conceptual arrangement has been adopted both for serial organs, such as the spinal cord, and parallel organs, such as the lungs, for which both the alveolus and the acinus have been proposed as FSUs candidates. Among the biological NTCP models, the critical volume model [72] states that normal functioning of organs and tissues is not impaired by radiation unless the fraction of surviving FSUs falls below a certain threshold. Consequently, the critical functioning volume that must be spared to avoid complications is determined by the size of the threshold fraction. Given that an FSU can be fully restored by a single surviving clonogenic cell, the probability that an FSU is depleted corresponds to the probability that all the stem cells that belong to it (e.g. the AEC2 in the alveoli) are killed.

Although the current biological NTCP models adopt a priori non-clinical knowledge to estimate patients' risk, they lack a mechanistic representation of the undergoing processes. The biological background is limited to morphological information on the tissue (encoded in the FSUs size, shape, and number) supplemented uniquely by data on cells' radiosensitivity. The latter, combined with the delivered dose, provides an estimate of the surviving cells. Mechanisms such as indirect damage spread by irradiated cells, cell repopulation, and repair kinetics are neglected by the current models, and the picture of the radiation-induced injury progression is, thus, incomplete. In this regard, a contribution might be given by ABMs, in which autonomous entities (such as cells) are assigned behaviours and states and left free to interact with each other and with the surrounding environment [3]. According to this paradigm, agents take decisions that depend on probabilistic rates and often lead to unpredictable emergent collective phenomena. Unlike EBMs, which describe the dynamics of population averages, the decentralized approach offered by ABMs allows for individual tracking and local information exchange, providing more realistic models [145].

We implemented a 3D ABM of a human alveolar duct with cell resolution (see Figure 4.1) that simulates the onset of RILF and its progression over the course of 3 years.

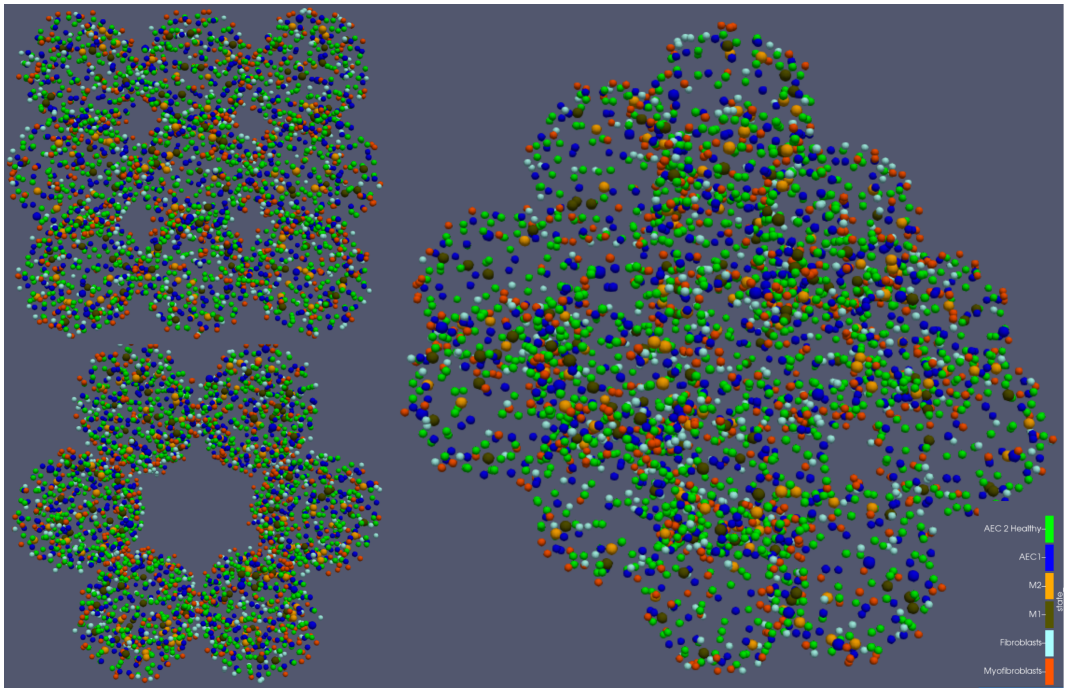

Figure 4.1: Visual output of the 3D ABM of a human alveolar duct. The structure is made up of 3 stacked layers, and each layer consists of 6 tangent alveoli. The centres of the alveoli are located on equidistant circles with a radius equal to the duct radius. Cells are represented as coloured spheres, with green = AEC2 cells, blue = AEC1 cells, brown = M1 macrophages, orange = M2 macrophages, light blue = fibroblasts, red = myofibroblasts.

The model builds on our previous work [82] with an emphasis on cell senescence and cell repopulation. A finer spatial resolution allows for radiation-induced damage to AEC2 to spread to bystanders [98, 155], while macrophages can phagocyte senescent cells [156, 157]. The grid arrangement of the simulation space constrains local impact on the surrounding environment by the cells and enables heterogeneous damage distributions. Patterns of ECM accumulation from our model match experimental findings of early and late CT changes in lung cancer patients treated with RT [53], and we show total RILF resolution for low doses as reported by previous studies on mice cells [148]. Moreover, the dose-response curve for the

ECM accumulation from our model matches the sigmoidal responses reported in the literature [31, 51]. We used the number of healthy AEC2 per alveolus to track FSU survival and observed a divergence from the theoretical values predicted by the LQ model of cell killing adopted by current biological NTCP models [69]. Based on this, we stress the need to account for microenvironmental factors when estimating the risk of RILI. Finally, we combine the ECM dose-response curve and the alveoli survival into a custom indicator for the surrogate measure of RILF severity and show that it is in agreement with experimental data from mice [158].

4.2 Results

4.2.1 Early and Late Fibrotic Response

We investigated the effect of the following model parameters on the outputs of the model: (i) the fraction of phagocytic macrophages, (ii) the AEC2 apoptotic-to-senescent ratio, and (iii) the bystander senescence threshold. More specifically, we tracked the number of cells and the concentration of the extracellular substances for 1000 days to ensure the stabilisation of the system (either towards RILF resolution or sharpening). Figure 4.2 and Figure 4.3 show the total cell number and average substances concentration for different doses (which correspond to an average AEC2 survival in the range 95% to 1%) with phagocytic fraction = 100% (i.e. all the macrophages were able to phagocyte 1 senescent cell), apoptotic-to-senescent ratio = 0 (i.e. all the damaged cells switched to the senescent phenotype and none underwent apoptosis) and bystander threshold = 2 (i.e. at least 2 senescent cells in the neighbourhood of a healthy AEC2 were needed to induce damage). Following a sharp rise in the number of damaged (and then senescent) AEC2, the immune system is triggered, and the senescent AEC2 are fully cleared within one year at all the doses. Within the alveoli irradiated at or below 4-5 Gy, the surviving healthy AEC2 are able to regenerate the whole epithelium (both AEC1 and AEC2), while for higher doses, there is an increase in the number of alveoli with no surviving stem cells. Consequently, both the M1 and M2 populations are reduced to their homeostatic levels. Due to the absence of healthy AEC2, the mesenchymal cells proliferate and secrete ECM that settles, with concentration proportional to the damage, after an initial rise.

In what follows, the term ECM concentration will refer to the average extracellular matrix concentration across the whole simulation space in g/cm^3, used as a surrogate of the more widely adopted HU. Figure 4.4 shows the early fibrotic response, that is, the absolute increase in the ECM concentration (with respect to the homeostatic values) at multiple doses 3 months after the irradiation. We separated the early component from the late one as was conducted in previous analyses [53] and fitted the experimental data using a logistic function as shown in [31, 50, 51] (we replaced the HU with the ECM concentration):

$$\Delta ECM = \frac{\Delta ECM_{max}}{1 + e^{4 \cdot \gamma \cdot \left(1 - \frac{D}{D_{50}}\right)}} \tag{4.1}$$

where ΔECM_{max} is the maximum ECM concentration, γ is the steepness of the sigmoid and D_{50} is the dose at 50% of the maximum ECM. An increase in the ECM concentration is observed even at very low doses (<2 Gy), while saturation occurs above 12 Gy. When lowering the fraction of phagocytic macrophages (while keeping the apoptotic-to-senescent ratio and the bystander threshold constant) to 60% and 80%, we observed the saturation of the ΔECM at 4 Gy and 6 Gy, respectively.

We measured the average increase in the ECM concentration at 1000 days from the irradiation for multiple doses and fitted the experimental data with the probit f unction provided in [158]:

$$\Delta ECM = \frac{1}{2} \cdot A \cdot \left\{ 1 - erf\left(\sqrt{\pi} \cdot \gamma \cdot \left(1 - \frac{D}{ED_{50}} \right) \right) \right\} \tag{4.2}$$

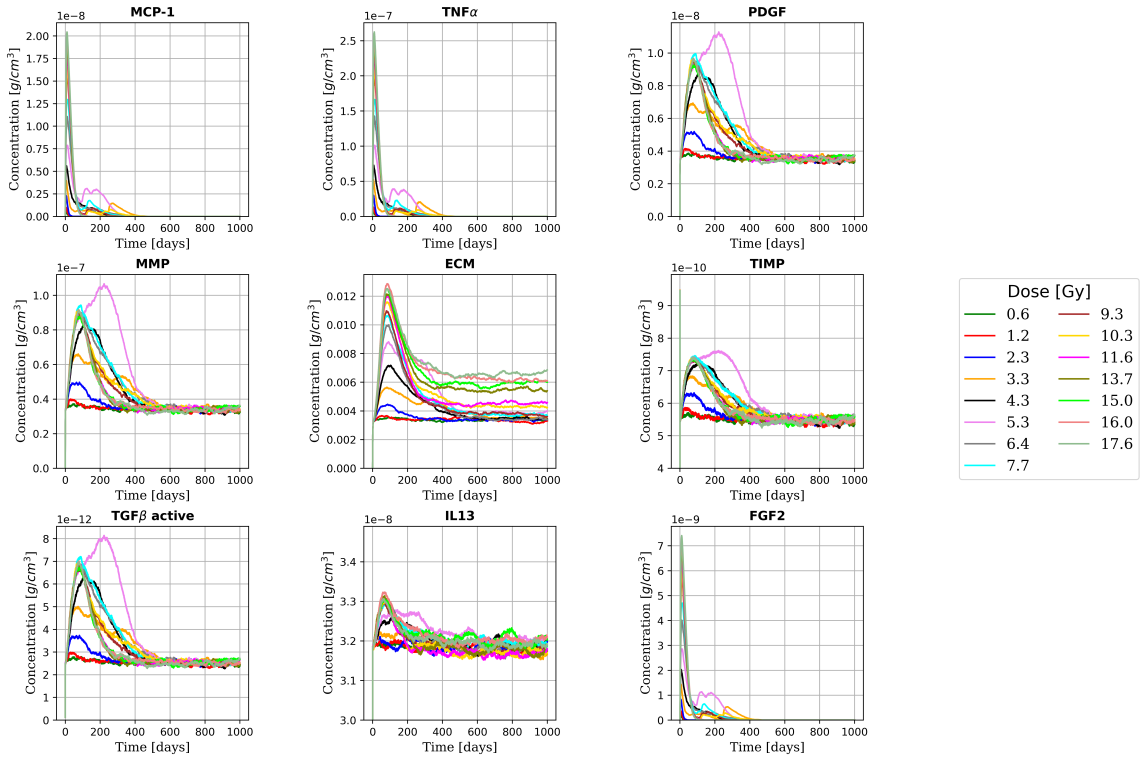

Figure 4.2: Time evolution of the extracellular substances for multiple doses. Peaks in the MCP1 TNFα, and FGF2 concentration, secreted by senescent AEC2, are observed immediately after the irradiation (see [159]). As shown in [160], a dose-dependent increase in the concentration of TGFβ (and the other macrophage-derived cytokines) is observed, followed by a restoration of the homeostatic levels in the late fibrotic phase as the senescent cells are fully cleared. A characteristic two-component pattern, where an initial dose-dependent peak is followed by a settlement, can be seen in the ECM concentration (as observed in [53]). The ECM, secreted by both fibroblasts and myofibroblasts, returns to homeostatic levels in the late phase only for doses $\leq$5 Gy.

where A is the maximum ΔECM concentration, erf is the error function, γ is the maximum steepness, and ED_{50} is the dose at 50% of the maximum ΔECM concentration. As reported in multiple studies [51, 53, 54], we assumed negligible ECM changes at late time points for doses $<$ 5 Gy and excluded those data from the experimental dataset. Given that the maximum dose (17.6 Gy) damaged 99% of the healthy AEC2, higher doses would not result in further increases of the ΔECM, and, therefore, we assume that the measured ΔECM_{max} is close to its saturation value. Overall, we observed a good agreement between the experimental data, shown in Figure 4.5, and the fitting curve. Although both the early and late fibrotic responses could be fitted by a sigmoid, we observed the halving of the maximum ECM concentration in the late phase for the doses that induced RILF. Finally, we measured A = 0.0030 and A = 0.0040 for the 60% and 80% phagocytic fraction, respectively.

4.2.2 Alveoli Survival

We investigated the survival of the alveoli 1000 days after the irradiation by counting the number of surviving healthy AEC2 per alveolus. We made the assumption that only AEC2 can be damaged by irradiation, and damaged cells can either undergo apoptosis or become senescent. In either case, cells lose

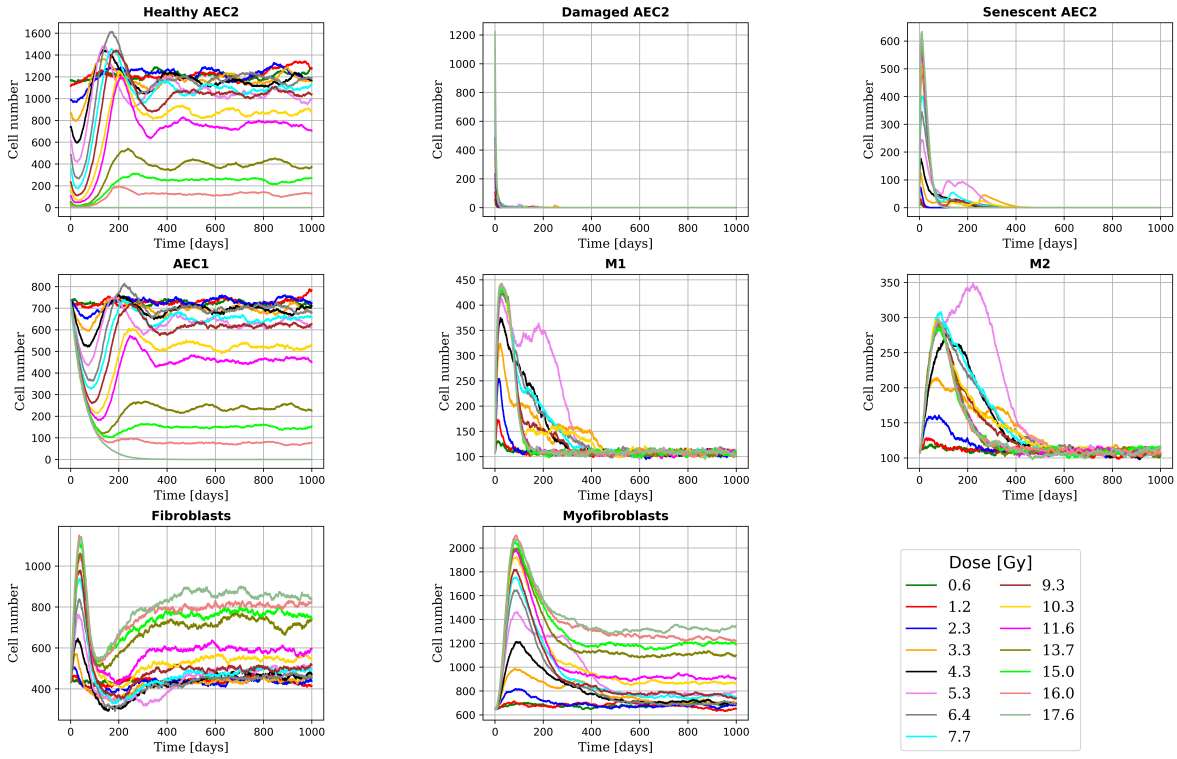

Figure 4.3: Time evolution of the total number of cells for multiple doses. As shown in [148], the AEC2 population is fully restored at low doses, while above 5 Gy, the increase in the number of senescent AEC2 (which grows with the dose) leads to the complete depletion of the healthy ones in a fraction of the alveoli (see Section Alveoli Survival). Consequently, the total number of healthy AEC2 decreases and then settles, followed by a decay in the AEC1 population. M1 macrophages, triggered by the damaged epithelium, accumulate proportionally to the number of senescent AEC2 and later on differentiate into M2 macrophages. In the later stage of fibrosis, following the clearance of the senescent cells, a decrease in the macrophage population is observed [161, 162]. Finally, the population of mesenchymal cells, whose proliferation is stimulated by macrophages and senescent AEC2 in the early phases, settles at higher levels (with respect to homeostasis) in the alveoli depleted of healthy AEC2.

their clonogenic potential. Further, for the sake of simplicity, we did not take into account the severity of the damage or repair mechanisms; thus, a cell can either be damaged or healthy. As shown in Figure 4.3, all the senescent AEC2 were removed by the immune system within one year and, therefore, each alveolus that retained at least one healthy AEC2 restored the whole epithelium and did not differ from an irradiated one when the measurement was performed. As reported by previous studies, each alveolus in our model represented an FSU that could be fully regenerated by the AEC2 acting as stem cells. Building on the concepts outlined in the critical volume NTCP model [69, 72], where the survival probability of an FSU is given by the probability that at least one of its stem cells survives, as shown by Equation 4.3, we fitted the experimental data on the surviving fraction of the alveoli using the aforementioned LQ model, which was adopted to estimate the survival of a single cell when irradiated at the dose D.

(4.3)

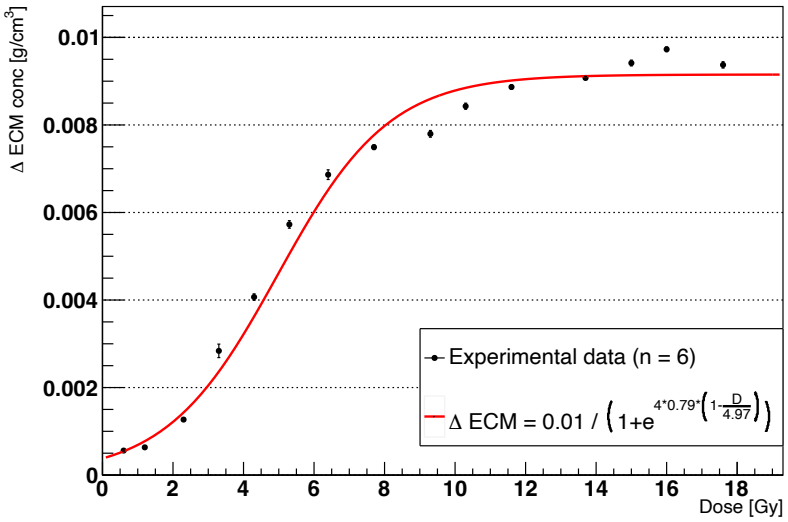

Figure 4.4: Dose-response curve for the early ECM concentration increase after 3 months with phagocytic fraction = 100% (n = number of experiments).

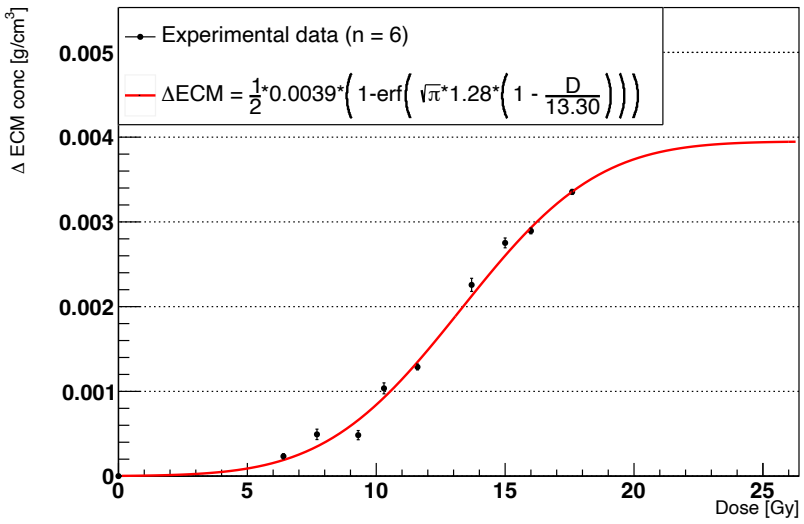

Figure 4.5: Dose-response curve for the ECM concentration increase after 1000 days with phagocytic fraction = 100% (n = number of experiments).

As can be seen in Figure 4.6 the LQ curve with $\alpha/\beta = 2$ is not in agreement with the experimental data and would predict lower survival for the doses at the end of the simulated range.

4.2.3 RILF Severity Index

As seen in a previous study on RILF in mice [158] where a FI was introduced, we implemented our own surrogate measure of RILF severity, the RSI. To make comparisons between the RILF and the FI reasonable,

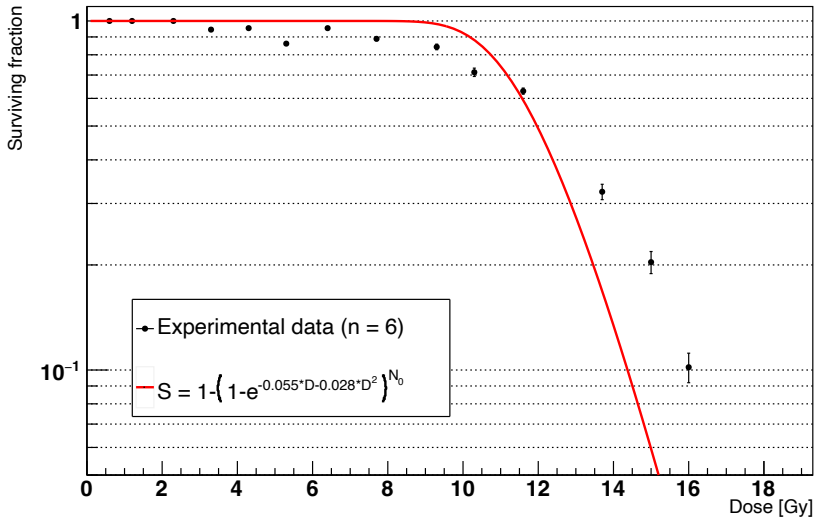

Figure 4.6: Alveoli survival after 1000 days with phagocytic fraction = 100% (n = number of experiments).

we defined the RSI as follows:

$$RSI = \sqrt{\Delta\overline{ECM_{conc}}\uparrow \cdot \Delta V_{surv,FSU}\downarrow} \tag{4.4}$$

where $\Delta\overline{ECM_{conc}}\uparrow$ is the average increase in the ECM concentration across the whole simulation space (in g/cm^3) and $\Delta V_{surv,FSU}\downarrow$ is the decrease in functioning distal lung volume given the total volume of the surviving FSUs (in cm^3). The experimental data are shown in Figure 4.7 and were fitted using the equation provided in [158] and presented in Section Early and Late Fibrotic Response (Equation 4.2). Again, we assumed negligible ECM changes at late time points for doses < 5 Gy and excluded those data from the experimental dataset. Figure 4.7 shows good agreement between the experimental data and the model curve; thus, the RSI matches the FI quantitatively up to a proportionality constant. We expect parameter A to saturate for D > 17.6 Gy, which would lead to 0% FSU survival.

4.2.4 Effects of AEC2 Apoptotic to Senescent Ratio

Previous studies [99, 148] have attributed the onset of RILF and IPF to the emergence of the senescent phenotype among the AEC2 rather than their apoptosis. Consequently, we investigated the impact of different values of the AEC2 apoptotic-to-senescent ratio on the survival of the alveoli. Given a certain amount of damaged cells, we lowered the fraction of senescent AEC2 and increased the apoptotic one, and the results are shown in Figure 4.8. As expected, due to the ability of the healthy AEC2 to repopulate the depleted alveoli and the lack of damage-spreading cells, we observed larger fractions of surviving alveoli for lower AEC2 senescent-to-damaged fractions. Notably, full resolution of the RILF was achieved for ratios $\leq 50\%$ and dose ≤ 10 Gy.

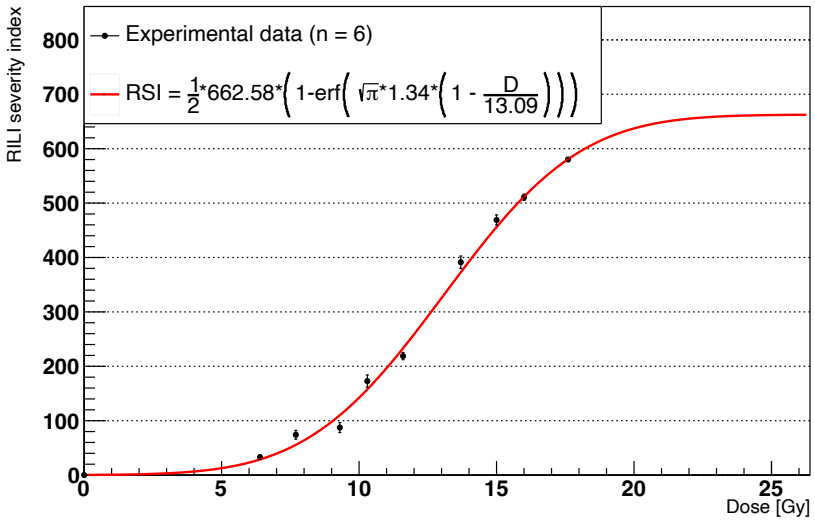

Figure 4.7: RILI severity index after 1000 days with phagocytic fraction = 100% (n = number of experiments).

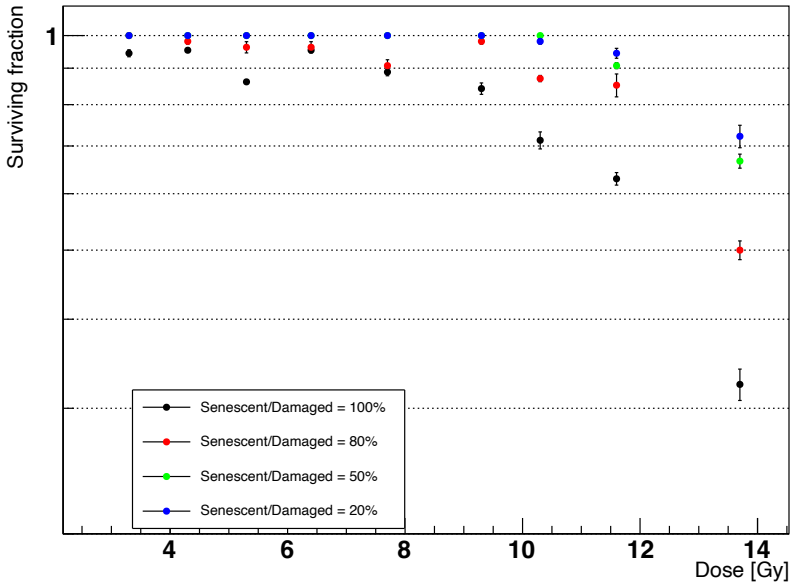

Figure 4.8: Alveoli survival after 1000 days with phagocytic fraction = 100% and different senescent to damaged AEC2 ratios. Senescent/Damaged = x% means that, after the irradiation, a fraction x of the healthy AEC2 shifted to the senescent state, while the remaining 1 - x fraction underwent apoptosis.

4.3 Discussion

RILF imposes strong constraints on the doses that can be delivered to thoracic tumours, limiting the potential benefits of RT. Understanding its pathophysiology and estimating the probability that normal

tissue complications arise, given a combination of dose and irradiated volume, is of paramount importance. Moreover, given the similarity between RILF and IPF, the latter would benefit from further knowledge of the progression of the former. Current NTCP models are built on a phenomenological basis and rely on clinical experience to determine the tolerance doses for the organs at risk. The lack of a mechanistic description of the undergoing phenomena might lead to oversimplified models of the radiation-induced injuries featuring restricted sets of input parameters and being unable to simulate the effects of post-irradiation treatments.

In this study, we implemented an ABM of a human alveolar segment and simulated the onset of RILF after the irradiation with single-fraction X-rays. We downscaled the model presented in our previous work [82] to the cellular level and added key cellular behaviours that have been documented both in RILF and IPF, such as cell repopulation, senescent cells clearance, and bystander senescence [155, 163, 164]. Our study emphasizes the role of cellular and molecular mechanisms in NTCP modelling and shows the time evolution of the RILF status. After testing several combinations of the bystander threshold parameter (i.e. the minimum number of senescent neighbours needed to trigger the phenotypic switch for a healthy AEC2) and phagocytic fraction (i.e. the fraction of macrophages able to remove senescent cells), we set them to 2 and 100%, respectively. When using these values, we observed full clearance of the senescent cells and epithelial recovery at doses < 5 Gy, as shown by Citrin et al. [148].

Our model, consisting of 18 alveoli organized in a cylindrical shape and 8 different cell types, was calibrated in homeostatic conditions using the results from the IPF model by Hao et al. [90]. Radiation-induced damage was simulated as a shift, for the AEC2, from the healthy to the senescent phenotype, with higher doses corresponding to larger damaged fractions. Experimental data from a study on the survival of mice AEC2 [165] were fitted using the LQ model curve that provided a dose-survival relation. By means of that, we simulated the irradiation of the alveolar duct within the dose range [0.6-17.6] Gy (which corresponds to 95% to 1% cell survival), and we tracked the total number of cells for each cell type and the substances concentration for 1000 days following the irradiation. In particular, the increase in the average ECM concentration and the decrease in the number of epithelial cells (both AEC1 and AEC2), hallmarks of tissue stiffening and inability to recover, respectively, were adopted as measures of RILF severity. A significant increase in the ECM concentration was observed at 3 months following the irradiation due to the spread of the senescent AEC2 and the consequent rise in the number of mesenchymal cells. The subsequent clearance of the senescent cells from the macrophages reduced the inflammation, and the homeostatic conditions were restored for the alveoli irradiated at doses < 5 Gy circa. Although all the senescent AEC2 were eventually removed at each simulated dose, some alveoli (where the number increased with the dose, as will be detailed in the next section) were fully depleted from the epithelial cells and underwent a permanent increase in the ECM. Our results, showing two distinguishable fibrotic responses, an early and a late one, are consistent with patterns detected in human lungs irradiated with photons [53, 54, 166] where density changes with respect to the baseline were measured at different time points. Moreover, the time-to-peak for the early response matches quantitative experimental data reported in the literature [51, 53]. Finally, as shown in Figure 4.4 and Figure 4.5, a good agreement was observed between the increase in ECM concentration as a function of the delivered dose and the models provided by [51] and [158] for the early and late response.

Building on the concept of the FSUs, widely used in modern biological NTCP models such as the critical volume model [69, 72], we measured the alveoli survival for multiple doses at 1000 days from the irradiation. Specifically, we identified the alveoli as FSUs of the lung in our model and classified as killed the alveoli fully depleted from the healthy AEC2. We fitted our data using the survival curve used in the critical volume model, which assumes that the probability that an FSU is killed is given by the joint probability of having all the stem cells killed, where the survival of a stem cell follows the LQ model. Figure 4.6 shows discrepancies between our data and the given model, with lower survival predicted by the model for the doses at the higher end of the simulated range. We suppose that the cause of this difference is the AEC2

repopulation not being compensated by the bystander senescence mechanism. Consequently, we argue that the temporal evolution of the RILF should play a role when modelling NTCP, as the FSUs survival might not be fully described by the LQ model alone.

We introduced a custom indicator, the RSI, as a surrogate measure of the RILF severity. Based on the idea of the fibrosis index implemented by Zhou et al. [158], the RSI is a positive number that measures the fibrosis damage by combining the depletion of the alveoli (and therefore AEC2 and AEC1) with the increase in the average concentration of the ECM. For each dose > 5 Gy, we computed the reduction in the functioning lung tissue as the loss of the volume due to the depleted alveoli and measured the average rise in the ECM concentration with respect to the homeostatic values at 1000 days from the irradiation. The results, which we fitted using the equation provided in [158], show quantitative agreement with the model parameters γ and ED_{50} (while the fibrosis index differs by a multiplicative constant). Taken together, these outcomes support the RSI as an alternative to the FI for computational simulations where a direct measure of the decrease in the functioning volume might not be available.

To investigate the impact of the senescent AEC2 on the RILF severity, we measured the alveoli survival with multiple senescent-to-damaged ratios when irradiated at different doses. Despite the increase in the number of apoptotic AEC2 and, as expected, lowering the fraction of senescent AEC2 from 100% to 20% increased the alveoli survival from 33% to 72% at 13.7 Gy. Notably, this feature could be exploited to simulate the effects of senolytic drugs on lung tissue, which have been shown to be able to reverse persistent RILF and IPF in mice [167, 168, 169] . The accumulation of senescent cells with age in the human lungs [170, 171], along with the finding that ageing is among the major risk factors for RILI [33, 42, 172], further support the relationship between the senescent AEC2 and RILF severity. Our work could therefore set the basis for modelling and testing the modulation of NTCP when RT is combined with drugs ([173] is an example of an ABM where the impact of chemotherapeutic drugs is simulated). Such models could then be exploited to optimize the treatments as a step towards personalized medicine.

This study showed that the model could replicate results published in the literature and highlighted discrepancies between the alveoli survival predicted by the critical volume model and our simulations. Contextually, we draw attention to the importance of both cell-cell and cell-environment interactions which introduce a time dependence in the survival curve of the alveolar stem cells.

4.4 Materials and Methods

We developed a hybrid ABM of an alveolar segment in a three-dimensional space that simulates cellular dynamics and molecular signalling following radiation-induced damage. Our model focuses on cell-scale behaviours and provides insights into RILF and normal-tissue complication modelling. In the following sections, we provide a detailed overview of the model implementation and present its main features. For a complete list of the model's parameters, see the Supplementary Material (available online).

4.4.1 Software Platform and Modelling Environment

Our model was developed using BDM (version v1.03.15-9589c6e2, Copyright (C) 2022 CERN & University of Surrey for the benefit of the BDM collaboration. All Rights Reserved), an open-source framework for building biological ABMs [4] in C++. Prototype simulations were performed on a MacBook Pro 2018 running macOS Monterey on a 2.3 GHz Quad-Core Intel Core i5 processor with 8 GB RAM, while a compute node of the Lichtenberg HPC system running CentOS 8.2 on 2×2.3 GHz Intel Cascade-Lake AP 48-cores processor (96 total cores) with 384 GB RAM was used for simulations requiring more than one day and testing multiple parameters. The PDEs describing the diffusion of the extracellular substances were solved

using the FTCS, while BCs were set to ”closed” to mimic an insulated environment. To account for the depletion of interacting substances (such as the ECM, MMP, and TIMP), the BDM FTCS algorithm was refined, and binding coefficients were included. The simulation space was defined as a (2000 $\times$ 2000 $\times$ 2000) μm^3 cube to fit an alveolar duct, and the 3D diffusion grid was split into cubes of side 500 μm to match the typical size of a CT voxel. The simulation time step was set to 1 s to ensure that the CFL stability condition was satisfied for the diffusion coefficient of each substance involved in the simulations. To reduce the total simulation time, the frequency of the default BDM standalone operations that regulate mechanical interactions among cells and cell behaviours was set to 10 simulation time steps. All the outputs derived from the simulations (as described in the following section) were printed on ROOT files and later on analysed using custom Python scripts (see, for example, [174]).

4.4.2 Geometric Frame and Operations

The lungs' airway tree culminates in the acinar airways, which are responsible for the gas-blood exchange [25]. Within them, independent structures named acini bifurcate into alveolar ducts (or segments), where stacked alveoli are arranged in cylindrical shapes. To investigate the impact of cell-scale behaviours such as senescent cell clearance, bystander damage, and repopulation, we downscaled our previous model [82] and simulated a human alveolar duct where spherical agents represent alveolar cells. Alveolar ducts can be seen as hollow cylinders whose walls are lined with alveoli [25]. These latter have been previously described as three-quarter spheres with an opening that faces the lumen of the ducts. As detailed in our previous work, given the average radius of an alveolus (approximating a sphere) and the average length and diameter of an alveolar duct, we implemented an 18-alveoli model of alveolar duct, where 3 rings of 6 tangent alveoli are stacked atop one another (sizes are given in Table 4.1). At the beginning of each simulation, newly created agents are assigned a type and randomly distributed on the 18 spherical surfaces. Our model features 3 major cell categories which inherit methods and properties (such as the identifier of the alveolus they belong to) from a common alv_cell type. Simulated cells are categorized as follows:

Catergory	Type	Initial Number per Alveolus	Source
Epithelial	AEC1	41	[29]
	AEC2healthy	69	[29]
	AEC2 damaged	0	
	AEC2 senescent	0	
Macrophage	Macrophage M1	6[1]	[29]
	Macrophage M2	6[1]	[29]
Mesenchymal	Fibroblast	24[2]	[29, 90]]
	Myofibroblast	36[2]	[29, 90]]

[1] Contrary to our previous model, we include only alveolar macrophages (M1 and M2) and neglect interstitial macrophages. We assume that M1 and M2 are equally distributed in homeostatic conditions. [2] See our previous work [82].

Table 4.1: Cell types and numbers.

Epithelial cells are positioned one alveolar radius from the alveolus centre, while mesenchymal cells and macrophages are located slightly further from (in the interstitial space) and slightly closer to (in the alveolar lumen) the alveolar centre, respectively.

As mentioned in the previous section, the simulation space is partitioned into cubic voxels that make up

the diffusion grid. We provided all the cells in our model with a function that allows them to measure the concentration of all the substances within the voxel where they reside. We used this function to both inform the cells about changes in the substances' concentration (to which they might react) and exploit the cells as probes to constantly track the average concentration of all the substances across the whole simulation space (for a complete list of the substances involved in the simulation as well as diffusion constants, decay and binding coefficients, see our previous work). To do this, and to record the total number of cells of each type, we used the update time series operation provided by BDM with a frequency of 1 h. Moreover, we developed custom standalone operations with a 10 s frequency to:

- determine the number of surviving alveoli;
- simulate the secretion of IL13 from lymphocytes (which, for simplicity, are not included in the model) at the centre of each alveolus [175];
- simulate the inflow of fibroblasts in the interstitial space with a rate that depends on the number of AEC2 per alveolus. According to the literature [176, 177], prostaglandin E2 secreted by AEC2 inhibits fibroblasts' chemotaxis and proliferation. We modelled this phenomenon using a reverse Hill function with coefficient 1 (to avoid abrupt changes in the fibroblasts' flow) multiplied by a constant rate. We assumed the Hill constant to be equal to the initial number of AEC2 per alveolus to reduce the number of unknown parameters and tuned the constant influx rate to keep the number of fibroblasts in homeostatic conditions constant;
- simulate the flow of monocytes into the alveolar space. The rate of monocytes entering each alveolus is constant in homeostasis and is incremented in the presence of senescent AEC2, which secrete MCP1 [97] (and is measured locally). See our previous work for more details [82].

4.4.3 Cell Behaviours

Cells' actions can be encoded and grouped into agents' behaviours which in turn are triggered by external signals or executed at a specific rate. Depending on their type, cells in our model are assigned custom behaviours when they are added to the simulation and sequentially perform the prescribed activities until they are removed. In what follows, we provide an overview of all the behaviours implemented in our model and emphasize the major changes with respect to our old work [82]. As mentioned before, biological behaviours are executed with a frequency of 10; that is, 1 biological time step is equal to 10 diffusion time steps.

Secretion

Cells secrete extracellular substances by changing their concentration within the voxel where they are located. The amount released by a secreting cell at each iteration can be constant or depend on external factors as detailed in what follows (see [82, 90] for a deeper overview of the mechanisms):

- M2: PDGF (constant rate), MMP (constant rate), TIMP (constant rate), IL13 (constant rate), TGFβ_{active} (rate is positively affected by IL13 concentration);
- M1: TNFα (constant rate);
- F: TGFβinactive (constant rate), ECM (rate is affected with inverse proportionality by ECM concentration; no secretion if the concentration exceeds a saturation threshold);

- MF: ECM (rate is positively affected by TGFβ_{active} concentration);
- Senescent AEC2: TNFα (constant rate), MCP1 (constant rate), FGF2 (rate is positively affected by TGFβ_{active} concentration).

Damage Spreading and Clearance

The central role played by senescent cells in RILI and IPF has been strongly emphasized in multiple studies [32, 92, 95, 98, 99, 147, 148, 149, 150]. More specifically, senescent AEC2 are involved in both the initiation and spread of the inflammatory process that, if unresolved, triggers the fibrotic process [150]. Unlike our previous work [82], in which the number of activated (i.e. senescent) cells damaged at the beginning of the simulation remained constant, here, the fraction of senescent cells is modelled as dynamic, both in size and position. As with multiple behaviours described in the following sections, downscaling our previous model allowed us to investigate this process.

Due to their high radiosensitivity and key role as stem cells (AEC1 are not able to differentiate [178]), we assumed that only AEC2 could be damaged by the irradiation. Irradiated cells in our model are either removed from the simulation (to simulate their apoptosis which has been proved to increase only in the first few weeks after the irradiation [148]) or switch temporarily to the damaged state [151], the duration of which depends on a random variable. Damaged cells, although slowly migrating (see the section Migration), cannot spread the damage but become able to do so as they turn senescent. In fact, senescent AEC2 acquire a SASP through which they are able to trigger the immune system and damage neighbouring (bystander) healthy cells, known as the senescence-induced senescence [155]. Our implementation of the bystander senescence behaviour is based on the model of radiation-induced intercellular signalling by McMahon et al. [74], in which irradiated cells can induce damage to healthy ones by secreting extracellular mediators. Although multiple studies have reported the involvement of TGFβ_{active} in the process [179, 180, 181, 182], we did not make any assumptions on the signalling molecules and instead modelled the intensity of the signal more generally using the intercellular distance. As in [74], our implementation relies on a threshold mechanism: when the number of senescent cells in the neighbourhood of a healthy one exceeds a threshold (which was tuned together with the senescent clearance mechanism described below to ensure complete recovery for low fractions of damaged cells), the "time above threshold" τ of the healthy cell is increased by one unit and decreased otherwise (if greater than 0). Since the neighbourhood of the healthy cell is defined as the group of cells within a two AEC2 diameter distance (to simulate short-range interaction), but not limited to the same alveolus, this mechanism allows for both intra- and inter-alveolus damage spreading. Finally, for a healthy cell with $\tau > 0$, the probability of transitioning to the damaged type is given by:

$$p = 1 - e^{-k\tau} \tag{4.5}$$

where k is a cell-line-specific constant. In our model, we used the value provided in [74] for the non-small-cell lung cancer H460 cell line.

Alongside the damage spreading mechanism, in this model, we introduced a behaviour to allow the immune system to perform senescent cell clearance [156, 157]. In particular, we provided the macrophages (both the M1 and M2 type, as their role in the process has not been fully elucidated yet [183]) with the ability to phagocyte senescent cells. At each time step, macrophages check whether they are in physical contact (a distance which we assumed to be 10% larger than the cell-to-cell distance) with any senescent AEC2 in the same alveolus and, if so, they can phagocyte it, provided that the macrophage has not reached its maximum capacity (determined by a phagocytic index [184, 185, 186]). Moreover, we tested multiple values for the phagocytic fraction, i.e. the fraction of macrophages that is able to clear senescent cells.

Migration

Contrary to the static nature of our previous work [82], this model features moving agents and mechanical interactions. In fact, moving to a finer scale allowed us to simulate cell migration while we relied on the implementation of the mechanical forces from a default BDM operation for the repulsion of cells in close proximity. We implemented two types of cell migration (none of them allows the cells to escape the alveolus they belong to), namely random movement and neighbourhood-informed migration.

We assumed that macrophages, mesenchymal cells, and damaged and senescent AEC2 would randomly move within the alveolus to either patrol the alveolar space (M1 and M2 macrophages), restore the ECM reserve (fibroblasts and myofibroblasts), or spread the damage while triggering the immune system (damaged and senescent AEC2). Within this group, we further distinguished cells that move at every time step from those that do not. Specifically, macrophages and mesenchymal cells in our model move constantly to perform the aforementioned activities. At every time step, a random direction (i.e. an angle in the interval $(0, 2\pi)$) is drawn from a uniform distribution and rotation matrices are used to compute the new position of the cell given its speed and the length of the time step. Moreover, macrophages that have exceeded their phagocytic capacity are not able to move anymore (see the section Damage Spreading and Clearance). On the contrary, damaged and senescent AEC2 might lose the ability to migrate properly due to radiation-induced injury. Therefore, at each time step, $\Delta\theta$ and $\Delta\varphi$ (where θ and φ represent the polar and azimuthal position of the cell) are drawn from a uniform distribution within a small range. We simulated casual absence of motion by including 0 in the range.

We implemented neighbourhood-informed migration to simulate AEC1 and AEC2 movements toward areas with low epithelial population density. In fact, AEC2 cells must migrate to regions depleted from AEC1 before starting the repopulation process, while AEC1 spread to maximize the alveolar gas-blood exchange capabilities [187, 188]. We modelled these mechanisms as follows (no assumption was made on the intercellular communication and we used the inverse-square law to model general signalling):

- The epithelial cell detects all its neighbours within an alveolar radius distance in the alveolus it belongs to (AEC1 detect other only AEC1, while AEC2 detect both AEC1 and AEC2);
- For each of the detected neighbours, the distance from the acting cell is measured;
- Using the distances from the step above, the cell determines the centre of mass of its neighbours, where each distance is weighted with the inverse of its squared normalized value;
- The cell migrates in the opposite direction from the location of the centre of mass, given a constant migration speed and the length of the simulation step.

Proliferation

Healthy AEC2 and fibroblasts are the only cell types that can (symmetrically) proliferate in our model. Due to their ability to act as stem cells, AEC2 proliferate to repopulate alveoli depleted from AEC1. In fact, it was shown that hyperplastic AEC2 are found in damaged alveoli [148]. We modelled AEC2 hyperplasia by providing the cells with the ability to check the state of their neighbours within an alveolar radius distance, which was made possible by the increase in the resolution with respect to our previous work [82]. If the number of AEC1 in the neighbourhood falls below a threshold (which we set as 20% less than the average number of AEC1 in homeostatic conditions in the monitored area), the AEC2 doubles its proliferation rate. Although more complex models of lung cells repopulation after radiation-induced damage have been developed [189], our models seek to replicate the ability of AEC2 cells to quickly and sensitively respond to local depletion of AEC1 by making use of a simple threshold mechanism. Fibroblasts, on the other hand,

proliferate during the inflammatory process. We modelled their proliferation as in [82], with a rate that depends on TGFβ_{active}, IL13, and FGF2, the latter being present only in the presence of senescent AEC2 [114, 115, 116].

Differentiation

Differentiation is a process that involves changes in a cell's phenotype and leads to the acquisition of new capabilities while others are lost. We mimicked this process by changing a cell's type, removing its old behaviours, and assigning new ones. The differentiation is a behaviour itself, and in the following, we detail those that might take place in our simulations. Unless otherwise stated, the differentiation was modelled as in [82].

We assumed that monocytes entering the alveolar space would immediately differentiate into pro-inflammatory M1 macrophages [190]. On the contrary, M1 macrophages have a constant probability of turning into M2 macrophages at each time step (tuned such that their number in homeostasis is constant), while the probability that M2 macrophages differentiate into M1 depends on the local concentration of TNFα [100] (which affects it positively, though this process is rarer than the opposite one).

Fibroblasts differentiate into myofibroblasts that collaborate in the secretion of the ECM [107, 118]. Although the myofibroblasts are almost absent from the alveolar space in homeostatic conditions, we assumed an initial level of inflammation (as was done in [90]) and tuned the differentiation rate so as to maintain a constant number of both fibroblast and myofibroblasts in homeostasis. This transition is then positively influenced by pro-fibrotic M2 macrophages through the secretion of PDGF and TGFβ_{active} [112].

Finally, AEC2, which act as a reservoir for the terminally differentiated AEC1, following migration and proliferation (as described in the previous sections), alter their phenotype at a constant rate [117, 188].

Apoptosis

We distinguish between constant and variable apoptosis. Cells that undergo constant apoptosis (AEC1, macrophages, and mesenchymal cells) are removed from the simulation at a constant rate. At each time step, each cell draws a random number from a uniform distribution, and if this number is smaller than the apoptosis rate, the removal is performed. On the contrary, variable apoptosis depends on external factors. As reported in the literature [187] healthy AEC2 increase their apoptotic rate if the number of surrounding AEC1 exceeds the homeostatic value. We modelled this behaviour as the adaptive proliferation (see Section Proliferation), doubling the AEC2 apoptotic rate when the threshold (which we set as 20% more than the average number of AEC1 in homeostatic conditions in the monitored area) is exceeded. Finally, we assumed that damaged and senescent AEC2 could not undergo apoptosis due to the short duration of the state (the former) and the phenotypic resistance to it (the latter, as shown in the literature [191]), respectively.

4.4.4 Initial Conditions

Homeostasis

As described in our previous work [82], we used a trial-and-error approach to tune the model parameters in homeostatic conditions. Except for the initial cell numbers, the size of the geometric frame, and the diffusion parameters of the extracellular substances (see Section Geometric Frame and Operations), we calibrated the secretion, proliferation, apoptosis, and differentiation rates to (i) match homeostatic experimental values reported in a previous model of IPF [90] and (ii) keep the number of cells constant (i.e.

within a reasonably small range of variation) for multiple weeks. Plots of the cell numbers and substances concentration are provided in the Supplementary Material (available online).

Radiation-Induced Damage

The radiation damage in our model was simulated as depletion of healthy AEC2. To replicate heterogeneous damage, depleted fractions for each alveolus were drawn from Poisson distributions centred on the average number of injured cells for a given dose. For each simulated dose, we estimated the surviving fraction by fitting experimental data from a study on rats AEC2 [165] (for doses < 15 Gy, due to its questionable validity at higher doses [192]) using the LQ model. To compensate for the lack of human pneumocyte data in our work, we limited our references to in vivo studies on AEC2 and neglected in vitro experiments on A549 and H460 cell lines. According to the LQ model (the most commonly used in radiation biology [10]), the survival probability (S) for a cell exposed to a single fraction of dose D is given by:

$$S = e^{-\alpha D - \beta D^2} \tag{4.6}$$

where the α and β parameters characterize the radiosensitivity of a cell line. Figure 4.9 shows the fit curve and parameters used in our simulations.

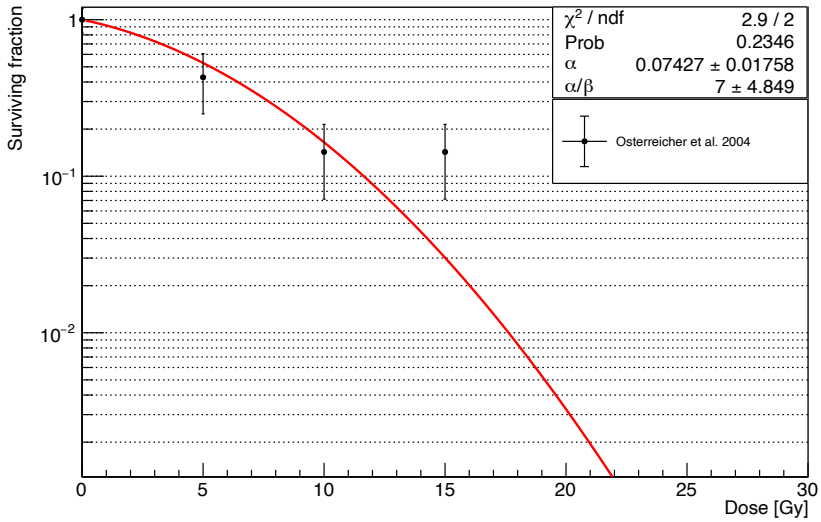

Figure 4.9: Experimental data of rats AEC2 survival from [165]. Data were fitted using the LQ model (in red) and the curve was used in the ABM to convert the simulated damaged fractions into the corresponding delivered doses.

According to our fit, the value of β is one order of magnitude smaller than α (or, equivalently, the α/β ratio is large), in agreement with results from the radiosensitivity of multiple mouse strains [69].

4.5 Conclusions

To our knowledge, our work represents the first attempt to mechanistically model RILF using the AB modelling approach. We showed that the time evolution of the ECM concentration in our alveolar duct

model could replicate early and late-response patterns observed in patients treated with RT. Moreover, the ECM concentration peak in the early response of our model is reached after 3-4 months from the irradiation, as found by previous studies. Further, we measured the FSU survival rate as a function of the dose and observed discrepancies at higher doses when fitting the data points with the critical volume model. Our RILF severity index, a surrogate measure of the disease severity based on the work done by Zhou et al., is in agreement with the experimental results shown in their mice model of RILF [158]. Finally, we highlighted the role of the senescent AEC2 as the main triggers of the RILF by reporting lower survival curves for the alveoli when increasing the initial fraction of senescent cells.

Future developments will focus on replicating a bigger portion of the lungs and coupling a radiation transport model with the aim of making voxel-voxel comparisons.

5 Mechanistic model of radiotherapy-induced lung fibrosis using coupled 3D Agent-Based and Monte Carlo simulations

This chapter delineates the implementation and characterization of the first coupled 3D AB-MC model that mechanistically simulates the onset of RILF in an alveolar segment. Our model replicates ECM patterns, RSI performance and FSUs survivals that show qualitative agreement with experimental studies and are consistent with our past results. Moreover, this chapter was submitted as a manuscript.

5.1 Introduction

Precision, efficacy and non-invasiveness have made RT a first-choice treatment option nowadays for a large portion of cancer patients. Nevertheless, the risk of developing radiation-induced pathologies remains significant and the number of reported injuries increases concurrently with the number of treatments. Notably, more than 50% of the cancer patients are treated with RT [193] and previous studies reported that thorax irradiation led to RILI (namely, pneumonitis and fibrosis) in up to 30% of the cases[33]. These pathological conditions are thought to be triggered mainly by the damaged alveolar epithelium and the resulting inflammation, if not resolved within a few weeks' time, can lead to lung stiffening and eventually death[23]. Consequently, greater efforts are required to improve our understanding of the mechanisms underlying the paths that link radiation damage and toxicity in normal (i.e. non-tumoural) tissues, with the ultimate goal of widening the therapeutic window.

To this aim, NTCP models have been implemented that estimate the probability of developing new pathologies as a function of the delivered dose for a given organ[154, 194, 195]. However, NTCP models widely employed in clinical practice restrict the set of inputs to the delivered dose distribution and a few macroscopic organ-specific parameters that fail to enfold a mechanistic description of the pathways involved. Moreover, the lack of spatial information in the DVHs that encode the dose distributions' data results in incomplete descriptions of the treatment plans and subsequent erroneous shifts of the NTCP curves[75, 196].

By combining AB modelling and a MC simulator we propose an innovative approach in an attempt to address the aforementioned shortcomings (see Figure 5.1). AB modelling is a powerful and relatively recent set of computational techniques that allows simulations of concurrent and independent entities, namely, the agents[3]. Each agent is initialized at the beginning of a new simulation with a set of rules, encoded into its behaviours, and positioned in an environment that can be sensed by and react to the agent itself. The interactions among different agents and between the surrounding environment and the agents themselves can lead to the emergence of elaborated dynamics and provide a framework to model complex systems, such as the biological ones. MC methods, on the other hand, have been extensively used to simulate the interaction of radiation with matter[76] and can provide accurate estimates of, among others, dose depositions in biological structures. In what follows we provide insights on the onset of the RILF in a coupled 3D AB-MC model of an alveolar segment. We updated our ABM of RILF[81, 82] and implemented

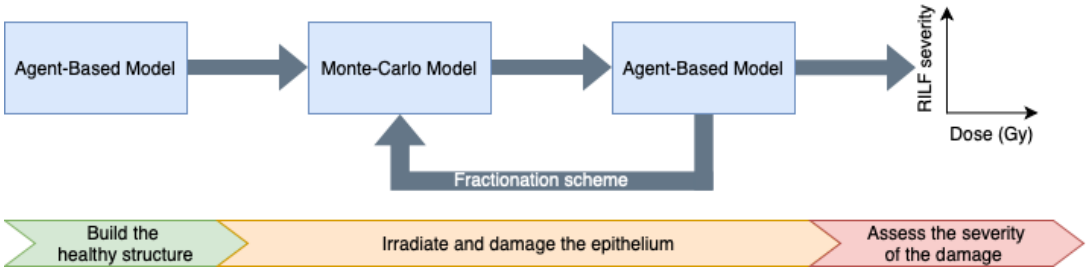

Figure 5.1: Schematic representation of the implemented workflow. The ABM is used to generate the alveolar segment structure in homeostatic conditions. The data are then fed into the MC model which replicates the geometry and irradiates it. Information about the delivered dose to each cell are then loaded into the ABM which simulates the evolution of the system. If a multi-fractionation scheme is set up, the data exported from the ABM are used as an input to the MC. If not, the data can be directly analysed to determine whether RILF onsets and, if so, its severity.

the alveolar segment geometry within the TOPAS-nBio MC extension[6]. As a result, our coupled model is now able to provide a mechanistic description of the depletion of the functioning distal airways of the lung as well as 3D spatial information about the delivered dose distributions. More specifically, this work details the implementation of the coupled model and provides a comparison between the ABM and the AB-MC models' results. Moreover, the effects of different radiation qualities as well as the impact of the bystander threshold on the outcomes are shown. Finally, we demonstrate how the use of a multi-fractionation scheme affects the model's outcomes. Temporal fractionation techniques are widely adopted in the clinics[197, 198, 199] due to their ability to spare normal tissues without losing efficacy in tumour cells killing[200]. Our results, in agreement with previous experimental studies[158], show a right shift towards higher doses for the same amount of damage when using 5 fractions with respect to a single fraction.

5.2 Results

5.2.1 Characterization of the dose distributions in the alveolar segment

Before running the full AB-MC model, different setups of the photon source for the irradiation of the alveolar segment were tested and the corresponding dose distributions compared. More specifically, doses were delivered using both an external beam with 4 coplanar fields and an isotropic source located at the center of the alveolar segment. The particle energy was set to $E_\gamma = 1keV$ for all the experiments and the total number of histories (i.e. emitted particles per field) was set to 1 million, which ensured reasonable simulation times on a common laptop. Moreover, each experiment was performed 10 times and the results averaged.

As can be seen from Figure 5.2a and Figure 5.2b, while the dose delivered with the external beam could be fitted to a Gaussian distribution that peaks at around 50% of the maximum dose with thin (although short) tails, the dose distribution from the isotropic irradiation shows two distinct peaks (at 0-1% and 10% of the maximum dose) and a long right tail. Given the symmetry of the resulting dose distribution and its closer resemblance to the beam setups used in the clinics, the external beam was used in all the experiments performed in this study.

We further analysed the effect of an increase in the number of histories in the dose distribution delivered by the external beam. Raising the number of particles from 4 millions (for 4 fields) to 30 millions (Figure 5.2c) didn't alter the shape of the dose distribution substantially, but required a greater computational cost.

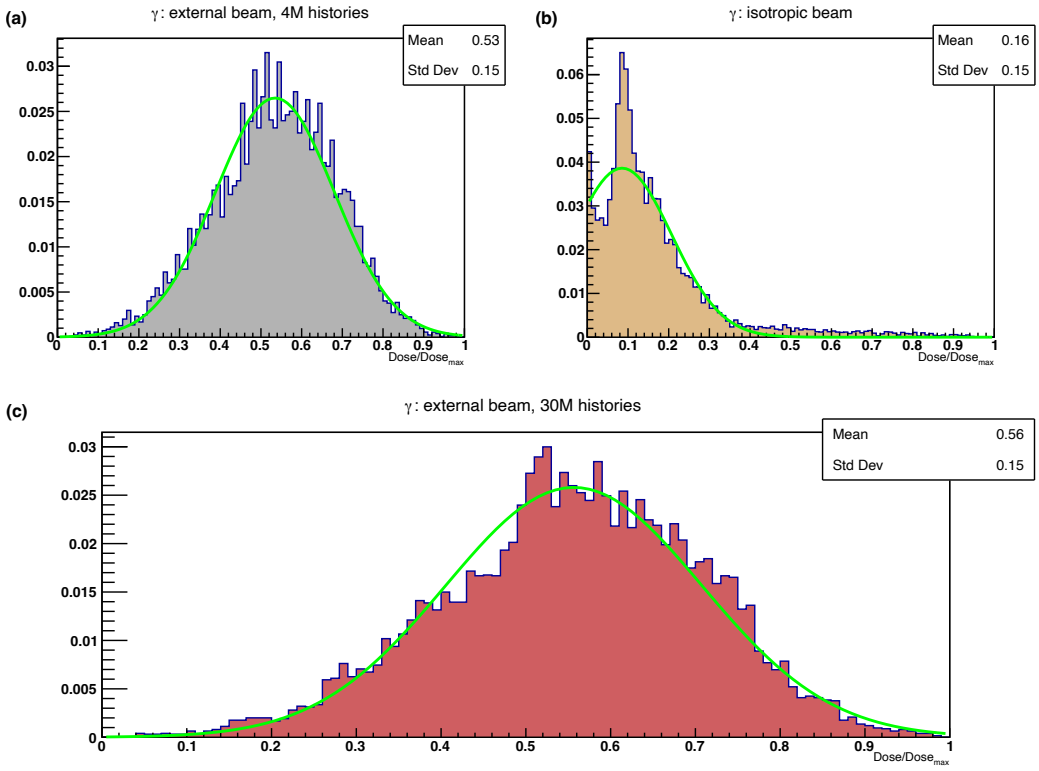

Figure 5.2: Dose distribution histograms for different setups in the alveolar segment model irradiated with photons. On the x-axis, doses are shown as percentages of the maximum delivered dose and the green curves are the best Gaussian fits for the histograms data. Panels **a** and **c** correspond to 4-fields external beams with 4 million and 30 million histories (i.e. particles) respectively. In panel **b** the dose distribution resulting from an isotropic source (i.e. a point source located at the center of the alveolar duct) is reported.

Therefore, the lower value was set in the parameter file of the MC model and used in the following simulations.

5.2.2 Simulation outcomes: ABM-MC vs ABM

To characterise the coupled AB-MC model, we compared the main simulation outcomes with those from our previous ABM[81]. In particular, we evaluated the surviving fraction of the FSUs, the RSI, the early and the late ECM fluctuations in the ECM concentration as a function of the delivered dose. To ensure that the system reached the steady state (both in terms of cell number and substances concentration), we simulated 1200 days. In the AB-MC model the dose was delivered once at the beginning of the simulation and the parameters were set to the same values as those in the ABM model (notably: phagocytic fraction = 100%, phagocytic index = 1, apoptotic-to-senescent ratio = 0 and bystander threshold = 2). As can be seen from Figure 5.3, both the early and the late components of the ΔECM (i.e. the increase in the average ECM concentration across the whole simulation space for the AB-MC model) could be fitted with the Equation 5.3 and Equation 5.4 and are qualitatively in agreement with experimental data[31, 50, 51, 158]. More specifically, the ΔECM in Figure 5.3a and Figure 5.3c exhibits a sigmoidal response to the delivered dose, as showed by Defraene et al. [50, 51], with the highest values reached within the first 3-4

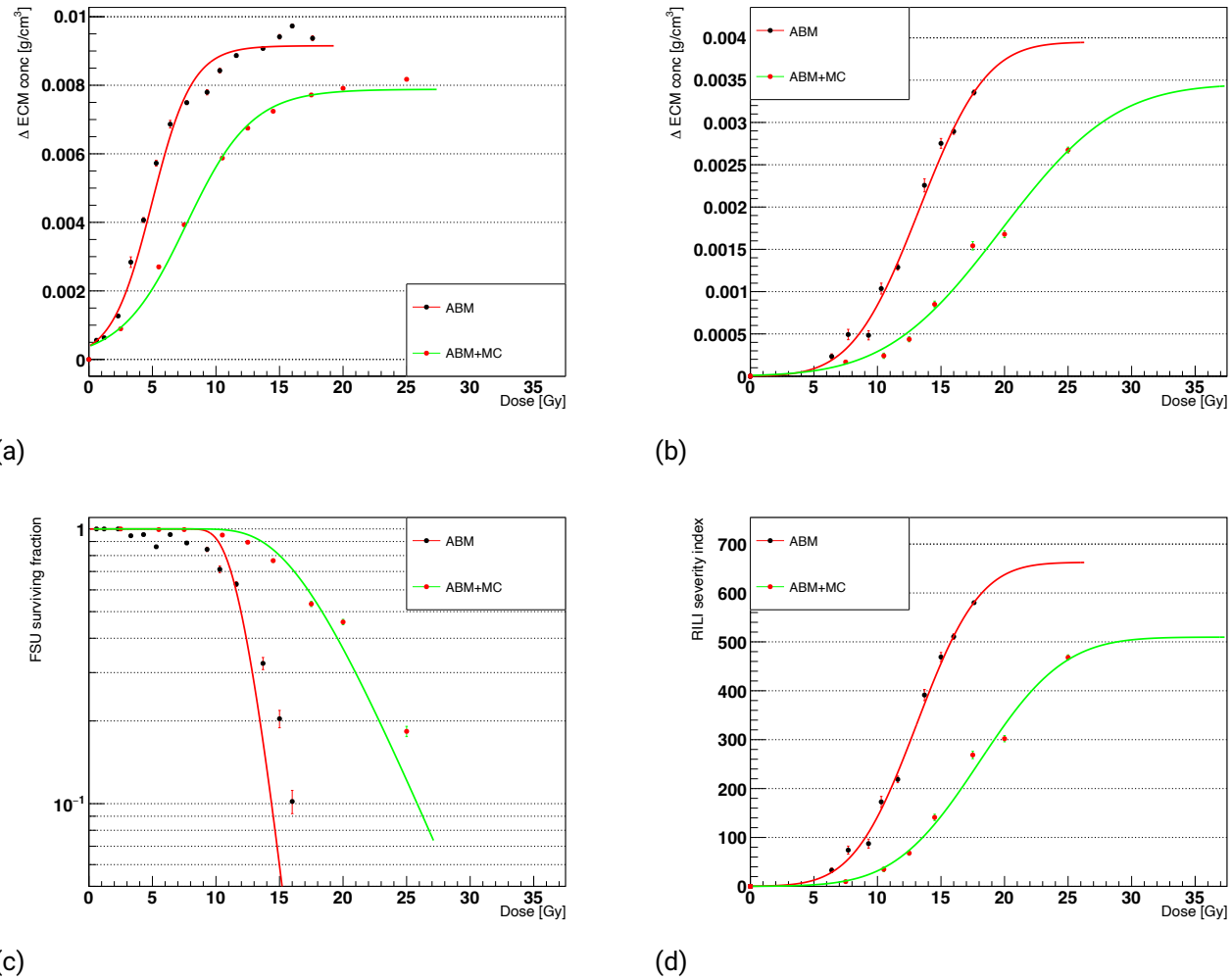

Figure 5.3: Comparison of the major outcomes from the ABM model (black markers, red fit curves) and the ABM-MC model using photons in one fraction (red markers, green fit curves). Panels **a** and **b** show the increase in the average ECM concentration across the whole simulation space after 90 days (early component) and 1200 days (late component). In panel **c** the surviving fraction of the alveoli (FSU) in logarithmic scale at the end of the simulation is reported. In the panels **a**, **b** and **c** the error bars represent the Standard Error of the Mean (SEM) for 10 experiments. The late ΔECM and the FSU survival are combined to provide the RSI, outlined in panel **d**,), where the errors bars were obtained by propagating the error from the FSU survival and the ΔECM increase measurements.

months following the irradiation, as in Konkol et al. [31].As expected, the ΔECM increases as a function of the dose and reaches a plateau around 20Gy for the early component and 30Gy for the late component. Due to the higher fraction of mesenchymal cells in the inflammatory phase (i.e. before the macrophages are able to clean the senescent cells), the ΔECM_{max} of the early phase is more than twice as much as that in the late phase and the plateau is reached at lower doses as the total amount of ECM that can be stored in the alveolar space is limited.

Figure 5.3c shows the surviving fraction of the FSUs as a function of the dose. For doses equal to or

Dose per fraction (Gy)	0.5	1.1	1.5	2	4	5	6	7	8.5
Total dose (Gy)	2.5	5.5	7.5	10	20	25	30	35	42.5

Table 5.1: Doses per fraction and corresponding total doses delivered in 5 fractions to gauge the ability of the model to simulate normal tissue sparing effects.

smaller than 7.5Gy in the AB-MC model the survival is close to 100%, which implies that no alveolus is fully depleted from the healthy AEC2, neither directly or indirectly. Moreover, fitting of the dataset with the Equation 5.5 shows better agreement than that observed for the results from the ABM model alone as well as improved consistency at the lower doses.

Finally, the late component ΔECM and the FSU surviving fraction were combined into the RSI, a surrogate measure of the RILF severity, presented in Figure 5.3d. The dataset obtained from the AB-MC model could be fitted using Equation 5.4 and showed qualitative agreement with experimental findings about the FI from Zhou et al. [158], although the RSI saturates at higher values than the FI.

Overall, the outcomes from the AB-MC model are qualitatively in agreement with experimental results found in the literature. However, a quantitative assessment couldn't be achieved, mainly because of the nature of the FI and ΔECM, originally expressed in terms of quantities that can't be discerned from our model (such as the functioning volume and the variation in the radiodensity). Notably, our previous model showed increased damage (i.e. lower surviving fractions and higher ΔECM) at the same doses, likely caused by narrower and more peaked dose distributions.

5.2.3 Temporal fractionation

To assess the ability of the alveolar segment model to repair the damaged tissue in between irradiations, we implemented a 5-fraction scheme using the AB-MC model. The temporal fractionation involved the delivery of relatively small doses (see Table 5.1) 24 hours apart, thus allowing the M1 and M2 macrophages to gather (triggered by the secretion of MCP1 by the damaged AEC2) and start removing the senescent cells. Moreover, the healthy AEC2 could replenish the depleted alveoli. After a 1-day simulation, the system was "frozen" and the structure of the alveolar segment loaded into TOPAS-nBio for the following irradiation.

The number of fractions and the doses were matched to those used in the experiments presented in the work by Zhou et al[158], which was used to evaluate our previous ABM model.

Figure 5.4 presents a comparison of the main outcomes from the AB-MC model, using 1 and 5 fractions, as a function of the total delivered dose. The results were fitted using Equation 5.3 and Equation 5.4. As expected, a right shift in both the late component ΔECM and in the FSU survival was observed. Consequently, an isoeffect was measured at higher total doses for the RSI when using 5 fractions with respect to 1 fraction. Similar RSI values for the two fractionation schemes were measured for total doses equal to or lower than 10Gy and above 35Gy, due to the high variability in the FSU survival at low doses and the formulation of the RSI, that forces it to saturate at high doses. Of note, the FSU survival data for the single fraction deviated from the LQ fit at high doses ($\geq$ 30Gy).

The results for the early and late ΔECM from our AB-MC model with 5 fractions could not only could be fitted using the equations provided by previous experimental studies by Defraene et al. [50, 51] and Konkol et al.[31], but also matched the observations from Zhou et al.[158] regarding the right shift of the RSI (a surrogate of the severity of the RILF, as is the FI) as the number of fractions increased from 1 to 5.

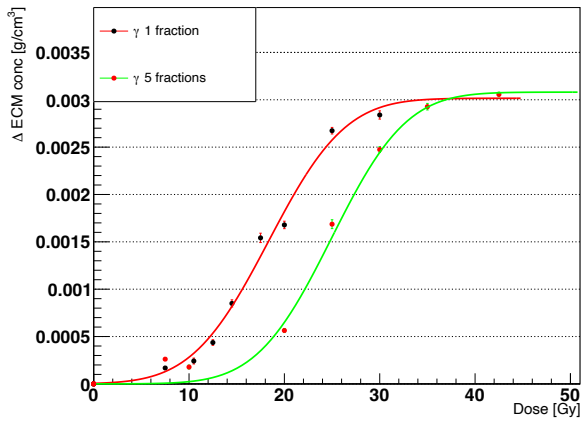

(a)

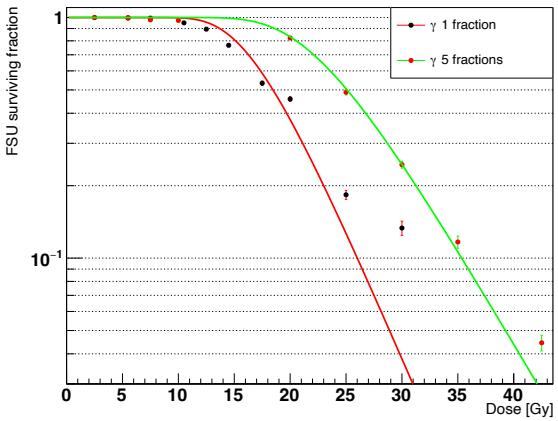

(b)

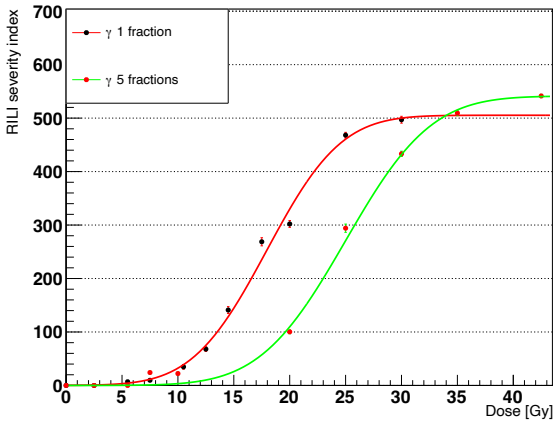

(c)

Figure 5.4: Comparison of the major outcomes from the ABM-MC model using photons in 1 fraction (black markers, red fit curves) and 5 fractions (red markers, green fit curves). Panels **a**, **b** and **c** show the increase in the average ECM concentration (late component), the surviving fraction of the FSU and the RSI, respectively, at the end of the simulation. The errors bars in panels **a** and **b** are the SEM for 10 experiments, while those in the panel **c** were obtained by propagating the errors in the RSI definition.

Impact of the bystander threshold

The bystander threshold dictates the minimum number of senescent AEC2 necessary to damage an healthy AEC2 that is located in their neighbourhood. It is, therefore, the main regulator for controlling the speed of the spread of the indirect damage. In fact, the probability that an healthy AEC2 will be indirectly damaged depends on the time spent in the neighbourhood of senescent cells and this, in turn, increases only if the number of senescent neighbours exceeds the bystander threshold (as introduced in the work by McMahon et al.[74]).

In our previous work[81], we determined the optimal values for the phagocytic fraction and phagocytic index, i.e. 100% and 1. Moreover, we showed how different values of the apoptotic-to-senescent ratio

affected the survival of the FSUs. We assessed the best value for the bystander threshold as well (i.e. 2), but given that the results from the AB-MC model exhibited decreased damage for the same doses with respect to our previous model, we evaluated the impact of a faster spread of the indirect damage (by setting the bystander threshold to 1) to determine if the effects could offset each other. As can be seen from

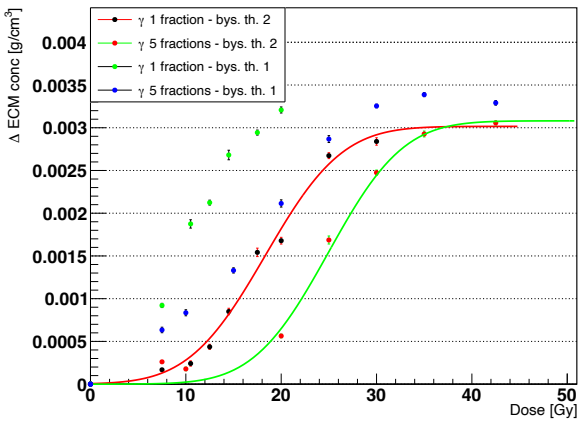

(a)

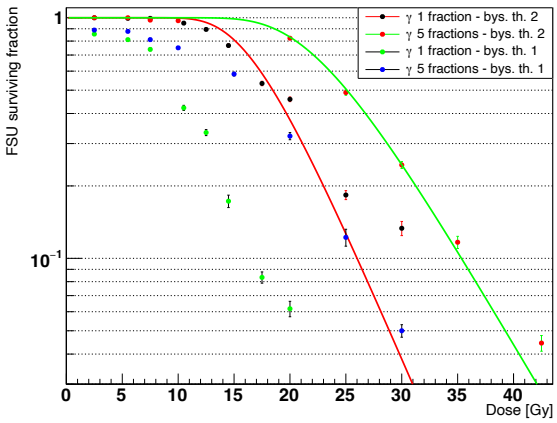

(b)

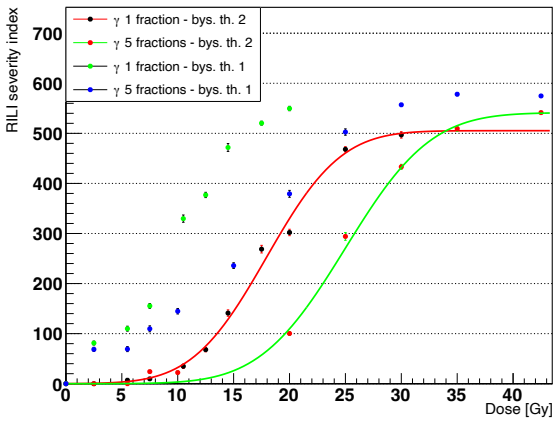

(c)

Figure 5.5: Comparison of the major outcomes from the ABM-MC model using photons in 1 fraction (black markers, red fit curves) and 5 fractions (red markers, green fit curves) with bystander threshold = 2, 1 fraction (green markers) and 5 fractions (blue markers) with bystander threshold = 1. Panels **a**, **b** and **c** show the increase in the average ECM concentration (late component), the surviving fraction of the FSU and the RSI, respectively, at the end of the simulation.The errors bars in panels **a** and **b** are the SEM for 10 experiments, while those in the panel **c** were obtained by propagating the errors in the RSI definition.

Figure 5.5, even though the AB-MC model showed reduced damage with respect to the ABM, one, it could not compensate the increased spread of the indirect damage. In fact, lowering the bystander threshold led to FSU survivals $< 100\%$ and $\Delta ECM > 0$ even at very low doses. As a consequence, the lowest RSI did not drop below 60 and none of the major outcomes could be fitted using Equation 5.4 and Equation 5.5.

5.2.4 Radiation qualities

The use of charged particles in the clinical setting has seen rapid spread in recent times due to the increased conformality of the dose deposition to the target volume with respect to the photons[201]. Moreover, experimental studies[54] reported differences in the dynamics of the normal tissue response between lung cancer patients treated with photons and protons. Contextually, we used TOPAS-nBio, coupled to our ABM, to compare the effect of different radiation qualities on the alveolar segment. In particular, we simulated the irradiation of the lung structure with 2 million protons delivered with an external beam using 4 coplanar fields in one fraction.

TOPAS-nBio can generate standard DNA damage files for each cell that is hit by one or more particles, thus providing punctual information about each and every interaction between the particle and the DNA. However, the process on a common laptop is relatively slow and the amount of data that is stored for each cell can be very large, thus making it prohibitive for thousands of cells as those in the alveolar segment. Therefore, our simulations didn't take into account the differences in the patterns generated by photons and protons when damaging the DNA of the AEC2 cells. Different simulation outcomes are thus solely the result of different dose distributions.

We simulated 60MeV protons as previous studies have reported negligible differences in the DNA damage response between proton and photon irradiations in the plateau region for this energy[202] and very low linear energy transfer (LET, < 2.5 keV/μm) at short distances (< 5mm)[203]. This requirement ensured very small LET variations along the proton tracks (as the diameter of the alveolar segment is < 1mm) and allowed us to use the LQ parameters derived from the survival curve of the AEC2 irradiated with photons. Figure 5.6 shows the dose distribution for the protons expressed as a fraction of the maximum delivered

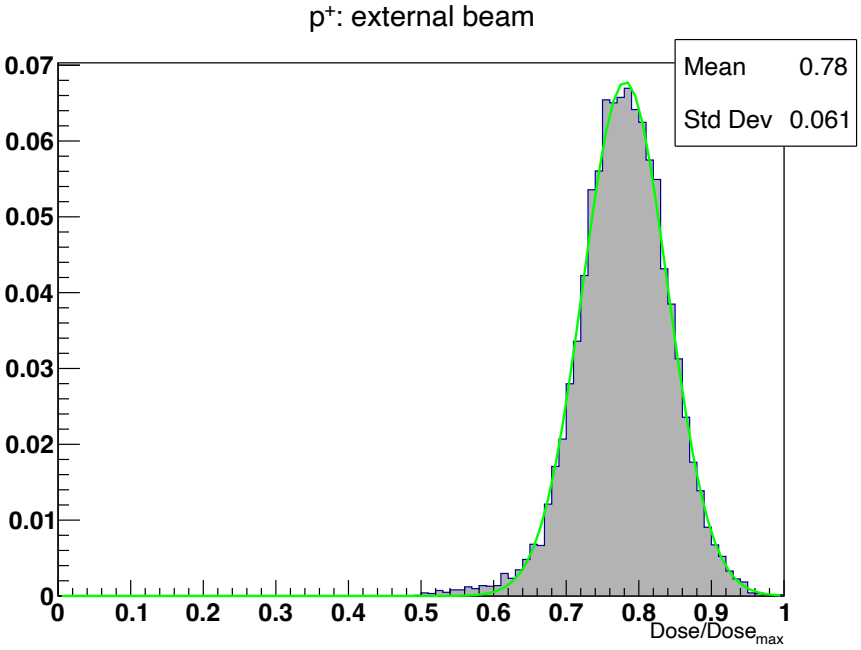

Figure 5.6: Dose distribution histogram for the alveolar segment model irradiated with protons. The dose was delivered using 4 fields from an external beam and 2 million histories in total. On the x-axis, doses are shown as percentages of the maximum delivered dose and the green curve is the best Gaussian fit for the histogram data.

dose. When compared with the photons histograms in Figure 5.2, the protons distribution exhibits a more

pronounced and narrower peak and the data points align well with a Gaussian distribution.

When comparing the main simulation outcomes from the different radiation qualities, a marked shift towards lower doses for the same effect (i.e. same ΔECM and FSU surviving fraction), shown in Figure 5.7, was observed for the protons. This, in turn, resulted in higher RSI at the same dose, similar to what was found when comparing different fractionation schemes for the photons (see Figure 5.4).

Given that the FSU survivals could be fitted by the LQ model from Equation 5.5 for both the photons and the protons, we introduced a relative biological effectiveness[204] relative to the FSU survival (RBE_{FSU}). The RBE_{FSU} was defined as the ratio of the absorbed dose from the photons to the absorbed dose from the protons resulting in the same effect and provides a quantitative measure of the relative effectiveness of the different radiations in depleting the FSUs. The definition reads as follows:

$$RBE_{FSU} = \left.\frac{D_\gamma}{D_{p^+}}\right|_{sf\gamma=sfp^+} \tag{5.1}$$

As can be seen from Figure 5.7b, small variations were observed for the RBE_{FSU} at the 3 isoeffects considered. While it is generally assumed an RBE = 1.1 for protons relative to photons for identical cell survivals[205], with lower RBEs for higher reference doses, we measured increasing values for identical FSU survivals: 1.30, 1.31 and 1.34 for 50%, 37% and 10% survival, respectively. However, it is worth noting that for high doses the data points for the photons deviate from the LQ fit and therefore the RBE_{FSU} at 10% survival might not be representative of the actual relative effectiveness of the radiation in depleting the FSUs. Moreover, it should be emphasized that the RBE_{FSU} is not an RBE in the traditional sense, as it's defined in terms of the survival of the FSUs and reflects heterogeneities in the dose distribution at a scale that would hold little relevance in a clinical setting.

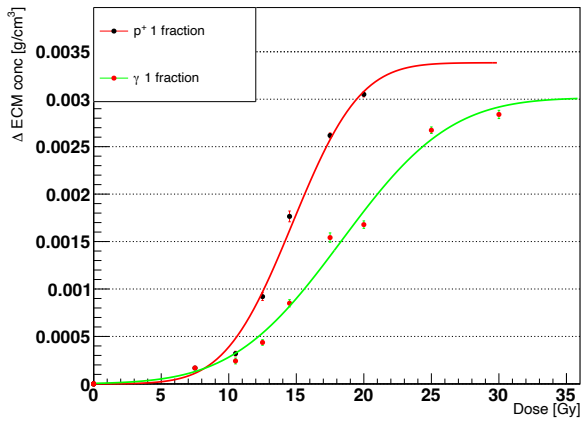

(a)

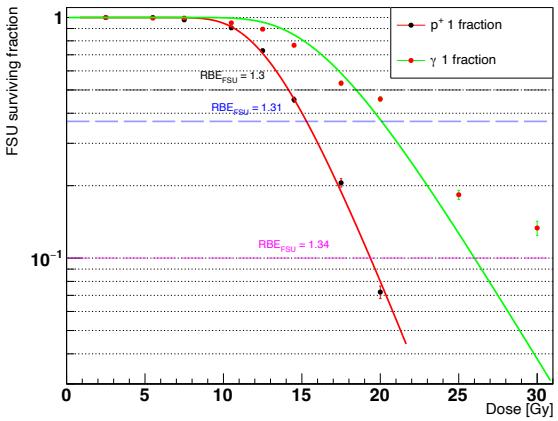

(b)

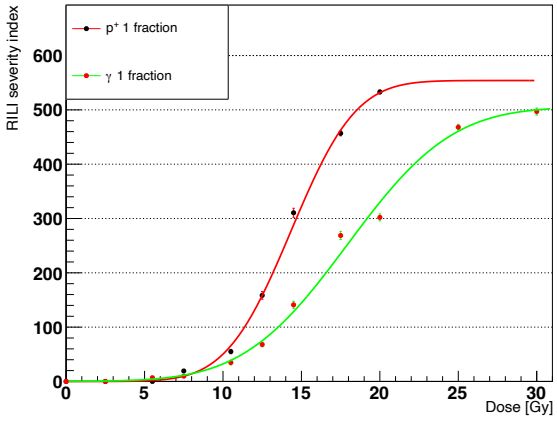

(c)

Figure 5.7: Comparison of the major outcomes from the ABM-MC model using protons (black markers, red fit curves) and photons (red markers, green fit curves), both in 1 fraction. Panels **a**, **b** and **c** show the increase in the average ECM concentration (late component), the surviving fraction of the FSU and the RSI, respectively, at the end of the simulation. Panel **c** provides also the RBE values for the surviving fraction of the FSUs at 50%, 37% and 10% survival. The errors bars in panels **a** and **b** are the SEM for 10 experiments, while those in the panel **c** were obtained by propagating the errors in the RSI definition.

5.3 Discussion

Despite being a crucial component in a large variety of cancer treatments, the efficacy of RT is intrinsically hindered by normal tissue toxicities[60]. Increasingly sophisticated NTCP models[75] have been implemented to estimate risk probabilities from patients' DVH, but the lack of mechanistic information constrains superficial representations of the underlying mechanisms and prevents patients-specific parameters to be taken into account.

To address the aforementioned shortcomings, we have previously implemented an ABM that simulates

the onset of RILF in an alveolar segment[81]. In this work, we outlined the development of a coupled AB-MC model, where the alveolar segment structure was rebuilt using TOPAS-nBio[6] and linked to an updated version of our previous model, with a custom script in charge of handling the communication between the models. As discussed in our former work, the ability of the model to replicate experimental results was assessed via the FSU (i.e. the alveoli) survival, the ECM increase and the RSI as functions of the dose and the output datasets fitted using Equation 5.4 and Equation 5.5.

More specifically, in the new implementation the ABM is used to generate the initial structure in healthy conditions and afterwards the cells' position, type and size are exported. Using this data as an input, the MC tool builds the structure in real-time and an irradiation is simulated based on the information provided via the parameter control system. Accordingly, realistic dose distributions can be simulated and dose depositions at cell scale registered. The generated data are then sent back into the ABM, where the absorbed doses are used to determine the fate of each cell using the LQ model. Subsequently, the ABM, is run and the onset of RILF simulated. Finally, to replicate temporal fractionation schemes the workflow can be executed multiple times by setting the number of fractions in the control script.

We compared different setups of the photons' source by characterizing the resulting relative dose distributions in the alveolar segment. To maximize the dose homogeneity, the tested sources were either isotropic, located at the center of the simulated structure, or external, with 4 coplanar fields spaced 90 degrees apart. While the first setup resulted in a positive-skewed distribution with 2 peaks in the low-dose region and a long right tail, the one provided by the external beam was symmetric and peaked at 50% of the maximum dose. Moreover, Figure 5.2c shows that an increase in the number of histories from 4 to 30 millions didn't alter the dose distribution significantly. In light of these results, the external beam was selected as the default photon source for the following simulations.

In accordance with the results from our previous model, the outcomes of the ABMC approach (single fraction) qualitatively matched published experimental results. In particular, the ΔECM showed two distinct components, an early one at around 3 months from the irradiation and a late one as the model reached the steady state[53]. Both the datasets exhibited a sigmoidal response as the dose increased and could be fitted using Equation 5.3 and Equation 5.4. The surviving fraction of the FSUs was measured at the end of each simulation as the ratio of the number of alveoli with at least an healthy stem cell to the initial number of alveoli, expanding upon the idea introduced in the critical volume NTCP model[69, 72]. The results were fitted using Equation 5.5 and showed good agreement with the LQ model for doses $<$ 20Gy. Finally, the previous metrics were combined into the RSI, which mimics the FI introduced by Zhou et al.[158] and provides a surrogate measure of the RILF severity, which could be fitted using Equation 5.4. Overall, the AB-MC model preserved the ability to simulate existing experimental results, such as the sigmoidal response of the early and late components of the ΔECM to increasing doses, as observed by Defraene et al. [50, 51], as well as their temporal patterns, outlined by Konkol et al. [31] and Bernchou et al.[53].Of note, despite showing consistency with the previous ABM, it can be seen from Figure 5.3 that all the curves were shifted towards higher doses for the same outcomes. We attribute these differences to the shape of the newly generated dose distributions which peak on the mean lung dose, but span a relatively large range with respect to those in the ABM. Moreover, in the old model the delivered dose was used to determine the initial damaged fraction which was the same for all the cells in an alveolus. Conversely, the ABMC simulates an actual dose distribution using the TOPAS-nBio module and each cell, given the absorbed dose, has a certain probability to be damaged, in accordance with the LQ model.

Temporal fractionation schemes as a way to spare the normal tissue as sublethal damages are repaired and depleted areas repopulated are widely employed in the clinics[197, 198, 199]. Accordingly, we compared the results from 1-fraction with those from 5-fractions using the AB-MC model. The ABM was run for 1 day between fractions and the structure's data at the end of the simulation used to feed the MC model. After the 5th fraction, the ABM ran for 1200 days to match the simulation time from the 1-fraction

simulation. As expected, the outcomes in Figure 5.4 show a shift towards higher total doses for the alveolar segment irradiated with 5 fractions and could be fitted using Equation 5.4 and Equation 5.5 for the ΔECM and RSI. Notably, the transition of the RSI transition to higher total doses from 1 to 5 fractions mimics the findings from[158] for the photons, although the experiments were performed on mice. The model is thus able to replicate normal tissue sparing as the macrophages clean the senescent cells and prevent excessive spread of the damage via bystander mechanisms, and the AEC2 repopulate the depleted alveoli. It is worth noting that the actual DNA damage is not taken into account by our model and therefore the repair of sublethal damages was not simulated. However, it was recently shown in [206] that residual DSBs in normal tissue cells exhibit low predictive power for cell survival and thus our assumptions remain valid. Finally, we noticed that delivering the dose in 5 fractions improved the ability of the LQ model to fit the FSUs survival with respect to the single fraction, especially for high total doses.

The key role played by the bystander effect in the onset of RILF has been emphasized by multiple studies[32, 147, 148] and earlier works highlighted that, when radiation-induced lung toxicities are modelled mechanistically, inflammation-induced tissue damage should be taken into account[77]. In our previous work we detailed the implementation of the damage spread behavior for the senescent AEC2 agents, where the minimum number of senescent AEC2 needed to damage an healthy cell can be controlled via the bystander threshold parameter. Given that the AB-MC model showed lower damage for the same dose with respect to our previous model, we investigated the effect of an increase in the speed of the damage spread on the model outcomes by lowering the bystander threshold. Figure 5.5a and Figure 5.5b show that the reduced damage can't compensate for the increase in the bystander effect and, even at the lowest doses, the ΔECM didn't drop to 0 and the FSU survival was $< 100\%$. This, in turn, resulted in a higher RSI with respect to that measured with the bystander threshold $= 2$. Notwithstanding this, the model proved to be robust, as it retained the ability to recover in-between fractions, as demonstrated by the right shift towards higher total doses when a 5-fraction scheme was used.

To further characterize the AB-MC model, we simulated a monoenergetic 60MeV proton irradiation using the same setup for the source as that previously described for the photons. Remarkable differences with respect to the photons irradiation were found in the resulting dose distribution (see Figure 5.6), which exhibited a narrower peak at 80% of the maximum delivered dose. As a result, despite the DNA damage and repair mechanisms were not taken into account, the model outcomes differed significantly from those obtained when the alveolar segment was irradiated with photons using a single fraction. Figure 5.7 shows increased ΔECM and lower FSU survival for the same doses when protons were used, resulting in a higher RSI for doses $>$ 10Gy and similarly to what Zhou et al.[207] observed when mice were irradiated using high LET particles. Furthermore, we compared the ability of the different radiation qualities to deplete the alveoli from the AEC2 by computing the RBE at different FSU survivals (that thus differs from the traditional RBE), a metric that accounts for long term effects as it was computed when the model reached the steady state and the alveolar segment was thus allowed to recover. We measured an average RBE_{FSU} $= 1.32$, however, the FSU survival at high doses for the photons deviated substantially from the LQ fit and thus the value at 10% survival might be discarded. Given that for the organs with parallel architecture, such as the lungs, the FSU survival plays a key role when estimating the probability of radiation-induced toxicity, future studies could benefit from the RBE_{FSU} as a tool for the comparison of different radiation qualities on the NTCP. This notwithstanding, it's crucial to acknowledge that the use of 1 keV photons for the irradiation of the alveolar segment has resulted in highly heterogeneous dose distributions. This, in turn, could be the underlying reason for the RBE effects observed in this study, which may not be seen in real exposures.

Overall, these findings capture the unique feature of the model (and, more generally, the added value ABMs can bring to the field of radiation oncology) to be susceptible not only to variations in the average values (i.e. different average doses, as equation-based models would be), but also to local changes (i.e.

different dose distributions).

In conclusion, this work could serve as a framework to investigate the effect of different fractionation schemes and dose distributions on the severity of RILF, while taking into account individualised parameters in the perspective of advancing precision medicine in RT treatments. Future developments might concentrate on taking into account the DNA damage and repair mechanisms in order to estimate the fractions of healthy, apoptotic and senescent cells more accurately.

5.4 Materials and Methods

5.4.1 The Agent-Based Model

Our 3D ABM of RILF in an alveolar segment was developed using the open-source platform BDM[4] and its implementation was detailed in our previous works[81, 82].

The model replicates a small section of the distal airways in the human lungs, namely an alveolar segment, where three layers of alveoli are stacked in a cylindrical shape. Each layer includes 6 alveoli which are modelled as hollow spheres. The surface of each sphere, in turn, is lined by 3 main cell types: the mesenchymal cells (fibroblasts and myofibroblasts) in the outer layer, the macrophages (type 1 and 2, M1 and M2) in the inner layer and the epithelial cells (type 1 and 2) in the middle layer. Following a radiation-induced damage in the epithelial layer, type 2 alveolar epithelial cells (AEC2s) can either become apoptotic or turn into a damaged and eventually senescent state. By secreting a plethora of chemokines and cytokines[151], the senescent cells can both damage the surrounding healthy AEC2 (where the minimum number of senescent cells needed to damage an healthy one is regulated by the bystander threshold parameter) and trigger an immune response led by M1 and M2. Provided by the capillaries (which are not simulated by our model), M1 and M2 (whose phagocytic fraction and phagocytic index are set with custom parameters) are gathered in the alveoli and remove the senescent cells[157, 184]. At the same time, the healthy AEC2 increase their proliferation and differentiation rates in the attempt to replenish both their own and the AEC1 populations[187, 188]. Ultimately, the disruption of the healthy epithelium and the secretion of growth factors from the type 2 macrophages concurrently stimulate the expansion of the mesenchymal compartment which in turn saturates the alveolus with ECM components. The severity of the damage at later time points (e.g. months/years after the treatment) is measured via the RSI, whose definition (proposed in our previous work[81]) was inspired by the concept of FSU in the critical volume model of NTCP[69, 72] and by the FI introduced in the work of Zhou et al.[158]. The RSI reads as follows:

$$RSI = \sqrt{\Delta\overline{ECM_{conc}}\uparrow \cdot \Delta V_{surv,FSU}\downarrow} \tag{5.2}$$

Where the two factors describe the average increase in the concentration of the ECM across the whole simulation space and the decrease in the volume of surviving FSUs, represented by the alveoli. Other equations of note (which were described in more detail in our previous work and were used to fit the simulations' output in section Results) are the following:

- Increase in the average ECM concentration across the whole simulation space, early component (where ΔECM_{max}, γ and D_{50} represent the saturation value for the ECM increase, the steepness of the sigmoid and dose at 50% of the ΔECM_{max}, respectively)[31, 50, 51].

$$\Delta ECM = \frac{\Delta ECM_{max}}{1 + e^{4\cdot\gamma\cdot\left(1-\frac{D}{D_{50}}\right)}} \tag{5.3}$$

- Increase in the average ECM concentration across the whole simulation space, late component, and RSI[158]

$$\begin{matrix} \Delta ECM \\ RSI \end{matrix} = \frac{1}{2} \cdot A \cdot \left\{ 1 - erf\left(\sqrt{\pi} \cdot \gamma \cdot \left(1 - \frac{D}{ED_{50}} \right) \right) \right\} \tag{5.4}$$

- FSU survival probability, derived from the LQ[10] and critical volume NTCP models[69, 72] (where N_{AEC2} is the total number of healthy AEC2 in an alveolus in homeostatic conditions)

$$P_{surv,FSU} = 1 - P_{kill,FSU} = 1 - \prod_{i=1}^{N_{AEC2}} P_{kill,cell} = 1 - \left(P_{kill,cell}\right)^{N_{AEC2}} = 1 - \left(1 - e^{-\alpha D - \beta D^2}\right)^{N_{AEC2}} \tag{5.5}$$

With respect to the previous version, the current model brings with it new features and noteworthy changes that will be detailed in what follows. Among them, modelling of the apoptotic AEC2s has been implemented to increase the accuracy of the simulations. Once an AEC2 has changed its state to apoptotic (either due to irradiation damage or ageing), free movement is hampered and the time to removal from the simulation is drawn from a Poisson distribution[208].

It is worth emphasizing that weakening of the immune system due to radiation-induced damage is not simulated by our model. In fact, to avoid additional complexity and potential uncertainty in the parameters, it is assumed that only the AEC2 cells can be damaged by the radiation, while all the other cell populations, including M1 and M2, are left unaffected. However, by tuning the aforementioned parameters that regulate the phagocytic fraction (i.e. the fraction of macrophages that can phagocyte senescent cells) and index (i.e. the maximum number of senescent cells that can be phagocyted by a macrophage) the damage to the immune system could be easily implemented.

At the beginning of a new simulation, each alveolus is initialized with the three cell compartments described before. Cells (i.e. the agents) are distributed at random positions on the alveolar surface and assigned type-specific behaviours. Among them, cell migration plays an important role and has been optimized in our latest model (see our previous work for additional details[81]). Macrophages and mesenchymal cells travel along spherical arcs in random directions to patrol the alveolar space and maintain homeostatic ECM concentrations, respectively. AEC1 and AEC2, however, are capable of neighbourhood-informed migration and thus move preferentially towards depleted zones in order to repopulate them. Finally, damaged and senescent epithelial cells move in random directions at slower speed than the healthy ones, but might not be able to move at all at times. In our updated model, every cell movement is followed by a check on the cell's final position. If the cell doesn't happen to be located on the spherical surface it belongs to (mainly due to approximation errors when the spherical arc is computed), the cell is translated to the appropriate radial distance while keeping the polar and azimuthal angles fixed.

As in our previous model, the simulations run in a closed cubic space of side 2000 μm that encompasses the whole alveolar segment. A diffusion grid overlaps the simulation space and dissects it in smaller cubic voxels, whose number can be adjusted by the user. The simulated cells can both measure and change the concentration of the substances of the voxel they are located in. Once secreted, substances can both diffuse and decay and, in some cases, be depleted by other substances. Our model simulates, among others, such coupled substances, i.e. MMP, TIMP and ECM (interaction mechanisms are outlined in our previous works[81, 82]). The system of reaction-diffusion PDEs for all the involved substances is then solved using a FTCS method with user-defined BCs. In its updated version, both the binding coefficients, the target and the BCs for the substances in the model can be specified in the initialization phase. In particular, we set Neumann BCs (as opposed to our previous model) with constant value, to ensure a net zero flux and mimic inter-compartmental communication. Moreover, we increased the duration of one time-step for the solution of the system of PDEs in the diffusion grid to 20 seconds. By doing so, we could shorten simulation

times while still fulfilling both the stability (i.e. CFL) and positivity conditions. The model simulates the diffusion, decay and, in some instances, the depletion of 10 different substances. These extracellular substances altogether constitute a network that serves as an interface between the cell populations[81, 82] which, for instance, senescent AEC2 can use to gather the monocytes and M2 to increase the proliferation of the mesenchymal cells as well as regulate the concentration of the ECM. Although simulating such a number of extracellular substances doesn't come without disadvantages (such as a decrease in the model's performance), it provides a more accurate representation of the mechanisms that underlie the RILF and allows the users to test the outcomes of new therapies by adjusting the model's parameters.

5.4.2 The Monte-Carlo Model

TOPAS-nBio is built on top of the Geant4-DNA[209] toolkit and extends the functionalities of the TOPAS platform[210]. It allows MC simulations at the microscopic and nanoscopic scale while simplifying the modelling of biological structures as well as consistent measurements of radiobiological quantities.

To investigate the effect of realistic dose distributions on our model of alveolar segment, we reimplemented its structure from scratch using the TOPAS-nBio platform. Our extension consists of 3 new classes that are used to both build the geometry of the cylinder and score the dose delivered to its building blocks.

When a new simulation is performed, an envelope for the alveolar segment is firstly built as a cubic box with side 900 μm. A for loop runs then through a vector containing the centers of the 18 alveoli (whose positions can be either hardcoded or provided in a separate file) and smaller containment boxes are generated. The modelling proceeds by instantiating a generic spherical structure with temporary radius for the cells and a second for loop runs through all the alveoli positions. Within its body, the alveoli are built by placing the cells on three spherical surfaces (as described in the previous section). More specifically, parameters for each cell (i.e. position in 3D, colour that indicates the cell type and size) are loaded from external files and, given the inherent repetitive nature of the geometry, the parameterization technique[210] is used to allow for faster rendering and simulation times (see Figure 5.8). As opposed to those in the ABM, cells in this model don't have behaviours, are static and differ only by colour and size.

Hits within cells are processed using a custom scorer that provides both the total dose deposited within the cells as well as the average dose for each alveolus. By checking the cells' size, non-epithelial cells are filtered out and the computation of the dose is skipped. For the epithelial cells, however, the total energy deposited by the hitting particles is summed and converted to Gray (Gy) units. At the end of a simulation the total dose delivered to each cell is exported to a text file along with a unique identifier and the identifier of the alveolus the cell belongs to. Moreover, the average dose delivered to (the epithelial cells of) each alveolus is computed and exported together with the alveolus identifier to a second file. Given that our previous work identified the alveoli as the FSU of the lung, the latter can be useful to, for example, characterise the dose distribution on a bigger scale than the cellular one.

Finally, simulations can be run using the parameter control system as described in the work by Schuemann et al.[6]. In the parameter file, the total world volume is defined as a cubic box with the same size as the simulation space of the ABM. The alveolar duct is then placed at its center and the envelope material set to vacuum, while we assumed that water is the sole component for the cells. With regard to the particle sources, we tested both an isotropic source located at the center of the alveolar duct and an external beam with one to four coplanar fields (see Figure 5.9). Following the measurements of the average delivered dose per alveolus and outlined in the section Results, the homogeneity of the dose distribution was maximized by the external beam with four fields. The motion of the beam was implemented by using a step function with variable positions on the XZ plane and 90 degrees rotations about the Y-axis, while the cut-off shape was set to "rectangle". Energy and type of the particles to be included in the beam were also set via the parameter file as well as the angular and energetic spreads which were set to zero. Settings for our custom

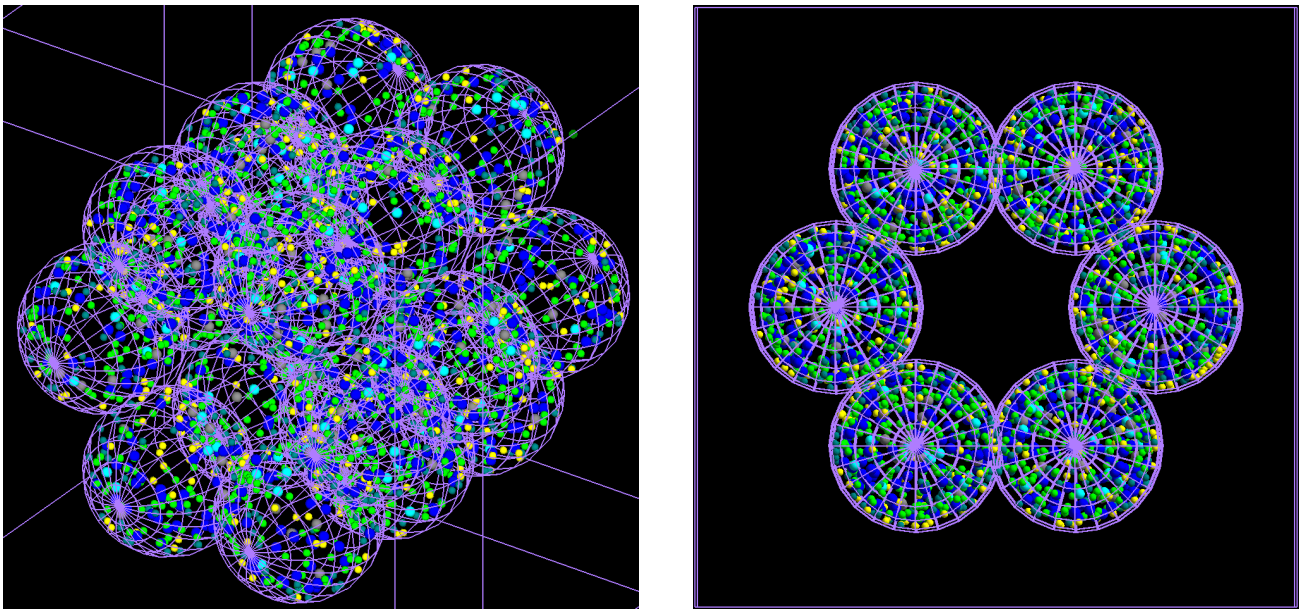

(a) (b)

Figure 5.8: Alveolar segment model built with TOPAS-nBio. The 18-alveoli structure is inscribed in a cubic box, while each alveolus has a spherical envelope. Cells have spherical shape and differ by size and colour. The outer space is empty, while cells are filled with water. The side of the outer box is 900 μm long, while the diameter of each alveolus measures 260 μm.

scorer were also adjusted via the parameter control system.

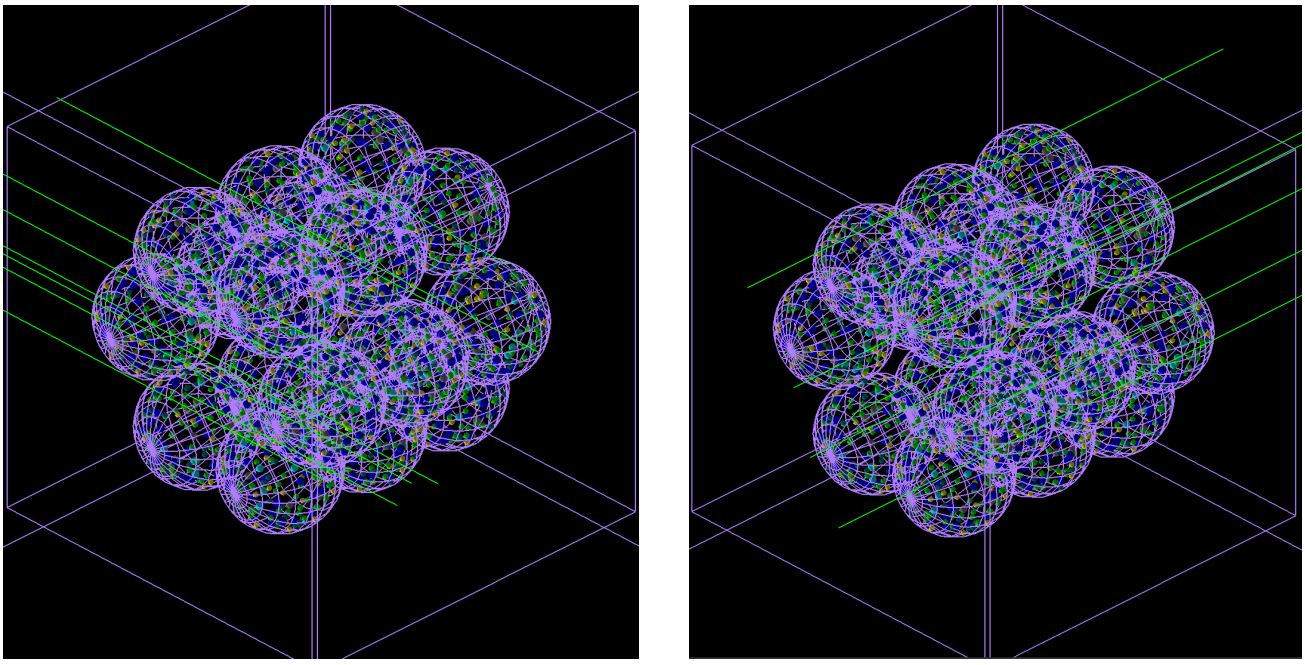

(a) (b)

Figure 5.9: Frontal and lateral irradiation of the alveolar duct in TOPAS-nBio with 1 keV gamma particles.

5.4.3 Coupling the models

The coupled model consists of the aforementioned AB and MC models each equipped with import/export functionalities that allow data exchange. In addition to this, overall control of the workflow is assigned to a bash script (see Figure 5.10). The sequence starts with a 1000 steps long run of the ABM that does not require any external data to generate the alveolar segment structure in healthy conditions. We tuned our ABM by running 20 days long simulations in homeostatic conditions and ensuring that both the number of cells and the average concentration of the substances remained constant and matched previously published results (more details on the tuning procedure as well as the parameters can be found in our previous work[81]). To ensure the consistency of the results, 10 experiments are performed for each parameter set and the output is used to feed the next step. In particular, we implemented a BDM standalone operation[4] that can be activated using a parameter and is triggered at the end of each simulation. With it, the cells' parameters together with the position and the diameter of the alveoli and the concentration per voxel of all the simulated substances can be exported. The data files for the cells contain the cells' position, their radius, an RGB colour code that identifies the type and additional type-specific parameters, such as the number of phagocyted cells for the macrophages or the number of steps spent above the bystander damage threshold for the healthy AEC2. Moreover, the identifier of the alveolus each cell belongs to is used to generate a new file for each alveolus.

Subsequently, the control script is used to set the total number of fractions as well as the steps for the ABM, the number of repeated experiments (where a new seed is selected for each run) and the target dose (through the number of histories of the MC model). The MC simulation is then run: TOPAS-nBio builds a new structure for the alveolar segment (using the data files mentioned above and the procedure described in the previous section), irradiates it and generates a summary of the dose deposited in each epithelial cell and the average dose per alveolus. It is worth noting that the duration of the irradiation is orders of magnitude shorter than the average cell's behavior time and therefore it is assumed that cells don't change their position and/or state within it.

The workflow proceeds with a new run of the ABM and custom parameters are used to enable reading of the external damage files. However, the concentration data are read in subsequent runs only as the duration of the preparatory simulation doesn't ensure steady state values for all the substances. Cells' data are read sequentially as well and used to rebuild the alveolar segment structure and assign the type-specific behaviours to the agents. For each epithelial cell the external damage file from the last step is checked and, if a match is found, the LQ model is used to determine the fate of the cell which will either remain healthy or become senescent or apoptotic. More specifically, a random number is drawn from a uniform distribution and compared against the AEC2 LQ survival curve value at the delivered dose (whose parameters were derived from previously published experimental data[165], as detailed in our previous works[81, 82]). A new simulation is then performed (whose duration is set in the bash script) and, depending on the number of fractions, the output is used to feed either a longer run of the ABM or a new irradiation using the MC model.

In terms of statistical sampling, all the simulations presented throughout this work were performed 10 times for each set of parameters, including the dose, the bystander threshold, the phagocytic fraction and index of the macrophages. To ensure independence between different runs, a new seed was selected in the control script at the beginning of each run and used to initialize the MC simulator. This resulted in different damage distributions that, in turn, led to variations among the initial conditions of the ABM. For the ABM a constant seed was set, however BioDynaMo compensated by automatically providing random number generators whose seed was linked to the identifier of the thread in use to simulate an agent, thus ensuring independence between and within runs. Each ABM simulation was run for 5.184.000 steps, resulting in a total simulation time of 1200 days (given the 20 seconds-long time steps). Additionally, 24 hours were

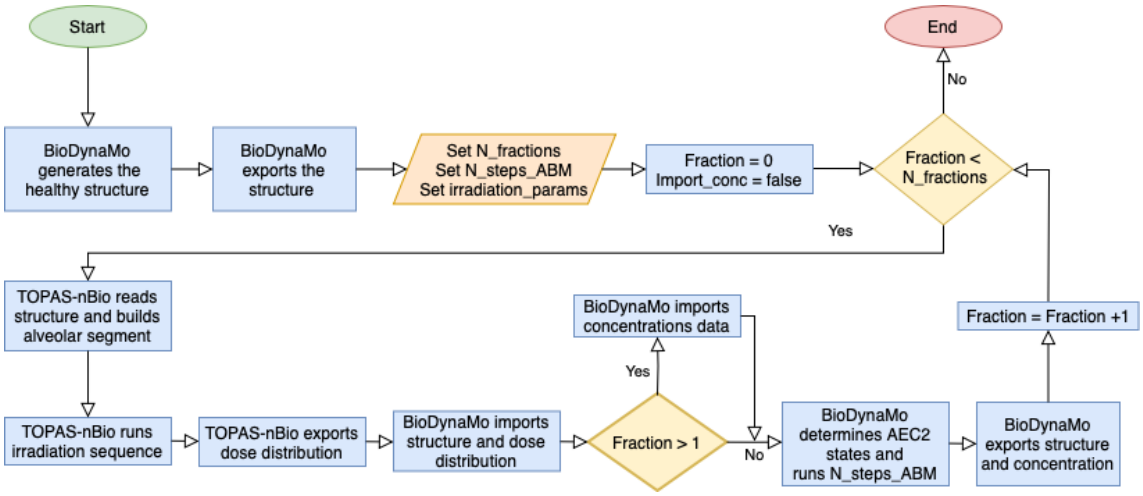

Figure 5.10: Flowchart of the coupled ABM – MC model workflow. BDM runs the ABM for 1000 steps, generates the healthy structure and exports the alveoli positions and the cells data. The number of fractions, the number of steps for the ABM and the irradiation parameters are then set into the control script which triggers the first run of the MC model using TOPAS-nBio. The structure is loaded from the data exported during the previous step and the alveolar segment is irradiated. Consequently, the dose distribution is exported and the data used as input for the ABM to determine the cells' fate. A new run of the ABM is then performed and the segment structure together with the cells' state and their position are exported. If a new fraction is to be delivered, the data are fed into the MC model, otherwise the workflow terminates.

simulated in the ABM between the delivery of each dose for the multi-fractionation schemes (thus adding 5 simulated days for the delivery of 5 fractions), while single fractions were assumed to be instantaneous.

A notable feature of our framework is its ease of use and customization. Besides BioDynaMo and TOPAS-nBio, users only need an executable file to simulate the ABM and text files that conform to the TOPAS Parameter Control System. As mentioned above, parameters such as the number of fractions, the number of time steps and dose per fraction as well as the number of experiments can be defined in the custom control script. If there's no need to update the agents' behaviours or the structure of the alveolar segment in the ABM, it's enough to compile the provided C++ code with BioDynaMo to generate the executable file. As for the TOPAS-nBio parameters that define, for example, the particle type and energy, the number of histories and the configuration of the particle source, they don't need to be compiled. Once provided the location of the aforementioned files, the control script can be executed from a shell to perform both the AB and the MC simulations sequentially. The simulations' output are ROOT[140] files that contain the number of cells and the concentration of each substance at multiple time points and location, stored for further analysis.

Preparatory simulations of the ABM used to generate the healthy structures, as well as those in between fractions, were run on a MacBook Pro laptop with a 2.3 GHz Quad-Core Intel Core i5 processor and 8 GB RAM. For longer (requiring more than 1 hour) or parallel simulations, however, a compute node of the Lichtenberg HPC system with 2x 2.3 GHz Intel Cascade-Lake AP 48-cores processor (96 total cores) and 384 GB RAM was used. Besides, the average runtime required to perform 1200-days long simulations was 3 hours. The reduced simulation times (enabled mainly by the optimizations made in the BDM framework[5] and the longer simulation steps) allowed us to perform longer simulations (with respect to our previous model, up to 1200 days) and improve the statistics by performing more experiments.

6 Summary and conclusions

An essential tool for cancer sterilization, RT is nowadays employed as a treatment for the majority of the affected patients [23, 211]. This not withstanding, the phenomenological nature of the models used to estimate the NTCP [75] leads to abstract and non-individual descriptions of the underlying radiobiology that hinder the efficacy of RT by limiting the maximum delivered dose and the irradiated volume. In this thesis, the potential benefits of a complementary approach, namely the ABM, were investigated and a 3D model of lung toxicity following irradiation (namely RILI) implemented and evaluated against existing experimental results.

Throughout the course of this work 3 models with increasing complexity were presented and all of them were implemented using the open source modelling platform BioDynaMo [4, 5]. Some contributions to the framework itself, mentioned in Chapter 2, were made to broaden its scope of application and address the RILI models' requirements. Among these contributions, a significant effort was made to enhance the capabilities of the diffusion module that is in charge of solving the PDEs that describe the diffusion of the extracellular substances. More specifically, both Dirichlet and Neumann BCs were implemented to simulate, for instance, insulated volumes or zero net fluxes across its walls and replace the existing open and closed boundaries. To handle the presence of multi-substance interactions, such as the depletion of the ECM by the MMP, the old FTCS resolution scheme was updated so as to take into account the depleting substances and the corresponding depletion coefficients. Moreover, the resolution scheme was made more robust by the introduction of two parameters checks that ensure the positivity of the substances concentration at each time step and position as well as the stability of the solution for the substances that undergo decay.

Although of lesser importance, it is worth mentioning that all the simulations performed for this work were run on multiple nodes of an HPC so as to improve their performance and allow parallelization. To do so, a custom script was written to install BioDynaMo in a container and testing on multiple cores confirmed the capability of the software to scale well up to 32 total cores. Due to the intrinsic stochastic nature of the AB models, the results differed slightly even between simulations run with the same set of initial parameters. Consequently, custom code was implemented to gather the results from different simulations and plot the average values of the number of cells and the concentration of the substances. As shown in Chapter 2, although not in use in the 3 models presented, several lung substructures with different levels of detail and complexity were built using BioDynaMo, thus assessing its multi-scale simulation capabilities.

To begin with, a 3D AB model of IPF, which shares a similar progression with RILF, was implemented and documented in Chapter 3. This hybrid model, which was used to check the suitability of the AB approach for modelling radiation-induced lung toxicity, consisted of a partial acinus made up of agents at the alveolar duct scale. Though stationary, each agent could simulate multi-cell dynamics for a total of 6 different cell types and the interaction network was provided by 10 diffusing extracellular substances. This allowed for larger volumes to be replicated without compromising the model performance so that 30-day-long simulations could be performed on a common laptop with a time resolution of 0.1s in reasonable time. Following an initial calibration in homeostatic conditions, an external damage was simulated by changing the phenotype of a portion of the healthy AEC2 which triggered a global response by gathering M1 macrophages. Contextually, a sensitivity analysis performed on the model parameters showed that the model was mostly sensitive to the rate of transition between M0 and M1. Heterogeneous damage in

the partial acinus was simulated by drawing random numbers from a normal distribution centred on the desired average fraction of damaged AEC2, $\overline{f}$, and using each number for a different alveolar segment. The results showed that the average ECM increased for $0 \leq \overline{f} \leq 40\%$ and dropped for $\overline{f} \geq 40\%$ as the AEC2 couldn't support the fibroblasts population. Interestingly, both in homeostasis and following the external damage the model's output matched previous experimental results [90] and laid the foundations for further 3D ABM of RILI.

Upon validation of the potential of the AB approach, an actual model of RILF was developed. As outlined in Chapter 4, the new model simulated the onset and progression of the disease in an alveolar segment consisting of 18 alveoli arranged in 3 stacked circles. As opposed to the previous work, the model was downscaled so as to mimic cell-scale dynamics. More specifically, the whole simulation space was reduced to a cube with side 2000 μm and divided into voxels with size on the order of that of a CT scan, in order to simplify the comparison between the ECM concentration and the HU measurements. Key radiobiological responses of the alveolar cells were implemented and assigned as behaviours to the cells, with special emphasis on the radiation-induced senescence and subsequent bystander effect. Increasing levels of damage from the x-rays to the healthy epithelium were simulated using an experimental survival curve fitted with the LQ model, with higher doses associated to larger fractions of damaged cells. On the basis of previous experimental results [77], the alveolus was identified as the FSU of the distal airways of the lungs and, based on the concepts outlined in the critical functioning volume model [72], the RSI was introduced as a surrogate measure of the RILF severity. This index, though similar to the FI [158], could be measured by simply determining the fraction of surviving (i.e. non fully depleted of their stem cells) alveoli and the variation in the ECM density.

The simulations, run for virtual times longer than 3 years, provided results that matched qualitatively the findings of experimental studies. In particular, the dose response curve for both the RSI and the average ECM concentration showed a sigmoidal shape with full recovery for $D \leq 5$ Gy. Besides, the ECM displayed a characteristic pattern with an early and a late component that matched the timing of past clinical data. Following an irradiation, eventually all the damaged and senescent AEC2 were cleaned by the macrophages, but higher accumulation of ECM was observed in the voxels of those fully depleted from the epithelial stem cells. Finally, two new parameters were identified as highly influential on the model's outcome: the phagocytic fraction of macrophages, and the senescent to damaged AEC2 ratio. Although setting the first to 100% and the second to 2 provided the most accurate results mentioned before, altering the second showed the key role of senescence in the onset and development of RILF. Overall, this model provided the first framework for simulating the radiation-induced damage at the cell scale in a small 3D region of the lungs, shading new light on the key radiobiological mechanisms involved and highlighting the potential role of ABM for NTCP estimates. Finally, the discrepancies between the model's results for the FSU survival and the corresponding estimates of the LQ model emphasized the importance of taking into account the temporal and spatial tissue evolution in NTCP calculations.

Chapter 5 presents the last and most complex RILF model of the thesis, where, despite few improvements in the behaviours of the simulated agents and no changes in the geometric framework, a radiation transport simulator based on the MC methods was introduced. By using a custom script, the software, named TOPAS-nBio [6], was linked to the AB model developed with BioDynaMo to build a pipeline that allowed data sharing between the two. More specifically, TOPAS-nBio allowed for realistic dose distributions to be simulated using different radiation qualities as well as testing of multi-fractionation schemes. This, in turn, showcased an exclusive feature that can't be replicated by DVH-based phenomenological models of the NTCP and the findings highlighted the actual model's sensitivity to local changes in the dose distribution. As a first step, the alveolar segment geometry in homeostatic conditions was implemented in TOPAS-nBio using position data from the AB model. Following the simulation of an irradiation, for which both the particle type, energy and source could be set, the delivered dose at the cell scale was computed by a custom

scorer and exported. BioDynaMo could then recreate the same structure and determine the fate of the epithelial cells based on the input data. At the end of the simulation, the updated structure could be quickly imported to TOPAS-nBio using a parametrization technique and the process iterated to simulate multiple fractions.

Once the irradiation setup, consisting of an external beam and 4 coplanar fields, was configured, the ability of the AB-MC model to replicate the results of the previous model was tested. The sigmoidal shape of the early and late components of the ECM as well as that of the RSI ensured the consistency of the results and, in addition, good agreement between the LQ model and the FSU survival was found. However, all the dose-response curves were shifted towards higher doses with respect to the previous model for the same outcome, most likely due to the shape of the dose distributions which spanned relatively large ranges and thus resulted in more heterogeneous damages. The temporal fractionation performed with photons, consisting of 5 fractions delivered 24 hours apart, yielded the desired outcomes as a larger fraction of normal tissue was spared with respect to the single fractions thus allowing higher doses for the same outcome, as demonstrated by the shift of the RSI. Unexpectedly, the FSU survival as a function of the dose for the multi-fraction scheme showed better agreement with the LQ model with respect to the single delivery. Remarkable differences with respect to the previous dose distribution resulted in distinct outcomes when the delivery of protons was simulated. In fact, higher RSI values for doses $>$ 10Gy were observed, similarly to the findings of Zhou et al. [207] for higher LET particles. Moreover, the introduction of a novel index, the RBE_{FSU}, allowed for a quantification and direct comparison of the ability of the different radiation qualities to deplete the FSU. As expected, the protons happened to be the most effective, though the comparison was not considered valid for surviving fractions $<$ 37%.

In conclusion, the AB models presented in this work support the use of the approach as a complement to the existing algorithms for NTCP estimates. The models, with increasing complexity, showed that it is possible to integrate cell-level radiobiological data and spatial information about the dose distribution into a framework to predict the course of some radiation-induced toxicity. In contrast to the previous approaches, such as those based on the LQ model, AB models can provide a full temporal and spatial picture of the evolution of the disease at multiple scales. This allows researchers to test the effect of drugs, irradiations or surgery administered/delivered at specific times or locations.

Future developments might involve the use of meta-agents to represent bigger portions of the lungs on the voxel scale to simplify the comparison with patient data. Moreover, the model would benefit from a DNA damage and repair simulator to improve the accuracy of the cells' fate estimates, such as the fraction of senescent and apoptotic cells following the irradiation. Finally, although preliminary studies exist [148], additional data on the cells' radiosensitivity as well as the relative importance of the bystander senescence would increase the robustness of the model's predictions.

Bibliography

[1] Eurostat. *Causes of death statistics - Europe*. 2023.

[2] Tadeusz Dyba et al. "The European cancer burden in 2020: Incidence and mortality estimates for 40 countries and 25 major cancers". In: *European Journal of Cancer* 157 (2021), pp. 308–347. DOI: 10.1016/j.ejca.2021.07.039.

[3] Uri Wilensky and William Rand. *An introduction to agent-based modeling*. January. 2015, pp. 1–504.

[4] Lukas Breitwieser et al. "BioDynaMo: a modular platform for high-performance agent-based simulation". In: *Bioinformatics* (2021). Ed. by Jonathan Wren, pp. 1–9. DOI: 10.1093/bioinformatics/btab649.

[5] Lukas Breitwieser et al. *High-Performance and Scalable Agent-Based Simulation with BioDynaMo*. Vol. 1. 1. Association for Computing Machinery, 2023. DOI: 10.1145/3572848.3577480. arXiv: 2301.06984.

[6] J Schuemann, A L Mcnamara, and J Ramos-me. "TOPAS-nBio : An Extension to the TOPAS Simulation Toolkit for Cellular and Sub-cellular Radiobiology". In: 138 (2019), pp. 125–138. DOI: 10.1667/RR15226.1.

[7] E J Hall and A J Giaccia. *Radiobiology for the Radiologist*. LWW medical book collection. Lippincott Williams & Wilkins, 2006.

[8] Marco Durante and Harald Paganetti. "Nuclear physics in particle therapy: A review". In: *Reports on Progress in Physics* 79.9 (2016), p. 96702. DOI: 10.1088/0034-4885/79/9/096702.

[9] Stephen J. McMahon and Kevin M. Prise. "Mechanistic modelling of radiation responses". In: *Cancers* 11.2 (2019). DOI: 10.3390/cancers11020205.

[10] Stephen Joseph McMahon. "The linear quadratic model: usage, interpretation and challenges." In: *Physics in medicine and biology* 64.1 (2018), 01TR01. DOI: 10.1088/1361-6560/aaf26a.

[11] Clint Park et al. "Universal Survival Curve and Single Fraction Equivalent Dose: Useful Tools in Understanding Potency of Ablative Radiotherapy". In: *International Journal of Radiation Oncology*Biology*Physics* 70.3 (2008), pp. 847–852. DOI: 10.1016/j.ijrobp.2007.10.059.

[12] J. F. Fowler. "Differences in Survival Curve Shapes for Formal Multi-target and Multi-hit Models". In: *Physics in Medicine and Biology* 9.2 (1964), p. 305. DOI: 10.1088/0031-9155/9/2/305.

[13] Dieter Schardt, Thilo Elsässer, and Daniela Schulz-Ertner. "Heavy-ion tumor therapy: Physical and radiobiological benefits". In: *Reviews of Modern Physics* 82.1 (2010), pp. 383–425. DOI: 10.1103/RevModPhys.82.383.

[14] Stephen J. Mcmahon et al. "Mechanistic Modelling of DNA Repair and Cellular Survival Following Radiation-Induced DNA Damage". In: *Scientific Reports* 6.April (2016), pp. 1–14. DOI: 10.1038/srep33290.

[15] Peggy L. Olive. "The Role of DNA Single- and Double-Strand Breaks in Cell Killing by Ionizing Radiation". In: *Radiation Research* 150.5 (1998), S42. DOI: 10.2307/3579807.

[16] Shenghui He and Norman E. Sharpless. “Senescence in Health and Disease”. In: *Cell* 169.6 (2017), pp. 1000–1011. DOI: 10.1016/j.cell.2017.05.015.

[17] Marco Durante and Jay S. Loeffler. “Charged particles in radiation oncology”. In: *Nature Reviews Clinical Oncology* 7.1 (2010), pp. 37–43. DOI: 10.1038/nrclinonc.2009.183.

[18] Thilo Elsässer, Michael Krämer, and Michael Scholz. “Accuracy of the local effect model for the prediction of biologic effects of carbon ion beams in vitro and in vivo.” In: *International journal of radiation oncology, biology, physics* 71.3 (2008), pp. 866–72. DOI: 10.1016/j.ijrobp.2008.02.037.

[19] Jochen Fleckenstein et al. “Dose distribution and tumor control probability in out-of-field lymph node stations in intensity modulated radiotherapy (IMRT) vs 3D-conformal radiotherapy (3D-CRT) of non-small-cell lung cancer: An in silico analysis”. In: *Radiation Oncology* 10.1 (2015), pp. 1–7. DOI: 10.1186/s13014-015-0485-6.

[20] Marcelo F. Benveniste et al. “Recognizing radiation therapy– related complications in the chest”. In: *Radiographics* 39.2 (2019), pp. 344–366. DOI: 10.1148/rg.2019180061.

[21] Stephen G. Chun et al. “Impact of intensity-modulated radiation therapy technique for locally advanced non-small-cell lung cancer: A secondary analysis of the NRG oncology RTOG 0617 randomized clinical trial”. In: *Journal of Clinical Oncology* 35.1 (2017), pp. 56–62. DOI: 10.1200/JCO.2016.69.1378.

[22] Robin Wijsman et al. “Comparison of toxicity and outcome in advanced stage non-small cell lung cancer patients treated with intensity-modulated (chemo-)radiotherapy using IMRT or VMAT”. In: *Radiotherapy and Oncology* 122.2 (2017), pp. 295–299. DOI: 10.1016/j.radonc.2016.11.015.

[23] Alexander N. Hanania et al. “Radiation-Induced Lung Injury: Assessment and Management”. In: *Chest* 156.1 (2019), pp. 150–162. DOI: 10.1016/j.chest.2019.03.033.

[24] Matthias Ochs et al. “The Number of Alveoli in the Human Lung”. In: *American Journal of Respiratory and Critical Care Medicine* 169.1 (2004), pp. 120–124. DOI: 10.1164/rccm.200308-1107oc.

[25] Ewald R Weibel. *Morphometry of the Human Lung*. Ed. by Springer. 1st ed. Berlin, Heidelberg: Springer Berlin Heidelberg, 1963, p. 151. DOI: 10.1007/978-3-642-87553-3.

[26] Beatrice Haefeli-Bleuer and Ewald R. Weibel. “Morphometry of the human pulmonary acinus”. In: *The Anatomical Record* 220.4 (1988), pp. 401–414. DOI: 10.1002/ar.1092200410.

[27] Ewald R. Weibel, Bernard Sapoval, and Marcel Filoche. “Design of peripheral airways for efficient gas exchange”. In: *Respiratory Physiology and Neurobiology* 148.1-2 SPEC. ISS. (2005), pp. 3–21. DOI: 10.1016/j.resp.2005.03.005.

[28] Kyle J. Travaglini et al. “A molecular cell atlas of the human lung from single cell RNA sequencing”. In: *bioRxiv* 587.November (2019). DOI: 10.1101/742320.

[29] K. C. Stone et al. “Allometric relationships of cell numbers and size in the mammalian lung.” In: *American journal of respiratory cell and molecular biology* 6.2 (1992), pp. 235–243. DOI: 10.1165/ajrcmb/6.2.235.

[30] Klaus Rüdiger Trott, Thomas Herrmann, and Michael Kasper. “Target cells in radiation pneumopathy”. In: *International Journal of Radiation Oncology Biology Physics* 58.2 (2004), pp. 463–469. DOI: 10.1016/j.ijrobp.2003.09.045.

[31] Marek Konkol et al. “Normal Lung Tissue CT Density Changes after Volumetric-Arc Radiotherapy (VMAT) for Lung Cancer”. In: *Journal of Personalized Medicine* 12.3 (2022), p. 485. DOI: 10.3390/jpm12030485.

[32] Hee Jin et al. “Radiation-induced lung fibrosis: Preclinical animal models and therapeutic strategies”. In: *Cancers* 12.6 (2020), pp. 1–24. DOI: 10.3390/cancers12061561.

[33] David A. Palma et al. “Predicting radiation pneumonitis after chemoradiation therapy for lung cancer: An international individual patient data meta-analysis”. In: *International Journal of Radiation Oncology Biology Physics* 85.2 (2013), pp. 444–450. DOI: 10.1016/j.ijrobp.2012.04.043.

[34] Kayoko Tsujino et al. “Combined analysis of V20, VS5, pulmonary fibrosis score on baseline computed tomography, and patient age improves prediction of severe radiation pneumonitis after concurrent chemoradiotherapy for locally advanced non-small-cell lung cancer”. In: *Journal of Thoracic Oncology* 9.7 (2014), pp. 983–990. DOI: 10.1097/JTO.0000000000000187.

[35] Lawrence B. Marks et al. “Radiation Dose-Volume Effects in the Lung”. In: *International Journal of Radiation Oncology Biology Physics* 76.3 SUPPL. (2010), pp. 70–76. DOI: 10.1016/j.ijrobp.2009.06.091.

[36] Xiao Jing Zhang et al. “Prediction of radiation pneumonitis in lung cancer patients: A systematic review”. In: *Journal of Cancer Research and Clinical Oncology* 138.12 (2012), pp. 2103–2116. DOI: 10.1007/s00432-012-1284-1.

[37] Feng-Ming Spring Kong and Shulian Wang. “Nondosimetric risk factors for radiation-induced lung toxicity.” In: *Seminars in radiation oncology* 25.2 (2015), pp. 100–9. DOI: 10.1016/j.semradonc.2014.12.003.

[38] Etienne Giroux Leprieur et al. “Acute radiation pneumonitis after conformational radiotherapy for nonsmall cell lung cancer: Clinical, dosimetric, and associated-treatment risk factors”. In: *Journal of Cancer Research and Therapeutics* 9.3 (2013), pp. 447–451. DOI: 10.4103/0973-1482.119339.

[39] Sean M. Parker et al. “Impact of Tumor Size on Local Control and Pneumonitis After Stereotactic Body Radiation Therapy for Lung Tumors”. In: *Practical Radiation Oncology* 9.1 (2019), e90–e97. DOI: 10.1016/j.prro.2018.09.003.

[40] Ellen X. Huang et al. “Heart irradiation as a risk factor for radiation pneumonitis”. In: *Acta Oncologica* 50.1 (2011), pp. 51–60. DOI: 10.3109/0284186X.2010.521192.

[41] Jun Dang et al. “Comparison of risk and predictors for early radiation pneumonitis in patients with locally advanced non-small cell lung cancer treated with radiotherapy with or without surgery”. In: *Lung Cancer* 86.3 (2014), pp. 329–333. DOI: 10.1016/j.lungcan.2014.10.005.

[42] Cary Dehing-Oberije et al. “The importance of patient characteristics for the prediction of radiation-induced lung toxicity”. In: *Radiotherapy and Oncology* 91.3 (2009), pp. 421–426. DOI: 10.1016/j.radonc.2008.12.002.

[43] Hekun Jin et al. “Dose-volume thresholds and smoking status for the risk of treatment-related pneumonitis in inoperable non-small cell lung cancer treated with definitive radiotherapy.” In: *Radiotherapy and oncology : journal of the European Society for Therapeutic Radiology and Oncology* 91.3 (2009), pp. 427–32. DOI: 10.1016/j.radonc.2008.09.009.

[44] James D. Cox, JoAnn Stetz, and Thomas F. Pajak. “Toxicity criteria of the Radiation Therapy Oncology Group (RTOG) and the European organization for research and treatment of cancer (EORTC)”. In: *International Journal of Radiation Oncology*Biology*Physics* 31.5 (1995), pp. 1341–1346. DOI: 10.1016/0360-3016(95)00060-C.

[45] National Cancer Institute (US). *Common Terminology Criteria for Adverse Events (CTCAE) 2017*. 2017.

[46] Anna Linda, Marco Trovo, and Jeffrey D. Bradley. "Radiation injury of the lung after stereotactic body radiation therapy (SBRT) for lung cancer: A timeline and pattern of CT changes". In: *European Journal of Radiology* 79.1 (2011), pp. 147–154. DOI: 10.1016/j.ejrad.2009.10.029.

[47] Max Dahele et al. "Radiological changes after stereotactic radiotherapy for stage I lung cancer". In: *Journal of Thoracic Oncology* 6.7 (2011), pp. 1221–1228. DOI: 10.1097/JTO.0b013e318219aac5.

[48] Walter De Wever et al. "The crazy-paving pattern: a radiological-pathological correlation". In: *Insights into Imaging* 2.2 (2011), pp. 117–132. DOI: 10.1007/s13244-010-0060-5.

[49] Yo Won Choi et al. "Effects of radiation therapy on the lung: Radiologic appearances and differential diagnosis". In: *Radiographics* 24.4 (2004), pp. 985–997. DOI: 10.1148/rg.244035160.

[50] Gilles Defraene, Wouter van Elmpt, and Dirk De Ruysscher. "Regional lung avoidance by CT numbers to reduce radiation-induced lung damage risk in non-small-cell lung cancer: a simulation study." In: *Acta oncologica (Stockholm, Sweden)* 59.2 (2020), pp. 201–207. DOI: 10.1080/0284186X.2019.1669814.

[51] Gilles Defraene et al. "Radiation-Induced Lung Density Changes on CT Scan for NSCLC: No Impact of Dose-Escalation Level or Volume." In: *International journal of radiation oncology, biology, physics* 102.3 (2018), pp. 642–650. DOI: 10.1016/j.ijrobp.2018.06.038.

[52] Christina Schröder et al. "Changes of lung parenchyma density following high dose radiation therapy for thoracic carcinomas - An automated analysis of follow up CT scans". In: *Radiation Oncology* 14.1 (2019), pp. 1–7. DOI: 10.1186/s13014-019-1276-2.

[53] Uffe Bernchou et al. *Time evolution of regional CT density changes in normal lung after IMRT for NSCLC*. 2013. DOI: 10.1016/j.radonc.2013.08.041.

[54] Yanjing Li et al. "Differential inflammatory response dynamics in normal lung following stereotactic body radiation therapy with protons versus photons". In: *Radiotherapy and Oncology* 136 (2019), pp. 169–175. DOI: 10.1016/j.radonc.2019.04.004.

[55] Cheng Zhou et al. "Modeling and multiscale characterization of the quantitative imaging based fibrosis index reveals pathophysiological, transcriptome and proteomic correlates of lung fibrosis induced by fractionated irradiation". In: *International Journal of Cancer* 144.12 (2019), pp. 3160–3173. DOI: 10.1002/ijc.32059.

[56] S. M. Bentzen, J. Z. Skoczylas, and J. Bernier. "Quantitative clinical radiobiology of early and late lung reactions". In: *International Journal of Radiation Biology* 76.4 (2000), pp. 453–462. DOI: 10.1080/095530000138448.

[57] S. M. Bentzen and S. L. Tucker. "Quantifying the position and steepness of radiation dose-response curves". In: *International Journal of Radiation Biology* 71.5 (1997), pp. 531–542. DOI: 10.1080/095530097143860.

[58] Shifeng Chen et al. "Investigation of the support vector machine algorithm to predict lung radiation-induced pneumonitis". In: *Medical Physics* 34.10 (2007), pp. 3808–3814. DOI: 10.1118/1.2776669.

[59] Hermann Holthusen. "Erfahrungen über die Verträglichkeitsgrenze für Röntgenstrahlen und deren Nutzanwendung zur Verhütung von Schäden". In: *Strahlentherapie* 57.254 (1936), 51a.

[60] Gillian C. Barnett et al. "Normal tissue reactions to radiotherapy". In: *Nat Rev Cancer* 9.2 (2009), pp. 134–142. DOI: 10.1038/nrc2587.Normal.

[61] Anders Brahme. “Dosimetric Precision Requirements in Radiation Therapy.” In: 23.January (1984), pp. 269–274.

[62] J. T. Lyman. “Complication probability as assessed from dose-volume histograms.” In: *Radiation research. Supplement* 8 (1985), S13–9. DOI: 10.2307/3583506.

[63] G J Kutcher and C Burman. “Calculation of complication probability factors for non-uniform normal tissue irradiation: the effective volume method.” In: *International journal of radiation oncology, biology, physics* 16.6 (1989), pp. 1623–30. DOI: 10.1016/0360-3016(89)90972-3.

[64] R Mohan et al. “Clinically relevant optimization of 3-D conformal treatments.” In: *Medical physics* 19.4 (1992), pp. 933–44. DOI: 10.1118/1.596781.

[65] Timothy E. Schultheiss, Colin G. Orton, and R. A. Peck. “Models in radiotherapy: Volume effects”. In: *Medical Physics* 10.4 (1983), pp. 410–415. DOI: 10.1118/1.595312.

[66] T. R. Munro and C. W. Gilbert. “The Relation Between Tumour Lethal Doses and the Radiosensitivity of Tumour Cells”. In: *The British Journal of Radiology* 34.400 (1961), pp. 246–251. DOI: 10.1259/0007-1285-34-400-246.

[67] P. Källman, A Agren, and A. Brahme. “Tumour and normal tissue responses to fractionated non-uniform dose delivery.” In: *International journal of radiation biology* 62.2 (1992), pp. 249–62. DOI: 10.1080/09553009214552071.

[68] H. Rodney Withers, Jeremy M.G. Taylor, and Boguslaw Maciejewski. “Treatment volume and tissue tolerance”. In: *International Journal of Radiation Oncology*Biology*Physics* 14.4 (1988), pp. 751–759. DOI: 10.1016/0360-3016(88)90098-3.

[69] P. Stavrev et al. “Critical volume model analysis of lung complication data from different strains of mice”. In: *International Journal of Radiation Biology* 81.1 (2005), pp. 77–88. DOI: 10.1080/09553000400027910.

[70] R. Timmerman et al. “Optimizing dose and fractionation for stereotactic body radiation therapy”. In: *Frontiers of Radiation Therapy and Oncology* 40 (2007), pp. 352–365. DOI: 10.1159/0000106046.

[71] A. Jackson, G. J. Kutcher, and E. D. Yorke. “Probability of radiation-induced complications for normal tissues with parallel architecture subject to non-uniform irradiation.” In: *Medical physics* 20.3 (1993), pp. 613–25. DOI: 10.1118/1.597056.

[72] Andrzej Niemierko and Michael Goitein. “Modeling of normal tissue response to radiation: The critical volume model”. In: *International Journal of Radiation Oncology, Biology, Physics* 25.1 (1993), pp. 135–145. DOI: 10.1016/0360-3016(93)90156-P.

[73] P Stavrev et al. “Generalization of a model of tissue response to radiation based on the idea of functional subunits and binomial statistics.” In: *Physics in medicine and biology* 46.5 (2001), pp. 1501–18. DOI: 10.1088/0031-9155/46/5/312.

[74] Stephen J. McMahon et al. “A Kinetic-Based Model of Radiation-Induced Intercellular Signalling”. In: *PLoS ONE* 8.1 (2013), pp. 15–18. DOI: 10.1371/journal.pone.0054526.

[75] Giuseppe Palma et al. “Normal tissue complication probability (NTCP) models for modern radiation therapy”. In: *Seminars in Oncology* 46.3 (2019), pp. 210–218. DOI: 10.1053/j.seminoncol.2019.07.006.

[76] P. Andreo. “Monte Carlo techniques in medical radiation physics”. In: *Physics in Medicine and Biology* 36.7 (1991), pp. 861–920. DOI: 10.1088/0031-9155/36/7/001.

[77] Eva Rutkowska et al. “Mechanistic modelling of radiotherapy-induced lung toxicity”. In: *British Journal of Radiology* 85.1020 (2012). DOI: 10.1259/bjr/28365782.

[78] J. Schuemann et al. “A New Standard DNA Damage (SDD) Data Format”. In: *Radiation Research* 191.1 (2019), pp. 76–92. DOI: 10.1667/RR15209.1.

[79] Yonghan He et al. “Cellular senescence and radiation-induced pulmonary fibrosis”. In: *Translational Research* 209 (2019), pp. 14–21. DOI: 10.1016/j.trsl.2019.03.006.

[80] Leonid Hanin and Marco Zaider. “A mechanistic description of radiation-induced damage to normal tissue and its healing kinetics”. In: *Physics in Medicine and Biology* 58.4 (2013), pp. 825–839. DOI: 10.1088/0031-9155/58/4/825.

[81] Nicolò Cogno, Roman Bauer, and Marco Durante. “An Agent-Based Model of Radiation-Induced Lung Fibrosis”. In: *International Journal of Molecular Sciences* 23.22 (2022). DOI: 10.3390/ijms232213920.

[82] Nicolò Cogno, Roman Bauer, and Marco Durante. “A 3D Agent-Based Model of Lung Fibrosis”. In: *Symmetry* 14.1 (2022). DOI: 10.3390/sym14010090.

[83] Rebecca Anne et al. “Mathematical modeling of radiotherapy and its impact on tumor interactions with the immune system”. In: *Neoplasia* 28.xxx (2022), p. 100796. DOI: 10.1016/j.neo.2022.100796.

[84] John Metzcar et al. “A Review of Cell-Based Computational Modeling in Cancer Biology”. In: *JCO Clinical Cancer Informatics* 3 (2019), pp. 1–13. DOI: 10.1200/cci.18.00069.

[85] Michael Wooldridge. *An Introduction to MultiAgent Systems*. John Wiley and Sons, Inc., 2002.

[86] Hans Petter Langtangen and Svein Linge. *Finite Difference Computing with PDEs*. Vol. 16. Texts in Computational Science and Engineering. Cham: Springer International Publishing, 2017. DOI: 10.1007/978-3-319-55456-3.

[87] Dirk Drasdo and Stefan Höhme. “A single-cell-based model of tumor growth in vitro: Monolayers and spheroids”. In: *Physical Biology* 2.3 (2005), pp. 133–147. DOI: 10.1088/1478-3975/2/3/001.

[88] OpenMP Architecture Review Board. *OpenMP*.

[89] Syslab. *Singularity*.

[90] Wenrui Hao, Clay Marsh, and Avner Friedman. “A mathematical model of idiopathic pulmonary fibrosis”. In: *PLoS ONE* 10.9 (2015), pp. 1–19. DOI: 10.1371/journal.pone.0135097.

[91] Luca Richeldi, Harold R. Collard, and Mark G. Jones. “Idiopathic pulmonary fibrosis”. In: *The Lancet* 389.10082 (2017), pp. 1941–1952. DOI: 10.1016/S0140-6736(17)30866-8.

[92] Görkem Türkkan et al. “Idiopathic pulmonary fibrosis: Current knowledge, future perspectives and its importance in radiation oncology”. In: *Radiotherapy and Oncology* 155 (2021), pp. 269–277. DOI: 10.1016/j.radonc.2020.11.020.

[93] Fernando J. Martinez et al. “Idiopathic pulmonary fibrosis”. In: *Nature Reviews Disease Primers* 3 (2017), pp. 1–20. DOI: 10.1038/nrdp.2017.74.

[94] Ewald R. Weibel. “Lung morphometry: the link between structure and function”. In: *Cell and Tissue Research* 367.3 (2017), pp. 413–426. DOI: 10.1007/s00441-016-2541-4.

[95] Thomas H. Sisson et al. “Targeted injury of type II alveolar epithelial cells induces pulmonary fibrosis”. In: *American Journal of Respiratory and Critical Care Medicine* 181.3 (2010), pp. 254–263. DOI: 10.1164/rccm.200810-1615OC.

[96] Ana Camelo et al. “The epithelium in idiopathic pulmonary fibrosis: Breaking the barrier”. In: *Frontiers in Pharmacology* 4 JAN.January (2014), pp. 1–11. DOI: 10.3389/fphar.2013.00173.

[97] Moisés Selman and Annie Pardo. “Role of epithelial cells in idiopathic pulmonary fibrosis: From innocent targets to serial killers”. In: *Proceedings of the American Thoracic Society* 3.4 (2006), pp. 364–372. DOI: 10.1513/pats.200601-003TK.

[98] Tanyalak Parimon et al. “Alveolar epithelial type II cells as drivers of lung fibrosis in idiopathic pulmonary fibrosis”. In: *International Journal of Molecular Sciences* 21.7 (2020). DOI: 10.3390/ijms21072269.

[99] Changfu Yao et al. “Senescence of Alveolar Type 2 Cells Drives Progressive Pulmonary Fibrosis”. In: *American Journal of Respiratory and Critical Care Medicine* 203.6 (2021), pp. 707–717. DOI: 10.1164/rccm.202004-1274OC.

[100] Elizabeth F. Redente et al. “Tumor necrosis factor-α accelerates the resolution of established pulmonary fibrosis in mice by targeting profibrotic lung macrophages”. In: *American Journal of Respiratory Cell and Molecular Biology* 50.4 (2014), pp. 825–837. DOI: 10.1165/rcmb.2013-0386OC.

[101] T. J. Broekelmann et al. “Transforming growth factor β1 is present at sites of extracellular matrix gene expression in human pulmonary fibrosis”. In: *Proceedings of the National Academy of Sciences of the United States of America* 88.15 (1991), pp. 6642–6646. DOI: 10.1073/pnas.88.15.6642.

[102] Nasreen Khalil et al. “Regulation of alveolar macrophage transforming growth factor-β secretion by corticosteroids in bleomycin-induced pulmonary inflammation in the rat”. In: *Journal of Clinical Investigation* 92.4 (1993), pp. 1812–1818. DOI: 10.1172/JCI116771.

[103] I Nagaoka, B C Trapnell, and R G Crystal. “Upregulation of platelet-derived growth factor-A and -B gene expression in alveolar macrophages of individuals with idiopathic pulmonary fibrosis.” In: *Journal of Clinical Investigation* 85.6 (1990), pp. 2023–2027. DOI: 10.1172/JCI114669.

[104] Anne Hancock et al. “Production of interleukin 13 by alveolar macrophages from normal and fibrotic lung”. In: *American Journal of Respiratory Cell and Molecular Biology* 18.1 (1998), pp. 60–65. DOI: 10.1165/ajrcmb.18.1.2627.

[105] Moises Selman et al. “TIMP-1, -2, -3, and -4 in idiopathic pulmonary fibrosis. A prevailing nondegradative lung microenvironment?” In: *American Journal of Physiology-Lung Cellular and Molecular Physiology* 279.3 (2000), pp. L562–L574. DOI: 10.1152/ajplung.2000.279.3.L562.

[106] J Kelley et al. “Cytokine signaling in lung: transforming growth factor-beta secretion by lung fibroblasts.” eng. In: *The American journal of physiology* 260.2 Pt 1 (1991), pp. L123–8. DOI: 10.1152/ajplung.1991.260.2.L123.

[107] G Raghu et al. “Collagen synthesis by normal and fibrotic human lung fibroblasts and the effect of transforming growth factor-beta.” eng. In: *The American review of respiratory disease* 140.1 (1989), pp. 95–100. DOI: 10.1164/ajrccm/140.1.95.

[108] Pengfei Lu et al. “Extracellular Matrix degradation and remodeling in development and disease”. In: *Cold Spring Harbor Perspectives in Biology* 3.12 (2011), pp. 1–24. DOI: 10.1101/cshperspect.a005058.

[109] Y. Morishima et al. “Triggering the induction of myofibroblast and fibrogenesis by airway epithelial shedding”. In: *American Journal of Respiratory Cell and Molecular Biology* 24.1 (2001), pp. 1–11. DOI: 10.1165/ajrcmb.24.1.4040.

[110] Stefan Fichtner-Feigl et al. “IL-13 signaling through the IL-13α2 receptor is involved in induction of TGF-β1 production and fibrosis”. In: *Nature Medicine* 12.1 (2006), pp. 99–106. DOI: 10.1038/nm1332.

[111] M. Hetzel et al. “Different effects of growth factors on proliferation and matrix production of normal and fibrotic human lung fibroblasts”. In: *Lung* 183.4 (2005), pp. 225–237. DOI: 10.1007/s00408-004-2534-z.

[112] Li Gu et al. “Effect of TGF-β/Smad signaling pathway on lung myofibroblast differentiation”. In: *Acta Pharmacologica Sinica* 28.3 (2007), pp. 382–391. DOI: 10.1111/j.1745-7254.2007.00468.x.

[113] Naoki Hagimoto et al. “TGF-β1 as an Enhancer of Fas-Mediated Apoptosis of Lung Epithelial Cells”. In: *The Journal of Immunology* 168.12 (2002), pp. 6470–6478. DOI: 10.4049/jimmunol.168.12.6470.

[114] Akira Saito et al. “Potential action of IL-4 and IL-13 as fibrogenic factors on lung fibroblasts in vitro.” eng. In: *International archives of allergy and immunology* 132.2 (2003), pp. 168–176. DOI: 10.1159/000073718.

[115] Li Xiao. “TGF-beta 1 induced fibroblast proliferation is mediated by the FGF-2/ERK pathway”. In: *Frontiers in Bioscience* 17.7 (2012), p. 2667. DOI: 10.2741/4077.

[116] Cheng Ming Li et al. “TGF-β1 and fibroblast growth factor-1 modify fibroblast growth factor-2 production in type II cells”. In: *American Journal of Physiology - Lung Cellular and Molecular Physiology* 279.6 23-6 (2000), pp. 1038–1046. DOI: 10.1152/ajplung.2000.279.6.l1038.

[117] Hans Boström et al. “PDGF-A signaling is a critical event in lung alveolar myofibroblast development and alveogenesis”. In: *Cell* 85.6 (1996), pp. 863–873. DOI: 10.1016/S0092-8674(00)81270-2.

[118] Kai Zhang et al. “Myofibroblasts and their role in lung collagen gene expression during pulmonary fibrosis: A combined immunohistochemical and in situ hybridization study”. In: *American Journal of Pathology* 145.1 (1994), pp. 114–125.

[119] Victor V. Petrov, Robert H. Fagard, and Paul J. Lijnen. “Stimulation of collagen production by transforming growth factor-β1 during differentiation of cardiac fibroblasts to myofibroblasts”. In: *Hypertension* 39.2 I (2002), pp. 258–263. DOI: 10.1161/hy0202.103268.

[120] Kevin K. Kim et al. “Alveolar epithelial cell mesenchymal transition develops in vivo during pulmonary fibrosis and is regulated by the extracellular matrix”. In: *Proceedings of the National Academy of Sciences of the United States of America* 103.35 (2006), pp. 13180–13185. DOI: 10.1073/pnas.0605669103.

[121] Jun Tashiro et al. “Exploring animal models that resemble idiopathic pulmonary fibrosis”. In: *Frontiers in Medicine* 4.JUL (2017), pp. 1–11. DOI: 10.3389/fmed.2017.00118.

[122] G. Wayne Brodland. “How computational models can help unlock biological systems”. In: *Seminars in Cell and Developmental Biology* 47-48 (2015), pp. 62–73. DOI: 10.1016/j.semcdb.2015.07.001.

[123] Raimond L. Winslow et al. “Computational medicine: Translating models to clinical care”. In: *Science Translational Medicine* 4.158 (2012), pp. 1–12. DOI: 10.1126/scitranslmed.3003528.

[124] Asit Saha and Barsha Saha. “Novel coronavirus SARS-CoV-2 (Covid-19) dynamics inside the human body”. In: *Reviews in Medical Virology* 30.5 (2020), pp. 1–11. DOI: 10.1002/rmv.2140.

[125] Giulia Giordano et al. *Modelling the COVID-19 epidemic and implementation of population-wide interventions in Italy*. Vol. 26. 6. Springer US, 2020, pp. 855–860. DOI: 10.1038/s41591-020-0883-7.

[126] H. Van Dyke Parunak, Robert Savit, and Rick L. Riolo. “Agent-Based Modeling vs. Equation-Based Modeling: A Case Study and Users’ Guide”. In: *Lecture Notes in Computer Science*. 1998, pp. 10–25. DOI: 10.1007/10692956_2.

[127] James D. Murray. *Mathematical Biology II*. Ed. by J. D. Murray. Vol. 18. Interdisciplinary Applied Mathematics. New York, NY: Springer New York, 2003. DOI: 10.1007/b98869.

[128] James D Murray. *Mathematical Biology I*. Ed. by J. D. Murray. 3rd ed. Vol. 17. Interdisciplinary Applied Mathematics. New York, NY: Springer New York, 2002. DOI: 10.1007/b98868.

[129] Eric Bonabeau. “Agent-based modeling: Methods and techniques for simulating human systems”. In: *Proceedings of the National Academy of Sciences of the United States of America* 99.SUPPL. 3 (2002), pp. 7280–7287. DOI: 10.1073/pnas.082080899.

[130] Nicholas A. Cilfone, Denise E. Kirschner, and Jennifer J. Linderman. “Strategies for Efficient Numerical Implementation of Hybrid Multi-scale Agent-Based Models to Describe Biological Systems”. In: *Cellular and Molecular Bioengineering* 8.1 (2015), pp. 119–136. DOI: 10.1007/s12195-014-0363-6.

[131] Hayley C. Warsinske et al. “Computational Modeling Predicts Simultaneous Targeting of Fibroblasts and Epithelial Cells Is Necessary for Treatment of Pulmonary Fibrosis”. In: *Frontiers in Pharmacology* 7.JUN (2016). DOI: 10.3389/fphar.2016.00183.

[132] S. Michaela Rikard et al. “Multiscale Coupling of an Agent-Based Model of Tissue Fibrosis and a Logic-Based Model of Intracellular Signaling”. In: *Frontiers in Physiology* 10.December (2019). DOI: 10.3389/fphys.2019.01481.

[133] Bryan N. Brown et al. “An agent-based model of inflammation and fibrosis following particulate exposure in the lung”. In: *Mathematical Biosciences* 231.2 (2011), pp. 186–196. DOI: 10.1016/j.mbs.2011.03.005. arXiv: NIHMS150003.

[134] Tyler J Wellman et al. “Topographic distribution of idiopathic pulmonary fibrosis: a hybrid physics- and agent-based model.” In: *Physiological measurement* 39.6 (2018), p. 064007. DOI: 10.1088/1361-6579/aaca86.

[135] Gregory A. Paulin et al. “Noninvasive quantification of alveolar morphometry in elderly never- and ex-smokers”. In: *Physiological Reports* 3.10 (2015), pp. 1–13. DOI: 10.14814/phy2.12583.

[136] J. E. Hansen and E. P. Ampaya. “Human air space shapes, sizes, areas, and volumes”. In: *Journal of Applied Physiology* 38.6 (1975), pp. 990–995. DOI: 10.1152/jappl.1975.38.6.990.

[137] Dmitriy A. Yablonskiy et al. “Quantification of lung microstructure with hyperpolarized 3He diffusion MRI”. In: *Journal of Applied Physiology* 107.4 (2009), pp. 1258–1265. DOI: 10.1152/japplphysiol.00386.2009.

[138] Pavel Dvorak et al. “Computer-assisted engineering of hyperstable fibroblast growth factor 2”. In: *Biotechnology and Bioengineering* 115.4 (2018), pp. 850–862. DOI: 10.1002/bit.26531.

[139] Michał Kołodziej et al. “Scale up of a chromatographic capture step for a clarified bacterial homogenate – Influence of mass transport limitation and competitive adsorption of impurities”. In: *Journal of Chromatography A* 1618 (2020). DOI: 10.1016/j.chroma.2020.460856.

[140] Rene Brun and Fons Rademakers. “ROOT - An object oriented data analysis framework”. In: *Nuclear Instruments and Methods in Physics Research, Section A: Accelerators, Spectrometers, Detectors and Associated Equipment* 389.1-2 (1997), pp. 81–86. DOI: 10.1016/S0168-9002(97)00048-X.

[141] Jessica R. Perez et al. “A comparative analysis of longitudinal computed tomography and histopathology for evaluating the potential of mesenchymal stem cells in mitigating radiation-induced pulmonary fibrosis”. In: *Scientific Reports* 7.1 (2017), pp. 1–10. DOI: 10.1038/s41598-017-09021-7.

[142] K Mah and J Van Dyk. “Quantitative measurement of changes in human lung density following irradiation”. In: *Radiotherapy and Oncology* 11.2 (1988), pp. 169–179. DOI: 10.1016/0167-8140(88)90253-8.

[143] Shirley Lehnert and Ellen El-Khatib. “The use of CT densitometry in the assessment of radiation-induced damage to the rat lung: A comparison with other endpoints”. In: *International Journal of Radiation Oncology, Biology, Physics* 16.1 (1989), pp. 117–124. DOI: 10.1016/0360-3016(89)90018-7.

[144] Feng Du et al. “Correlation Between Lung Density Changes Under Different Dose Gradients and Radiation Pneumonitis—Based on an Analysis of Computed Tomography Scans During Esophageal Cancer Radiotherapy”. In: *Frontiers in Oncology* 11.May (2021), pp. 1–9. DOI: 10.3389/fonc.2021.650764.

[145] Grazziela P. Figueredo et al. “Comparing stochastic differential equations and agent-based modelling and simulation for early-stage cancer”. In: *PLoS ONE* 9.4 (2014), pp. 1–18. DOI: 10.1371/journal.pone.0095150.

[146] Lorena Giuranno et al. “Radiation-Induced Lung Injury (RILI)”. In: *Frontiers in Oncology* 9.September (2019), pp. 1–16. DOI: 10.3389/fonc.2019.00877.

[147] Marisol Arroyo-Hernández et al. “Radiation-induced lung injury: current evidence”. In: *BMC Pulmonary Medicine* 21.1 (2021), pp. 1–12. DOI: 10.1186/s12890-020-01376-4.

[148] Deborah E. Citrin et al. “Role of type II pneumocyte senescence in radiation-induced lung fibrosis”. In: *Journal of the National Cancer Institute* 105.19 (2013), pp. 1474–1484. DOI: 10.1093/jnci/djt212.

[149] Deborah E. Citrin et al. “Radiation-Induced Fibrosis: Mechanisms and Opportunities to Mitigate. Report of an NCI Workshop, September 19, 2016.” In: *Radiation Research* 188.1 (2017), pp. 1–20. DOI: 10.1667/RR14784.1.

[150] Xiaojing Hong et al. “Molecular Mechanisms of Alveolar Epithelial Stem Cell Senescence and Senescence-Associated Differentiation Disorders in Pulmonary Fibrosis”. In: *Cells* 11.5 (2022), p. 877. DOI: 10.3390/cells11050877.

[151] Soumyajit Roy, Kilian E. Salerno, and Deborah E. Citrin. “Biology of Radiation-Induced Lung Injury”. In: *Seminars in Radiation Oncology* 31.2 (2021), pp. 155–161. DOI: 10.1016/j.semradonc.2020.11.006.

[152] E. C.J. Phernambucq et al. “Outcomes of concurrent chemoradiotherapy in patients with stage III non-small-cell lung cancer and significant comorbidity”. In: *Annals of Oncology* 22.1 (2011), pp. 132–138. DOI: 10.1093/annonc/mdq316.

[153] R. Bryan Barriger et al. “Dose-volume analysis of radiation pneumonitis in non-small-cell lung cancer patients treated with concurrent cisplatinum and etoposide with or without consolidation docetaxel”. In: *International Journal of Radiation Oncology Biology Physics* 78.5 (2010), pp. 1381–1386. DOI: 10.1016/j.ijrobp.2009.09.030.

[154] Magdalena Adamus-Górka et al. “Comparison of dose response models for predicting normal tissue complications from cancer radiotherapy: Application in rat spinal cord”. In: *Cancers* 3.2 (2011), pp. 2421–2443. DOI: 10.3390/cancers3022421.

[155] Glyn Nelson et al. “A senescent cell bystander effect: Senescence-induced senescence”. In: *Aging Cell* 11.2 (2012), pp. 345–349. DOI: 10.1111/j.1474-9726.2012.00795.x.

[156] Larissa G.P.Langhi Prata et al. “Senescent cell clearance by the immune system: Emerging therapeutic opportunities”. In: *Seminars in Immunology* 40.November 2018 (2018), p. 101275. DOI: 10.1016/j.smim.2019.04.003.

[157] Sonia S. Elder and Elaine Emmerson. “Senescent cells and macrophages: Key players for regeneration?: Senescent cells and macrophages”. In: *Open Biology* 10.12 (2020). DOI: 10.1098/rsob.200309rsob200309.

[158] Cheng Zhou et al. “Quantitative assessment of radiation dose and fractionation effects on normal tissue by utilizing a novel lung fibrosis index model”. In: *Radiation Oncology* 12.1 (2017), pp. 1–8. DOI: 10.1186/s13014-017-0912-y.

[159] Alina Wiesemann et al. “Inhibition of Radiation-Induced Ccl2 Signaling Protects Lungs from Vascular Dysfunction and Endothelial Cell Loss”. In: *Antioxidants and Redox Signaling* 30.2 (2019), pp. 213–231. DOI: 10.1089/ars.2017.7458.

[160] Claudia E. Rübe et al. “Dose-dependent induction of transforming growth factor β (TGF-β) in the lung tissue of fibrosis-prone mice after thoracic irradiation”. In: *International Journal of Radiation Oncology Biology Physics* 47.4 (2000), pp. 1033–1042. DOI: 10.1016/S0360-3016(00)00482-X.

[161] A. J. Franko and J. Sharplin. “Development of fibrosis after lung irradiation in relation to inflammation and lung function in a mouse strain prone to fibrosis”. In: *Radiation Research* 140.3 (1994), pp. 347–355. DOI: 10.2307/3579112.

[162] Alexander V. Misharin et al. “Monocyte-derived alveolar macrophages drive lung fibrosis and persist in the lung over the life span”. In: *Journal of Experimental Medicine* 214.8 (2017), pp. 2387–2404. DOI: 10.1084/jem.20162152.

[163] Seth J. Kligerman, Teri J. Franks, and Jeffrey R. Galvin. “From the Radiologic Pathology Archives: Organization and fibrosis as a response to lung injury in diffuse alveolar damage, organizing pneumonia, and acute fibrinous and organizing pneumonia”. In: *Radiographics* 33.7 (2013), pp. 1951–1975. DOI: 10.1148/rg.337130057.

[164] Silke Meiners and Mareike Lehmann. “Senescent Cells in IPF: Locked in Repair?” In: *Frontiers in medicine* 7.December (2020), p. 606330. DOI: 10.3389/fmed.2020.606330.

[165] Jan Österreicher et al. “Role of type II pneumocytes in pathogenesis of radiation pneumonitis: Dose response of radiation-induced long changes in the transient high vascular permeability period”. In: *Experimental and Toxicologic Pathology* 56.3 (2004), pp. 181–187. DOI: 10.1016/j.etp.2004.08.003.

[166] Yevegeniy Vinogradskiy et al. “Spatial and dose-response analysis of fibrotic lung changes after stereotactic body radiation therapy”. In: *Medical Physics* 40.8 (2013). DOI: 10.1118/1.4813916.

[167] Jin Pan et al. “Inhibition of Bcl-2/xl With ABT-263 Selectively Kills Senescent Type II Pneumocytes and Reverses Persistent Pulmonary Fibrosis Induced by Ionizing Radiation in Mice.” In: *International journal of radiation oncology, biology, physics* 99.2 (2017), pp. 353–361. DOI: 10.1016/j.ijrobp.2017.02.216.

[168] Mareike Lehmann et al. “Senolytic drugs target alveolar epithelial cell function and attenuate experimental lung fibrosis ex vivo”. In: *European Respiratory Journal* 50.2 (2017), p. 1602367. DOI: 10.1183/13993003.02367-2016.

[169] Eun Joo Chung et al. “Truncated Plasminogen Activator Inhibitor-1 Protein Protects from Pulmonary Fibrosis Mediated by Irradiation in a Murine Model”. In: *International Journal of Radiation Oncology Biology Physics* 94.5 (2016), pp. 1163–1172. DOI: 10.1016/j.ijrobp.2015.11.044.

[170] Pavan Parikh et al. “Cellular senescence in the lung across the age spectrum”. In: *American Journal of Physiology - Lung Cellular and Molecular Physiology* 316.5 (2019), pp. L826–L842. DOI: 10.1152/ajplung.00424.2018.

[171] Judith Campisi. “Cellular senescence and lung function during aging: Yin and Yang”. In: *Annals of the American Thoracic Society* 13.December (2016), S402–S406. DOI: 10.1513/AnnalsATS.201609-703AW.

[172] Ivan R. Vogelius and Soren M. Bentzen. “A literature-based meta-analysis of clinical risk factors for development of radiation induced pneumonitis”. In: *Acta Oncologica* 51.8 (2012), pp. 975–983. DOI: 10.3109/0284186X.2012.718093.

[173] Marios Demetriades et al. “Interrogating and Quantifying In Vitro Cancer Drug Pharmacodynamics via Agent-Based and Bayesian Monte Carlo Modelling”. In: *Pharmaceutics* 14.4 (2022), pp. 1–15. DOI: 10.3390/pharmaceutics14040749.

[174] Steven Schramm. *PyROOT tutorial*. https://indico.cern.ch/event/704163/contributions/2936719/attachments/1693833/2726445/Tutorial-PyROOT.pdf. 2018.

[175] Andreas Pahl et al. “Regulation of IL-13 synthesis in human lymphocytes: implications for asthma therapy.” In: *British journal of pharmacology* 135.8 (2002), pp. 1915–26. DOI: 10.1038/sj.bjp.0704656.

[176] Vibha Lama et al. “Prostaglandin E2 synthesis and suppression of fibroblast proliferation by alveolar epithelial cells is cyclooxygenase-2-dependent”. In: *American Journal of Respiratory Cell and Molecular Biology* 27.6 (2002), pp. 752–758. DOI: 10.1165/rcmb.4857.

[177] Tadashi Kohyama et al. “Prostaglandin E2 inhibits fibroblast chemotaxis”. In: *American Journal of Physiology - Lung Cellular and Molecular Physiology* 281.5 25-5 (2001), pp. 1257–1263. DOI: 10.1152/ajplung.2001.281.5.l1257.

[178] Nicole L. Jansing et al. “Unbiased quantitation of alveolar type II to alveolar type i cell transdifferentiation during repair after lung injury in mice”. In: *American Journal of Respiratory Cell and Molecular Biology* 57.5 (2017), pp. 519–526. DOI: 10.1165/rcmb.2017-0037MA.

[179] Sona Hubackova et al. “IL1-and TGFβ-Nox4 signaling, oxidative stress and DNA damage response are shared features of replicative, oncogene-induced, and drug-induced paracrine ’Bystander senescence’”. In: *Aging* 4.12 (2012), pp. 932–951. DOI: 10.18632/aging.100520.

[180] C. Shao, M. Folkard, and K. M. Prise. “Role of TGF-B1 and nitric oxide in the bystander response of irradiated glioma cells”. In: *Oncogene* 27.4 (2008), pp. 434–440. DOI: 10.1038/sj.onc.1210653.

[181] Y. Jiang et al. “The role of TGF-β1-miR-21-ROS pathway in bystander responses induced by irradiated non-small-cell lung cancer cells”. In: *British Journal of Cancer* 111.4 (2014), pp. 772–780. DOI: 10.1038/bjc.2014.368.

[182] Juan Carlos Acosta et al. “A complex secretory program orchestrated by the inflammasome controls paracrine senescence”. In: *Nature Cell Biology* 15.8 (2013), pp. 978–990. DOI: 10.1038/ncb2784.

[183] Eun Joo Chung et al. “Natural variation in macrophage polarization and function impact pneumocyte senescence and susceptibility to fibrosis.” In: *Aging* 14.undefined (2022), pp. 1–26. DOI: 10.18632/aging.204309.

[184] Nagaraja Nagre et al. “Alveolar Macrophage Phagocytosis and Bacteria Clearance in Mice.” In: *Journal of visualized experiments : JoVE* 145 (2019), pp. 1–12. DOI: 10.3791/59088.

[185] William J Janssen et al. “Surfactant proteins A and D suppress alveolar macrophage phagocytosis via interaction with SIRP alpha.” In: *American journal of respiratory and critical care medicine* 178.2 (2008), pp. 158–67. DOI: 10.1164/rccm.200711-1661OC.

[186] Bin Hu et al. “Deficient In Vitro and In Vivo Phagocytosis of Apoptotic T Cells by Resident Murine Alveolar Macrophages”. In: *The Journal of Immunology* 165.4 (2000), pp. 2124–2133. DOI: 10.4049/jimmunol.165.4.2124.

[187] H. Fehrenbach et al. “Keratinocyte growth factor-induced hyperplasia of rat alveolar type II cells in vivo is resolved by differentiation into type I cells and by apoptosis”. In: *European Respiratory Journal* 14.3 (1999), pp. 534–544. DOI: 10.1034/j.1399-3003.1999.14c10.x.

[188] Lynn M. Crosby et al. “Balance of life and death in alveolar epithelial type II cells: Proliferation, apoptosis, and the effects of cyclic stretch on wound healing”. In: *American Journal of Physiology - Lung Cellular and Molecular Physiology* 301.4 (2011), pp. 536–546. DOI: 10.1152/ajplung.00371.2010.

[189] Balázs G. Madas. “Radon induced hyperplasia: Effective adaptation reducing the local doses in the bronchial epithelium”. In: *Journal of Radiological Protection* 36.3 (2016), pp. 653–666. DOI: 10.1088/0952-4746/36/3/653.

[190] Angela M. Groves et al. “Role of Infiltrating Monocytes in the Development of Radiation-Induced Pulmonary Fibrosis”. In: *Radiation Research* 189.3 (2018), pp. 300–311. DOI: 10.1667/RR14874.1.

[191] Bennett G Childs et al. “Senescence and apoptosis: dueling or complementary cell fates?” In: *EMBO reports* 15.11 (2014), pp. 1139–1153. DOI: 10.15252/embr.201439245.

[192] John P. Kirkpatrick, David J. Brenner, and Colin G. Orton. “The linear-quadratic model is inappropriate to model high dose per fraction effects in radiosurgery”. In: *Medical Physics* 36.8 (2009), pp. 3381–3384. DOI: 10.1118/1.3157095.

[193] Adrian C. Begg, Fiona A. Stewart, and Conchita Vens. “Strategies to improve radiotherapy with targeted drugs”. In: *Nature Reviews Cancer* 11.4 (2011), pp. 239–253. DOI: 10.1038/nrc3007.

[194] Dustin Begosh-Mayne et al. “The dose–response characteristics of four NTCP models: using a novel CT-based radiomic method to quantify radiation-induced lung density changes”. In: *Scientific Reports* 10.1 (2020), pp. 1–9. DOI: 10.1038/s41598-020-67499-0.

[195] Lawrence B. Marks et al. “Use of Normal Tissue Complication Probability Models in the Clinic”. In: *International Journal of Radiation Oncology Biology Physics* 76.3 SUPPL. (2010). DOI: 10.1016/j.ijrobp.2009.07.1754.

[196] Giuseppe Palma et al. “Spatial Dose Patterns Associated With Radiation Pneumonitis in a Randomized Trial Comparing Intensity-Modulated Photon Therapy With Passive Scattering Proton Therapy for Locally Advanced Non-Small Cell Lung Cancer”. In: *International Journal of Radiation Oncology Biology Physics* 104.5 (2019), pp. 1124–1132. DOI: 10.1016/j.ijrobp.2019.02.039.

[197] Katherine Mah et al. “Acute radiation-induced pulmonary damage: a clinical study on the response to fractionated radiation therapy.” In: *International journal of radiation oncology, biology, physics* 13.2 (1987), pp. 179–88. DOI: 10.1016/0360-3016(87)90125-8.

[198] Maria L. Hernando et al. “Radiation-induced pulmonary toxicity: A dose-volume histogram analysis in 201 patients with lung cancer”. In: *International Journal of Radiation Oncology Biology Physics* 51.3 (2001), pp. 650–659. DOI: 10.1016/S0360-3016(01)01685-6.

[199] S L Kwa et al. “Radiation pneumonitis as a function of mean lung dose: an analysis of pooled data of 540 patients.” In: *International journal of radiation oncology, biology, physics* 42.1 (1998), pp. 1–9. DOI: 10.1016/s0360-3016(98)00196-5.

[200] H. Rodney Withers. *The Four R’s of Radiotherapy*. Vol. 5. ACADEMIC PRESS, INC., 1975, pp. 241–271. DOI: 10.1016/b978-0-12-035405-4.50012-8.

[201] Marco Durante, Roberto Orecchia, and Jay S. Loeffler. “Charged-particle therapy in cancer: Clinical uses and future perspectives”. In: *Nature Reviews Clinical Oncology* 14.8 (2017), pp. 483–495. DOI: 10.1038/nrclinonc.2017.30.

[202] Pankaj Chaudhary et al. “Variations in the Processing of DNA Double-Strand Breaks Along 60-MeV Therapeutic Proton Beams”. In: *International Journal of Radiation Oncology Biology Physics* 95.1 (2016), pp. 86–94. DOI: 10.1016/j.ijrobp.2015.07.2279.

[203] Dorota Słonina et al. “Relative biological effectiveness of the 60-MeV therapeutic proton beam at the Institute of Nuclear Physics (IFJ PAN) in Kraków, Poland.” In: *Radiation and environmental biophysics* 53.4 (2014), pp. 745–54. DOI: 10.1007/s00411-014-0559-0.

[204] R G Dale and B Jones. “The assessment of RBE effects using the concept of biologically effective dose.” In: *International journal of radiation oncology, biology, physics* 43.3 (1999), pp. 639–45. DOI: 10.1016/s0360-3016(98)00364-2.

[205] Harald Paganetti. “Relative biological effectiveness (RBE) values for proton beam therapy. Variations as a function of biological endpoint, dose, and linear energy transfer”. In: *Physics in Medicine and Biology* 59.22 (2014), R419–R472. DOI: 10.1088/0031-9155/59/22/R419.

[206] Francisco D. C. Guerra Liberal and Stephen J. McMahon. “Characterization of Intrinsic Radiation Sensitivity in a Diverse Panel of Normal, Cancerous and CRISPR-Modified Cell Lines”. In: *International Journal of Molecular Sciences* 24.9 (2023), p. 7861. DOI: 10.3390/ijms24097861.

[207] Cheng Zhou et al. “Determining RBE for development of lung fibrosis induced by fractionated irradiation with carbon ions utilizing fibrosis index and high-LET BED model”. In: *Clinical and Translational Radiation Oncology* 14 (2019), pp. 25–32. DOI: 10.1016/j.ctro.2018.10.005.

[208] Michael R Elliott and Kodi S Ravichandran. “The Dynamics of Apoptotic Cell Clearance.” In: *Developmental cell* 38.2 (2016), pp. 147–60. DOI: 10.1016/j.devcel.2016.06.029.

[209] S. Incerti et al. “THE Geant4-DNA project”. In: *International Journal of Modeling, Simulation, and Scientific Computing* 1.2 (2010), pp. 157–178. DOI: 10.1142/S1793962310000122. arXiv: 0910.5684.

[210] J. Perl et al. “TOPAS: An innovative proton Monte Carlo platform for research and clinical applications”. In: *Medical Physics* 39.11 (2012), pp. 6818–6837. DOI: 10.1118/1.4758060.

[211] Asim Ejaz, Joel S. Greenberger, and Peter J. Rubin. “Understanding the mechanism of radiation induced fibrosis and therapy options”. In: *Pharmacology and Therapeutics* 204 (2019), p. 107399. DOI: 10.1016/j.pharmthera.2019.107399.

List of Figures

List of Tables

Publications related to this thesis

Peer-reviewed first author publications

- Cogno, N.; Bauer, R.; Durante, M. A 3D Agent-Based Model of Lung Fibrosis. *Symmetry* **2022**, 14, 90. https://doi.org/10.3390/sym14010090
- Cogno, N.; Bauer, R.; Durante, M. An Agent-Based Model of Radiation-Induced Lung Fibrosis. *Int. J. Mol. Sci.* **2022**, 23, 13920. https://doi.org/10.3390/ijms232213920

Submitted first author publications

- Cogno N. et al. "Mechanistic model of radiotherapy-induced lung fibrosis using coupled 3D Agent-Based and Monte Carlo simulations". Submitted to: Nature Communications Medicine (2023)
- Cogno N. et al. "Recipes for calibration and validation of agent-based models in cancer biomedicine". Submitted to: Cancer Biology & Therapy (2023)

Acknowledgements

Not without ups and downs, three and half years have already gone. And despite the negligible changes in my location, it felt as if time flowed at variable speeds throughout this journey. Looking back, I must admit I could have never expected this to be such an enriching experience, and I find myself wondering how and whether I could have grown this much in a parallel world, taking a different path. The answer, most likely, is no, and the reason behind it lies in the people that, near or far, surrounded me, supported me and allowed me to go through this PhD.

First of all, I want to thank my supervisor Marco Durante for allowing me to pursue a PhD in such a dynamic environment, for his support, his advice, his experience, his kindness and for always showing his genuine passion and excitement for research in general. Thank you for allowing me to be often independent and focus on what interested me the most. I also want to thank Roman Bauer for his supervision at all times. Despite the distance, you've always found the time to provide me with precious inputs and guidance.

I want to thank the BioDynaMo team, especially Tobias, Lukas, Ahmad, Jack, Vasileios and Marco, for your endless patience, your support, the fruitful discussions and challenges. You really made me feel part of a team and I've learned so much from you and with you.

A special thanks goes to all my colleagues and friends at GSI. Thank you Gianmarco, Tamara, Francesca, Laura, Timo, Chiara, Cosimo, Martina, Cristina, Gaia and Amèlia, you really made these years feel easier and made me feel at home. We often went through similar difficulties and I hope I was able to give back to you a little bit of what you gave to me. Thank you Patryk, Charles, Christian, Charis and Min. I've always looked forward to spending time with you and I have amazing memories from these years. It felt like we were long-time friends since we first met. Thank you Gian and Tamara, for your honest and genuine friendship. Gian, you were always there to discuss our research topics, and you always knew how to make me laugh. Sharing the office and snacks in the afternoon with you two was a real pleasure. Thank you Nacho, for your friendship born during the scary German classes. We shared the passion for running as well as hard workouts in cold mornings, thank you for making it feel more enjoyable.

Thank you to the Life Science Engineering graduate school for making this all possible. Thank you for the interesting meetings and retreats, you allowed me to broaden my scientific background and put me in contact with a network of brilliant scientists sharing my same journey.

Thank you Martine Kräckmann and Maria Didonna-Schnellbächer, you helped me since the very beginning, in the middle of the Covid pandemic, and endless times throughout these years with all the paperwork related to the GSI and the university, I am truly grateful.

A huge thanks goes to my family, for their inexhaustible support, their understanding and help hundreds of kilometres away. Being separated for so long was all but easy for both of us, and yet you never ceased to push me, I knew you were always there for me. I wouldn't even be halfway through this journey if it wasn't for you. Thank you, Lucry, for always having kind words for me.

And last, but definitely not least, I would like to thank Vanessa. We've started together, moved to Darmstadt together and shared every day of the last three and half years. Not only you encouraged me to start, but you also inspired me every day throughout this adventure as a passionate and tireless researcher. You're a role model for me and I owe you so much.

Erklärungen laut Promotionsordnung

§ 8 Abs. 1 lit. c PromO

Ich versichere hiermit, dass die elektronische Version meiner Dissertation mit der schriftlichen Version übereinstimmt.

§ 8 Abs. 1 lit. d PromO

Ich versichere hiermit, dass zu einem vorherigen Zeitpunkt noch keine Promotion versucht wurde. In diesem Fall sind nähere Angaben über Zeitpunkt, Hochschule, Dissertationsthema und Ergebnis dieses Versuchs mitzuteilen.

§ 9 Abs. 1 PromO

Ich versichere hiermit, dass die vorliegende Dissertation selbstständig und nur unter Verwendung der angegebenen Quellen verfasst wurde.

§ 9 Abs. 2 PromO

Die Arbeit hat bisher noch nicht zu Prüfungszwecken gedient.

Darmstadt, 17. Oktober 2023

N. Cogno